DEPARTMENT OF PHYSICS
UNIVERSITY OF JYVÄSKYLÄ
RESEARCH REPORT No. 5/2012

Particle radiation in microelectronics

BY
ARTO JAVANAINEN

Academic Dissertation
for the Degree of
Doctor of Philosophy

to be presented, by permission of the
Faculty of Mathematics and Science
of the University of Jyväskylä,
for public examination in Auditorium FYS 1 of the
University of Jyväskylä on June 20, 2012
at 12 o'clock noon

Jyväskylä, Finland
June 2012

To our beloved daughters
Iida and Edla

"Mielikuvitus on tietoa tärkeämpää"
"Imagination is more important than knowledge"
— *Albert Einstein*

Preface

The work reported in this thesis has been carried out over the years 2005–2012 at the Accelerator Laboratory of the University of Jyväskylä. It has been a great pleasure to work in the RADEF group all these years.

Most of all, I want to thank my supervisor Dr. Ari Virtanen for his endless patience and all the fruitful conversations we have had about physics and beyond. Very special thanks go to Mr. Reno Harboe-Sørensen from the European Space Research and Technology Centre of the European Space Agency. Reno's extraordinary experience in the field of radiation effects and his invaluable guidance have been the main driving forces for this work and the whole existence of RADEF facility. Dr. Heikki Kettunen and Mr. Mikko Rossi deserve my thanks for all the help they have offered me over the years in various experiments. Also I have to thank Dr. Iiro Riihimäki, whose impact on this work cannot be ignored.

I want to thank Dr. Tomek Malkiewicz, Dr. Jarek Perkowski and Mr. Mikko Sillanpää for helping me in the stopping force measurements. Especially I want to thank Dr. Wladek Trzaska for his guidance on theoretical and experimental aspects of stopping. Also I have to thank the staff of technical workshops, both electrical and mechanical, for all their help over the years.

Although this work was done in Jyväskylä, there was several people involved from outside JYFL, who need recognition. From Sandia National Laboratories, I want to thank Dr. Jim Schwank and Dr. Marty Shaneyfelt for their support in the charge yield experiments. I thank Dr. Veronique Ferlet-Cavrois of ESA/ESTEC for all the support that she has provided. Also I'm grateful to Dr. Peter Sigmund from University of Southern Denmark for all the discussions that we have had about stopping force.

This work was supported by the Academy of Finland under the Finnish Centre of Excellence in Nuclear and Accelerator Based Physics Research Programmes 2006–2011 and 2012–2017 (Projects No. 213503 and No. 251353), and European Space Agency (ESA/ESTEC Contract No. 18197/04/NL/CP). The financial support from Emil Aaltonen foundation is gratefully acknowledged.

I owe a dept of gratitute to my parents, who have always supported me in my activities. Last but not least, I want to thank my wife Riitu, who has acted as a counterbalance and not have let me to dig myself too deep into the trenches.

Jyväskylä, May 2012

Arto Javanainen

Abstract

Javanainen, Arto, 1978–
Particle radiation in microelectronics
Jyväskylä: University of Jyväskylä, 2012, 109 pages
Research report No. 5/2012 / Department of Physics, University of Jyväskylä,
ISSN 0075-465X; 5/2012
ISBN paper copy: 978-951-39-4726-2
ISBN electronic: 978-951-39-4727-9
diss.

The unavoidable presence of particle radiation in space and on the ground combined with constantly evolving technology necessitates a deep understanding of the basic mechanisms underlying radiation effects in materials and electronic devices.

This thesis provides an overview of the different radiation environments, with a review of the interaction mechanisms between energetic particles and matter. In this work a new semi-empirical model for estimating the electronic stopping force of solids for heavy ions is introduced. Radiation effects occurring in microelectronics due to particle radiation are also discussed with a brief introduction to radiation hardness assurance (RHA) testing of electronics.

The thesis introduces the RADiation Effects Facility (RADEF) of the Accelerator Laboratory in University of Jyväskylä and its utilization in the RHA testing.

The experimental part of this thesis consists of data concerning the electronic stopping force of silicon for heavy ions, and heavy-ion induced charge yield in silicon dioxide. For the stopping force measurements a new method called B–TOF was developed and utilized, the details of which are given in this thesis. The stopping force data are used for parameterization of the developed semi-empirical model, which in turn is the basis for a stopping force prediction code. This code is being used by the European Space Agency in its heavy-ion irradiation facilities.

Both of the experimental sections include previously unpublished results, which will improve knowledge of the interactions of energetic particles in bulk materials and electronic devices.

Keywords: radiation effects, electronics, stopping force, heavy ions, silicon, silicon dioxide, recombination

Author Arto Javanainen
Department of Physics
University of Jyväskylä
Jyväskylä
Finland
email: arto.javanainen@jyu.fi

Supervisor Docent Ari Virtanen
Department of Physics
University of Jyväskylä
Jyväskylä
Finland

Reviewers Professor Laurent Dusseau
University Montpellier II
Montpellier
France

Professor Jyrki Räisänen
Department of Physics
University of Helsinki
Helsinki
Finland

Opponent Professor Kenneth F. Galloway
School of Engineering
Vanderbilt University
Nashville, Tennessee
USA

List of Author's Publications

This thesis is mainly based on the results published in the following articles:

A.I **A. Javanainen**, T. Malkiewicz, J. Perkowski, W. H. Trzaska, A. Virtanen, G. Berger, W. Hajdas, R. Harboe-Sørensen, H. Kettunen, V. Lyapin, M. Mutterer, A. Pirojenko, I. Riihimäki, T. Sajavaara, G. Tyurin, and H. J. Whitlow, "Linear energy transfer of heavy ions in silicon,"
IEEE Trans. Nucl. Sci., vol. 54, no. 4, pp. 1158–1162, August 2007.
Available from: http://dx.doi.org/10.1109/TNS.2007.895121

A.II **A. Javanainen**, M. Sillanpää, W. H. Trzaska, A. Virtanen, G. Berger, W. Hajdas, R. Harboe-Sørensen, H. Kettunen, T. Malkiewicz, M. Mutterer, J. Perkowski, A. Pirojenko, I. Riihimäki, T. Sajavaara, G. Tyurin, and H. J. Whitlow, "Experimental linear energy transfer of heavy ions in silicon for RADEF cocktail species,"
IEEE Trans. Nucl. Sci., vol. 56, no. 4, pp. 2242–2246, August 2009.
Available from: http://dx.doi.org/10.1109/TNS.2008.2009983

A.III **A. Javanainen**, J. R. Schwank, M. R. Shaneyfelt, R. Harboe-Sørensen, A. Virtanen, H. Kettunen, S. M. Dalton, P. E. Dodd, and A. Jaksic, "Heavy-ion induced charge yield in MOSFETs,"
IEEE Trans. Nucl. Sci., vol. 56, no. 6, pp. 3367–3371, December 2009.
Available from: http://dx.doi.org/10.1109/TNS.2009.2033687

A.IV **A. Javanainen**, W. H. Trzaska, R. Harboe-Sørensen, A. Virtanen, G. Berger, W. Hajdas, "Semi-empirical LET descriptions of heavy ions used in the European Component Irradiation Facilities,"
IEEE Trans. Nucl. Sci., vol. 57, no. 4, pp. 1946–1949, August 2010.
Available from: http://dx.doi.org/10.1109/TNS.2009.2036353

A.V **A. Javanainen**, "A simple expression for electronic stopping force of heavy ions in solids,"
Nucl. Instr. Meth. B., in press, 2012.
Available from: http://dx.doi.org/10.1016/j.nimb.2012.05.013

Author's contribution

The author has made most of the data acquisition, analysis and writing for the articles A.I–A.IV. For A.V the author of this thesis is the sole contributor. Articles A.I–A.V are included in the end of this thesis.

In the following articles the author of this thesis has been assisting in the data acquisition, analysis and writing.

I V. Ferlet-Cavrois, J. R. Schwank, S. Liu, M. Muschitiello, Th. Beutier, **A. Javanainen**, A. Hedlund, C. Poivey, A. Zadeh, R. Harboe-Sørensen, G. Santin, B. Nickson, A. Menicucci, C. Binois, D. Peyre, S. K. Hoeffgen, S. Metzger, D. Schardt, H. Kettunen, A. Virtanen, G. Berger, B. Piquet, J.-C. Foy, M. Zafrani, P. Truscott, M. Poizat, F. Bezerra, "Influence of beam conditions and energy for SEE testing,"
IEEE Trans. Nucl. Sci., in press, 2012.
Available from: http://dx.doi.org/10.1109/TNS.2012.2187681

II T. Siiskonen, H. Kettunen, K. Peräjärvi, **A. Javanainen**, M. Rossi, W. H. Trzaska, J. Turunen, and A. Virtanen, "Energy loss measurement of protons in liquid water,"
Phys. Med. Biol., vol. 56, pp. 2367–2374, March 2011.
Available from: http://dx.doi.org/10.1088/0031-9155/56/8/003

III J. Perkowski, J. Andrzejewski, **A. Javanainen**, W. H. Trzaska, T. Malkiewicz, K. Sobczak, and A. Virtanen, "The first experimental values for the stopping power of ^{89}Y ions in carbon, nickel and gold,"
Vacuum, vol. 83, no. 1, pp. S73–S76, May 2009.
Available from: http://dx.doi.org/10.1016/j.vacuum.2009.01.025

IV J. Perkowski, J. Andrzejewski, **A. Javanainen**, T. Malkiewicz, K. Sobczak, A. Virtanen, and W. H. Trzaska, "The first experimental values for the stopping power of Au ions in nickel,"
Act. Phys. Pol. B, vol. 39, no. 2, pp. 507–511, February 2008.
Available from: http://www.actaphys.uj.edu.pl/vol39/pdf/v39p0507.pdf

V A. Virtanen, R. Harboe-Sorensen, **A. Javanainen**, H. Kettunen, H. Koivisto, and I. Riihimäki, "Upgrades for the RADEF facility,"
IEEE Radiation Effect Data Workshop, pp. 38–41, July 2007.
Available from: http://dx.doi.org/10.1109/REDW.2007.4342538

Contents

Introduction

Our world is filled and surrounded with microelectronics and increasing amount is being launched to space all the time. According to Ref. [1] there is more than 900 active satellites orbiting the Earth. Also, there are several man-made vehicles deeper in space. Obviously, all these are carrying varying amount of electronics on board. From the electronics point of view the radiation environment, where these systems need to operate, is far more hostile compared to the ground level. The first anomalies in satellite electronics due to galactic cosmic rays were reported in 1975[2]. Ever since there have been numerous failures observed in space projects due to radiation. The latest major incident being the loss of the Russian *Phobos-Ground* (Фобос-Грунт) mission, which occurred in January 2012 allegedly because of cosmic radiation.

The radiation effects are not entirely restricted to space. Already in 1976, the bit errors in the computers used in Los Alamos National Laboratory, US, were proven to be caused by atmospheric neutrons [3]. Also these effects have been demonstrated to occur in avionics [4]. In addition to this, authors in Ref. [5] suggest that the future state-of-the-art devices, produced with the modern deep-sub-micron technologies, are expected to be susceptible to errors induced by muons from the cosmic ray showers. Of course, at ground level there are also places such as, nuclear power plants and particle accelerators (e.g. LHC at CERN) with very high radiation levels and where electronics is used and their radiation durability needs to be assured.

Interactions between radiation and matter have been realized ever since the first forms of radiation were recognized. The radiation effects in electronics were first thought to be either *total ionizing* or *displacement damage effects* until beginning of the 60's. In 1962, Wallmark and Marcus in Ref. [6] gave the first predictions on the increase in the *probability of failures* in electronics due to cosmic ray ionization with technological evolution. The increasing reliance on electronics in our everyday life (communication, national and international security, traveling, etc.) combined with the technological evolution towards the *nano-scale*, make us vulnerable in case of failures. The cosmic radiation is a natural process which cannot be avoided, not even at ground level, but the radiation effects can be mitigated. For this, the knowledge on the interactions between radiation and matter, and the mechanisms how the electronics are affected, is crucial.

This thesis will try to unfold some of the physical mechanisms involved in the

heavy-ion interactions with matter, and the effects of energetic heavy ions in silicon based materials and devices. As the vast majority of electronics are based on silicon technology, the obvious choice of material under study was silicon. The experimental focus in this work is in the *stopping force* of silicon for various heavy ions. In addition to this, the *charge yield* of heavy-ion induced ionization in silicon dioxide was also experimentally defined, namely using *Metal-Oxide-Semiconductor-Field-Effect-Transistors* (MOSFET) as the test vehicles.

The thesis has been outlined as the following. First an introductory is given on particle radiation environments, discussing about the space radiation environments, and the sources of particle radiation existing on Earth. The second part is dedicated to describe the interactions between energetic particles and matter, mainly focusing on the theory of electronic stopping force. This part introduces a new semi-empirical stopping force model developed in this work. The effects induced by particle radiation in electronic devices are discussed in Chapter 3, consisting of e.g. consideration of the applicability of the *Linear Energy Transfer* as the metric for radiation damage in electronics. Discussion on the main principles of *Radiation Hardness Assurance testing* (RHA) of electronics is presented in Chapter 4. There is also a detailed introduction on the utilization of the RADiation Effects Facility (RADEF) in RHA testing at the Accelerator Laboratory of the University of Jyväskylä. In Chapter 5, the description of the experimental part of this work is given with detailed information on the methods and the set-ups which were used, and results obtained. The experimental part consists of two different investigations:

1. Electronic stopping force measurements for heavy ions in silicon using an updated measuring concept.

2. Heavy-ion induced charge yield in SiO_2.

Both of the experimental parts contain previously unpublished results. Finally Chapter 6 summarizes the work and discusses briefly about the outlook.

1 Particle radiation environments

In this chapter the different sources of particle radiation are briefly discussed. The primary focus is in the space radiation environment, but also the radiation sources at ground level are introduced.

1.1 The Space

The shortage of medium in space enables energetic particles to travel great distances without scattering, i.e. without energy losses. In outer space, away from any radiation sources (i.e. stars) or planets with magnetic fields, the amount of particle radiation is very small. In the vicinity of the Sun and the Earth, the particle radiation is non-negligible. In this work the space radiation environment is considered to prevail in the region reaching from the Sun to the upper atmosphere of the Earth. This region of space consists of three major sources of particle radiation: (1) the Sun, (2) trapped particles in the Earth's magnetic field and (3) Galactic Cosmic Rays (GCR). These are discussed in the following. Also monitoring and forecasting of the *space weather* and its implications for our everyday life are briefly viewed.

1.1.1 The Sun

Of all the particle radiation sources in the vicinity of the Earth, the Sun is the most remarkable. The vast majority of the particle radiation, which is present in the interplanetary space near Earth or is trapped in the Earth's magnetosphere, is of solar origin. The regular flow of energy from the Sun is called the *solar wind*. In addition to electro-magnetic radiation, the solar wind is mostly consisting of high energy electrons and protons. In the solar wind, the particle plasma travels through space with an average velocity of approximately 400 km/s, and the average proton densities, in absence of any major solar events (see Section 1.1.1.2), are in the order of 1–10 protons/cm^3 [7]. This yields to average proton fluxes of $4 - 40 \cdot 10^7 \mathrm{cm}^{-2}\mathrm{s}^{-1}$.

1.1.1.1 Sunspot cycle

The Sun's activity has been observed to have periodicity of approximately 11 years, which is called the *solar cycle*. The activity of the Sun is closely related with the

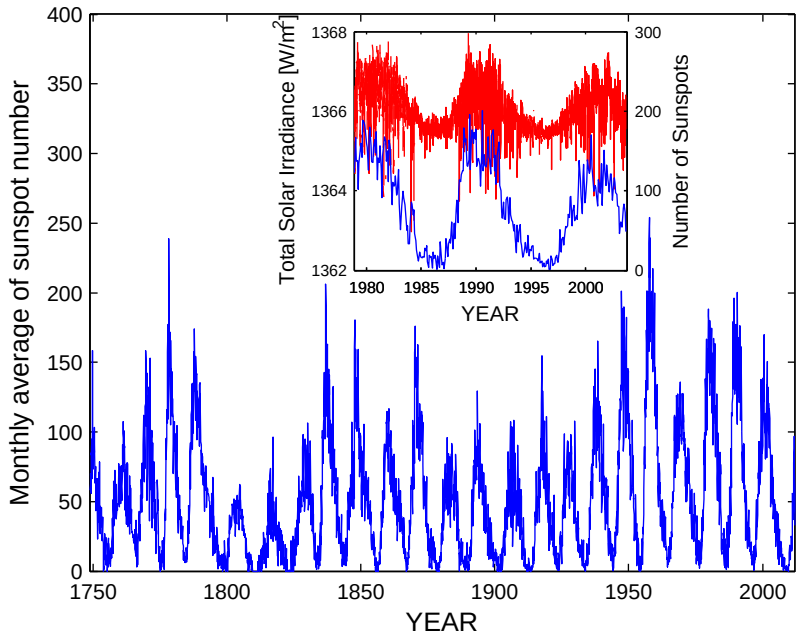

Figure 1.1: Monthly average of sunspot number from beginning of 1749 to February 2012 as taken from Ref. [8]. In addition to the sunspot number, the data taken from Refs. [9–11] for Total Solar Irradiance at 1 A.U from November 1978 to October 2003 is presented in the inset.

number of sunspots observed in the Sun's surface. The first European observations of the sunspots were done in the 17th century, but the daily records were started in 1749 [8]. There is some scarce records available, dating back to year 1610. The counting of these cycles was started in 1760's, when the occurrance of the first official full cycle has been agreed. Thus, now in 2012 the 24th cycle is ongoing. The monthly average of the sunspot number from Ref. [8], is presented in Fig. 1.1 with data from Refs. [9–11] for the *Total Solar Irradiance* (TSI). The value of TSI gives the total irradiated power by the Sun in units of $\mathrm{W/m^2}$, estimated at the distance of 1 *Astronomical Unit* (A.U.) from the Sun, which essentially equals the *Sun-to-Earth distance*[12]. The "11-year" periodicity as well as the correlation between the Sun's activity and sunspot number are clearly seen in the inset figure.

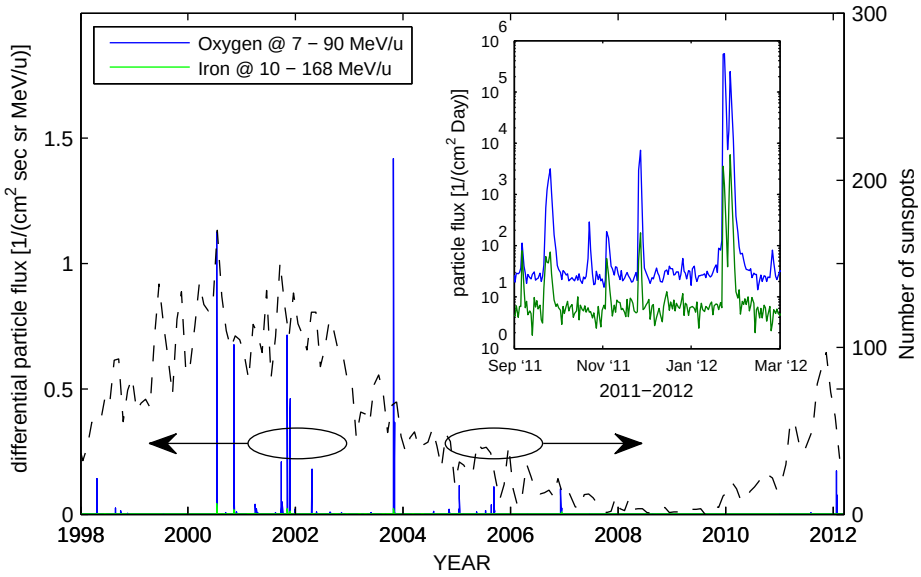

Figure 1.2: Daily average of solar energetic particle fluxes from 1998 to March 2012 for oxygen and iron ions measured by the Solar Isotope Spectrometer on the Advanced Composition Explorer spacecraft[13], with monthly average sunspot number taken from Ref. [8]. Particle flux data are taken from Ref. [7].

1.1.1.2 Solar flares and Coronal Mass Ejections

Apart from the solar cycle discussed above, there are very unpredictable phenomena occurring in the Sun. Occasionally interactions between the hot plasma and the magnetic fields on the surface of the Sun create conditions, where huge amounts of plasma are ejected. These eruptions are called the *solar flares*. The real massive solar flares are called the *Coronal Mass Ejections* (CMEs). The CMEs are orders of magnitude larger compared to regular solar flares. In a CME event, a huge part of the Sun's corona explodes and is ejected from the Sun with velocities up to thousands of km/s, consisting of matter up to 10^{10} metric tons [14].

The solar flares mainly consists of electrons and protons, but there is also heavier ions, such as oxygen and iron, present in the shockwaves. In Fig. 1.2 the average particle fluxes in the solar wind for oxygen and iron ions are presented as they have been measured by the *Solar Isotope Spectrometer*[15] on the *Advanced Composition Explorer spacecraft*[13]. These data are available online at Ref. [7]. The graph presents the data taken between two *solar maxima* around years 2001 and 2012. In the graph

the solar activity is presented by the monthly averaged *sunspot number* from Ref. [8]. The data clearly demonstrates the increased occurence of bursts in the heavy-ion fluxes during the high activity season of the Sun. The variability in the ion fluxes is more easily observed in the inset graph. The observed peaks are associated with solar flares, and the highest ones are due to the CMEs. Although, the amount of heavier ions in CMEs is much lower compared to that of even the constant solar wind protons or electrons, they can cause problems in the electronics more easily due to their higher ability to ionize matter (i.e. stopping force). More discussion on the particle–matter interactions in materials and particle induced effects in electronics is presented in Chapters 2 and 3.

1.1.2 Trapped particles – Van Allen belts

The Earth's magnetic field prohibits energetic charged particles to reach directly the Earth's surface. On the other hand, part of the charged particles are trapped in the magnetosphere, thus constituting regions with high radiation fields known as the *Van Allen belts*[16]. These belts are mostly consisting of energetic protons and electrons. There are two distinct regions called the *inner*- and the *outer* belt, or zone. The inner belt is typically referred to as the proton belt and the outer one as the electron belt, because these regions are mainly occupied by these particles.

1.1.2.1 South Atlantic Anomaly

The Earth's invariably moving *magnetic dip poles* (North pole: 85.01°N, 132.66°W, South pole: 64.43°S, 137.32°E [17]) diverge from the *geographical poles*. In addition to this, the magnetic dip poles are not antipodal[1], on the contrary to the geographical poles which are antipodal by definition[17]. This misalignment causes eccentricity in the Van Allen belts in respect to the Earth's surface. Hence there is an increased amount of energetic particles reaching very low altitudes in the South Atlantic region east from Brazil. This region is called the *South Atlantic Anomaly* (SAA). The SAA is illustrated in the Fig. 1.3, where the fluxes of >100 MeV protons and >5 MeV electrons at altitude of 500 km are presented as taken from Ref. [18]. One should note that in this figure the SAA region is consisting only of protons at these given energies. The SAA exposes high altitude aircrafts to higher radiation levels compared to other regions around the globe. Moreover, the SAA poses a severe threat to satellites orbiting the Earth.

[1] straight line drawn between these two poles does not cross the center of the Earth

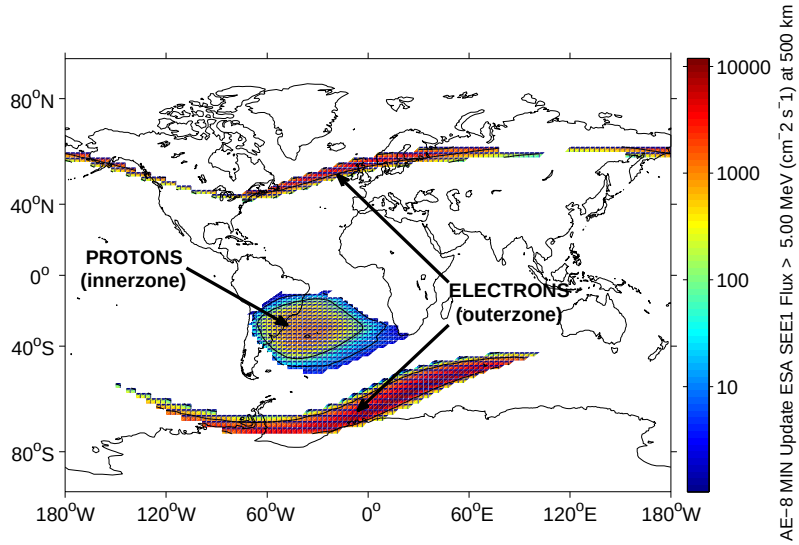

Figure 1.3: Proton (100 MeV) and electron (5 MeV) intensities at 500 km altitude estimated by the AP8-MIN and AE8-MIN models, respectively [19, 20]. The South Atlantic Anomaly can be clearly seen in the south–east coast of Brazil where there is distinct region of energetic protons reaching altitudes of 500 km. Data taken from the ESA's Space Environment Information System (SPENVIS) in Ref. [18]

1.1.3 Galactic cosmic rays

The satellites, which are orbiting the Earth e.g. in *Low Earth Orbit* (LEO)[2] below the Van Allen belts, are experiencing relative stable and low radiation fields with occasional disruptions by high solar activity (i.e. solar flares and CMEs, see 1.1.1.2). On the other hand, the radiation environment outside the radiation belts is much more irregular and prone to variations by the solar activity. Nevertheless, if the solar contribution in the radiation environment is taken aside, there is a relatively constant flow of heavy particles at very high energies. These particles are called the *Galactic Cosmic Rays* (GCR), as they are supposedly originating from supernovae explosions in other galaxies. Their energies can reach up to several hundreds of GeV/u. By using the *CREME-code*[3], available online at Ref. [22], the radiation environment due to GCRs can be estimated. Estimations for environments in the *Geostationary Earth Orbit* (GEO)[4] or near Earth interplanetary space, are presented in Fig. 1.4. These

[2]LEO is referred to as the orbits reaching from few hundreds up to few thousands of kilometers above the Earth's surface.

[3]CREME stands for *Cosmic Ray Effects on MicroElectronics*. The basis of the CREME-code is presented in Ref. [21].

[4]GEO is a circular orbit approximately 36 000 km above the Earth's equator.

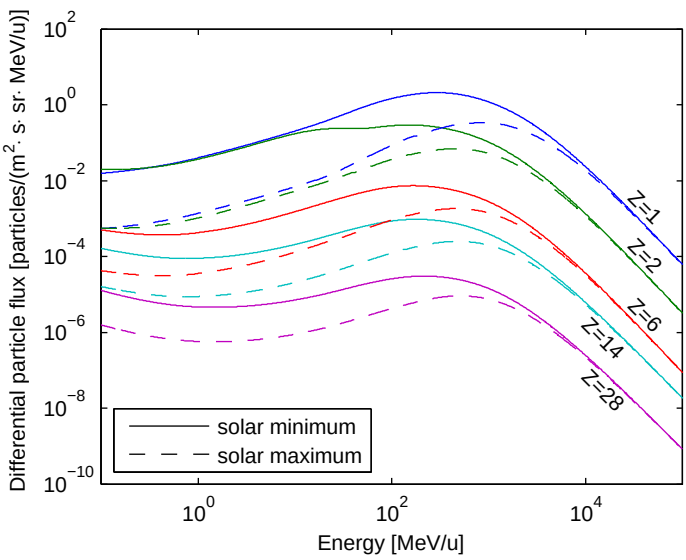

Figure 1.4: Differential flux of selected galactic cosmic ray particles after 2.54 mm of aluminum as a function of energy per nucleon in GEO or near Earth interplanetary space during the solar minimum (solid line) and the solar maximum (dashed line). Data are taken from [22].

regions are generally considered to be less influenced by the Earth's magnetic field. In the graph the differential fluxes of selected GCR particles are given as a function of energy per nucleon. The fluxes are defined after 2.54 mm of aluminum, which is considered to be typical shielding thickness (and material) in spacecrafts. The selected particles are: proton, alpha, carbon, silicon and nickel. The particle fluxes are plotted according to the estimations for solar minimum and maximum. The difference in the spectra, presented in Fig. 1.4, between the solar maximum and minimum is likely due to the magnetic field variations in the Sun with its activity. High solar activity during the solar maximum gives rise to higher solar magnetic fields, and thus GCRs at low energies are deflected.

In GCRs, protons are the most abundant, which is readily seen in Fig. 1.4. The same is illustrated in Fig. 1.5, where the relative abundances of particle species are presented as a function of atomic number. This graph shows the rapid drop in the particles with atomic numbers above iron ($Z \sim 26$). This is due to the maximum in the nuclear binding energy for the atomic masses around $A = 60$. This results in a maximum of the *electronic stopping force* of silicon for GCRs to be approximately 30 MeV/(mg/cm^2). More discussion of the electronic stopping, and the radiation ef-

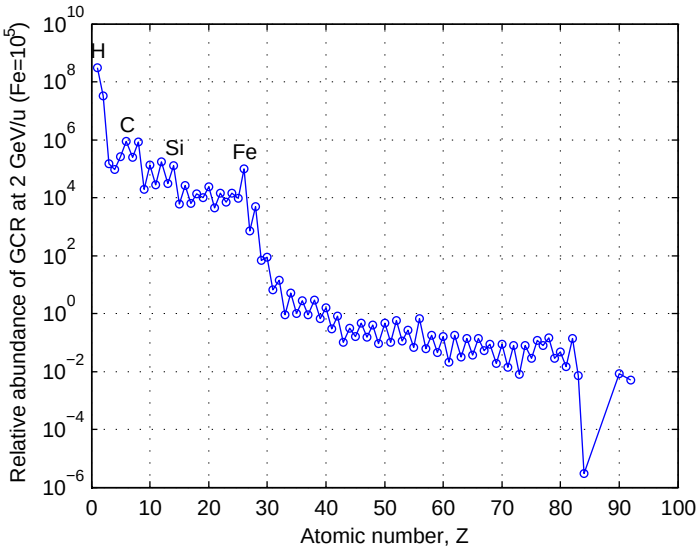

Figure 1.5: Relative abundance of different ion species in galactic cosmic rays as a function of atomic number at energies ∼2 GeV/u. Data are taken from [22].

fects and their testing in electronics are presented in Chapters 2, 3 and 4, respectively.

1.1.4 Space weather

The space radiation environment, *the space weather*, is constantly monitored by various dedicated satellite systems, such as the *Geostationary Operational Environmental Satellites* (GOES) and the *Solar and Heliospheric Observatory* (SOHO). For instance, the *Space Weather Prediction Center* (SWPC), uphold by the *National Oceanic and Atmospheric Administration* (NOAA), provides a service for real-time monitoring and forecasting of space environment. Their webpages can be found at http://www.swpc.noaa.gov/. The online information about the status of the space radiation environment is crucial for modern satellite systems and also in some extent for the electronic and electrical systems on ground. The solar flares are not only a threat to the spacecrafts, but in case of intense flares (CMEs) the *geomagnetically induced currents* (GIC) in Earth can affect also power grids, telecommunication networks, pipelines and railways. The GICs and their effect in the powerlines in Finland has been discussed in Ref. [23]. The solar flares also increase the radiation levels in the atmosphere due to the increase in trapped particles in the Van Allen belts. The

well known and easily observable indication of increased atmospheric radiation is the *northern lights* also known as the *Aurora Borealis*. They are caused by the collisions of the energetic particles with the atmospheric atoms.

1.2 Atmospheric and ground level radiation

Particle radiation is not restricted only to space. At ground level and at high altitudes there exists both natural and man-made particle radiation. Despite the lower radiation levels compared to the space environment, especially in case of natural sources, the electronics has been shown to be affected by the radiation also in these regions. This section gives a brief introduction to the radiation sources existing at the ground level and in the Earth's atmosphere. First presenting a discussion on the natural sources, followed by a short contemplation of the artificial sources.

1.2.1 Cosmic rays

Although, the Earth's magnetic field deflects majority of the particle radiation coming from space, there is still a continuous shower of energetic particles present at high altitudes and even at ground level due to the GCRs and the solar activity. The atmospheric radiation was shown to increase with altitude already hundred years ago by Victor Hess, who also proved the radiation to be mostly of cosmic origin [24].

The probabilities for the primary cosmic ray particles (protons and heavy ions) themselves to penetrate the atmosphere are extremely low, but as they interact with atoms in the upper atmosphere they create secondary particles, such as *neutrons* and *muons*. These secondaries interact relatively weakly with matter and they are able to reach ground level and in some extent even penetrate into the Earth. Neutrons, as they are neutral particles, do not interact with matter via Coulomb forces and thus no primary ionization is produced by them. In turn, neutrons can indirectly produce ionizing effects via scattering with nuclei, elastically or inelastically. See more details in Chapter 2.

Already in 1979 Ziegler and Lanford in Ref. [25] suggested that the anomalous soft errors observed in *random-access-memories* (RAM) were caused by *atmospheric-neutrons*. They also predicted this effect, at that time considered quite minute, to become more pronounced in the future along with the technological evolution. In his review in Ref. [26], Normand discussed the impact of the two papers, Refs. [25, 27], to the activities of the electronics industry. Normand criticized that the susceptibility

of electronics to errors induced by atmospheric neutrons remained publicly unrecognized. Even though the vendors (e.g. IBM[28]) made extensive studies about the subject early on, they published the results much later. Normand's paper presents several examples of soft error observations in memories and explains them with the atmospheric neutrons. The impact of atmospheric neutrons on scaled technologies has been discussed recently by Ibe *et al.* in Ref. [29], where based on their simulations they confirm Ziegler's postulate that the effect becomes more pronounced along with the technology scaling. Some anecdotal suggestions have been made by representatives from electronics industry about the increasing possibility of cosmic rays causing failures in the evolving automotive electronics if not taken into account in the design [30]. This aspect is also discussed in Ref. [31, and references therein].

Obviously, the atmospheric radiation is more of a problem in avionics. After the solar flare occurred in late January 2012 (see the inset of Fig. 1.2), several airlines were forced to divert their flights from the polar routes due to increased radiation in the atmosphere[32]. The effects of cosmic rays on avionics has been discussed e.g. in Refs. [4, 33].

Apart from *neutrinos*, *muons* are the most abundant of the cosmic ray secondaries present on the ground[34]. Muon is a charged particle with the same charge as electron, and mass corresponding approximately 200 times the electron mass. The first results on muon-induced errors in microelectronics was published by Sierawski *et al.*[5], where artificially produced muon beam was used. Their results suggest that muons are not capable to cause problems in electronics manufactured by using the latest technologies (65 nm or 45 nm). However, they predicted the susceptibility to become higher in the future technologies.

1.2.2 Radionuclides in the soil

Although silicon is the second most abundant element (by weight) in the Earth's crust [35], the use of this excellent metalloid in semiconductor industry has exhibited some unexpected problems in the past. There are traces of radioactive elements present everywhere in the soil. Thus all bulk of materials contain small traces of radioactive particles even after refinement. The most concern is of U-238 and Th-232, and their radioactive daughter nuclides, such as Rn-220 and Rn-222.

Already in 1979, May and Woods reported in Ref. [27] that alpha particles emitted from the packaging materials were causing soft errors in random-access-memories (RAM) and charge-coupled-devices (CCD) (see more about soft errors in Section

3.6.2.1). It was shown that the packages, used at that time, contained these radioactive elements in the order of some *parts-per-million*. In 1982, also the metallization within the devices was demonstrated to be a possible source of radioactivity [36]. After these findings the reduction of these radiation sources and mitigation of their effects has been done typically by controlling the purity of the materials and/or *error-detection-and-correction* (EDAC) applied on the devices. In addition, protective coatings on the device surface have been introduced in order to minimize the problem[37]. But, not only these "auxiliary" materials are posing the threat. Even after the refining chain of silicon there is always some traces (∼parts-per-billion) of these unwanted radioactive residues present in the devices, which in turn have also demonstrated to cause soft errors in modern memories[38, and references therein].

Radon is a well-known perpetrator when considering health issues. Recent study presented in Ref. [39] has shown very little concern of ambient radon to induce errors in microelectronics via diffusion through the packaging. Nevertheless, while being an *inert atom*, Rn can diffuse into materials. Also its daughter nuclides, usually positively charged ions, can adhere to surfaces [40]. These radioactive elements has to be taken into account in devices with bare dies such as particle detectors. For example after storing a *Micro-Channel Plate* (MCP) in ambient conditions, the accumulated radioactive residues, although very small amounts, in the device surface and its pores can cause problems when taking the detector in use. Typically after ambient storage, a MCP requires few days of waiting in vacuum before full operation voltage (∼few kV) can be applied. This is partly due to possible high ionization events induced by alpha-particles in the Rn decay chain, which could damage the detector.

These problems, caused by the radioactive residues, are nearly impossible to avoid completely. Only very strict control of the used materials and sufficient EDAC techniques are effective in assuring the tolerance against these radiation sources.

1.2.3 Thermal neutrons

Eventually, part of the secondary neutrons, produced by either aforementioned cosmic rays or decay processes of radionuclides in the soil, lose their energy and become thermalized. These so called *thermal neutrons* have average kinetic energy of ∼25 meV, which equals the most probable energy for a free particle at room temperature (∼290 K). It was discovered by Fermi *et al.*(see Ref. [41, and references therein]) that slow neutrons are more effectively interacting with matter than high energy ones. Thermal neutrons can initiate nuclear reactions, if they are captured by target nuclei.

Depending on the target atom, the reaction products can be either gamma or particle radiation. In case of particle radiation, especially with fission products, the effect of ionization becomes substantial and gives rise to problems in electronics. The most notorious example of this is the neutron induced fission in boron-10 described by

$$^{10}_{5}\mathrm{B} + ^{1}_{0}\mathrm{n} \longrightarrow ^{7}\mathrm{Li} + ^{4}\mathrm{He} + \gamma.$$

This neutron capture in ^{10}B has a exceptionally high cross-section in comparison to other materials. It has been shown, in Ref. [42], to be a considerable source of errors in *Static-Random-Access-Memories* (SRAM). Due to the high fluxes of low energy neutrons and their high penetration capability, the only way to mitigate this problem is to avoid using ^{10}B in the devices. Boron is very widely used dopant in semiconductors and also present in the *borophosphosilicate glass* (BPSG) commonly used as an insulator in standard manufacturing processes. Although, naturally ^{11}B is the most abundant ($\sim 80\%$) boron isotope, the used boron has to be carefully refined in order to minimize the problems caused by thermal neutrons.

1.2.4 Artificial radiation sources

In addition to the natural sources, there is plentiful of man-made radiation present in the ground-level. This can be either used in testing of the radiation sensitivity in electronics, or it can unintentionally cause problems in the electronic systems. A list of the selected man-made radiation sources is given below.

- accelerators, e.g. **cyclotrons** (**heavy ions**, protons, neutrons, electrons), synchrotrons (x-rays), x-ray tubes
- lasers
- enriched radionuclides (photons, electrons, neutrons, protons, **heavy ions**)
- nuclear power plant (photons, neutrons)
- nuclear weapons (e.g. Operation Dominic [43, 44])

In the list above the main focus points of this work are in boldface. Extra care has to be taken of electronic systems used in the vicinity of these artificial radiation sources in order to assure their operation. E.g. in nuclear power plants or accelerators, such as the *Large Hadron Collider* at CERN, the failures in the electronics has to be minimized. The radiation sensitivity of used electronics has to be either tested, or electronics need to be manufactured *Radiation Hard* (RadHard). The utilization of

accelerators, namely cyclotrons, and enriched radionuclides in the radiation-effects testing of electronics is discussed in Section 4.

2 Energetic charged particles and matter

While an energetic charged particle traverses matter it loses energy via different mechanisms. A simple illustration of energy loss is given in Fig. 2.1, where an ion with initial energy of E penetrates a slab of material with a thickness of Δx. The final energy of the ion is $E - \Delta E$. If the thickness is considered as *infinitesimal*, $\mathrm{d}x$, the energy loss $\Delta E \to \mathrm{d}E$. From this the total *stopping force* is defined as

$$-\left.\frac{\mathrm{d}E}{\mathrm{d}x}\right|_{total} = \sum_i -\left.\frac{\mathrm{d}E}{\mathrm{d}x}\right|_i, \tag{2.1}$$

where i denote the different energy loss mechanisms according to [45], and which are listed below:

1. **Excitation and ionization of target atoms**
2. **Projectile excitation and ionization**
3. Electron capture
4. **Recoil loss ('nuclear stopping')**
5. Electromagnetic radiation

Additionally part of the energy loss can also go to the following reactions:

6. **Nuclear reactions**
7. Chemical reactions

As in this work primarily the interactions between heavy ions and matter are considered at energies of hundreds of keV/u to tens of MeV/u, the mechanisms 1–4 are the most interesting ones. More over, this chapter concentrates on mechanisms 1 and 2 as they constitute most of the electronic energy loss, which dominate above all others in the energy ranges and ion species studied in this work. The nuclear reactions (6) are discussed, as there is evidence of their contribution in the errors observed in modern electronics. Also the nuclear stopping (4.) is briefly introduced.

Particle radiation can change the physical properties of the target material temporarily or permanently. Usually ionizing radiation (processes 1–3) is considered to be non-destructive as it is mainly breaking the covalent bonds in the target material. Depending on the material, these broken bonds are self-reassembled immediately after

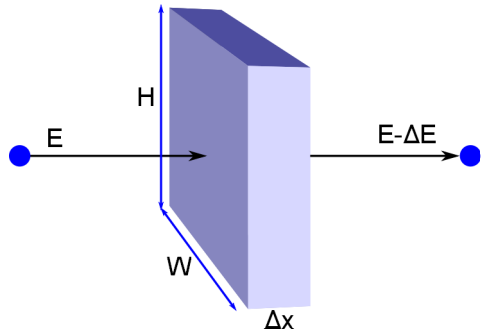

Figure 2.1: Illustration of the energy loss of energetic particle with initial energy of E after passing through a slab of material with thickness of Δx.

their creation or they can be fixed by high temperature anneal. In reality, heavy ions also create permanent changes in the target. This is, in one hand, due to the high density of ionization caused by the high-Z ions, which induces material modification. On the other hand, energetic target recoils, due to the nuclear stopping (4), may rearrange the atomic structure of the target. In some cases, depending on their nature, these atomic defects can also be repaired by high temperature annealing. More discussion on the effects of energetic heavy ions in materials and electronic devices is presented in Section 3.

2.1 Stopping nomenclature

Before proceeding, the terminology of the energy loss used in this work will be clarified. Officially the energy loss of an ion in matter is called *the stopping power*. In the past there has been intensive discussions on the terminology, whether the term *stopping power* should be replaced by *stopping force* [46]. In this work the term *stopping force*, or simply *stopping*, is used.

2.2 General theories for electronic stopping

When considering the mean energy loss per unit length for a projectile due to the collisions with target electrons (i.e. electronic stopping force), it is generally written:

$$\begin{aligned} -\frac{\mathrm{d}E}{\mathrm{d}x}\bigg|_{elec} &= NZ_2S \\ &= \frac{1}{4\pi\epsilon_0^2}\frac{Z_1^2e^4}{m_ev^2}NZ_2L \\ &= 3.0705\cdot10^{-4}\frac{Z_1^2Z_2}{A_2\beta^2}L, \end{aligned} \tag{2.2}$$

where

$Z_{1,2}$	are the atomic numbers for the projectile (1) and target (2),
A_2	is the mass number of the target atom,
N	is the atomic density of the target material,
v	is the velocity of the projectile,
S	is *electronic stopping cross-section* in units of [*energy*$\times$*area*],
e and m_e	are the *elementary charge* and the *electron rest mass*, respectively,
ϵ_0	is the vacuum permittivity, and
L	is the theory dependent *dimensionless* stopping number (see below).

Furthermore, $\beta = v/c$, and c is the speed of light in vacuum. The electronic stopping force in Eq. (2.2) is given in units of MeV/(mg/cm^2). Sophisticated reader might notice that this is the unit for mass stopping force and not for stopping force (MeV/µm). Let's clarify here that in this work the concepts of mass stopping force and stopping force are used interchangeably, although technically there is a difference. Strictly speaking, the mass stopping force is the stopping force divided by the density of the target material (i.e. $-\frac{1}{\rho}\frac{dE}{dl}$).

In the next sections the fundamental stopping theories by Bohr, Bethe, and Bloch are introduced. Also description of a semi-empirical model developed in this work is given below.

2.2.1 Bohr's classical theory

In 1913 Niels Bohr formulated his original theory on *the decrease of velocity of moving electrified particles on passing through matter*[47], which he afterwards revised in Refs. [48, 49]. In this theory the energy loss of an ion is considered by means of

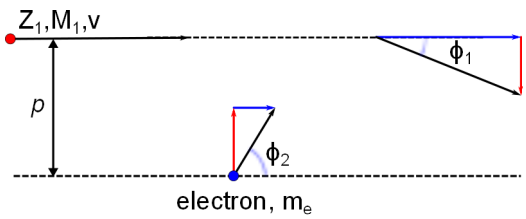

Figure 2.2: Rutherford scattering of a target electron in a heavy-ion collision in *lab frame*. The scattering angles are not in scale.

classical conservation laws of energy and momentum. The next treatment is adopted from the Bohr's original works and the work done by Sigmund in Refs. [45, 50].

The Bohr's model is *approximately* valid for velocities

$$\beta < 2Z_1\alpha, \tag{2.3}$$

where $\alpha \sim \frac{1}{137}$ is the *fine structure constant*. The lower limit is set by $\beta \gg \alpha$. We can see that in our case (i.e. heavy ions with Z_1 ranging from 7 up to 54, in the energy range from 100 keV/u to 10 MeV/u, corresponding β values of ~ 0.015 and ~ 0.15, respectively), these two criteria are nearly fulfilled. Only N-ions ($Z_1 = 7$) violate the limit set by Eq. (2.3) at the highest energies (see more in Section 5.1.3).

In the classical picture the target electrons are treated as harmonic oscillators with resonance frequencies of ω_i. The collisions are considered as elastic. The energy transfer is a function of the impact parameter, p. The impact parameter is the closest distance between initial projected path of the projectile, and the electron. In this case the electron is assumed stationary, and the path of the projectile as a straight line during the collision event. The impact parameter in a collision is illustrated in Fig. 2.2. First we define the *collision diameter*

$$b = \frac{1}{4\pi\epsilon_0}\frac{2e^2Z_1}{m_0v^2}, \tag{2.4}$$

where $m_0 = \frac{M_1m_e}{M_1+m_e}$ is the *reduced mass*, which in case of $M_1 \gg m_e \Rightarrow m_0 \approx m_e$. M_1 is the mass of the projectile. The energy loss of an ion in a single collision with an electron is divided in two parts *close* and *distant* collisions. The division in these two regions is chosen at $p = p_0$. In the close collisions (i.e. $0 < p < p_0$) the energy transfer is assumed to be much higher than the electron binding energy, $\hbar\omega_i$, and the electron is considered as free. The dependence of electron scattering angle, ϕ_2, on the impact

parameter has been derived from the *Rutherford scattering*, and the conservation laws of momentum and energy, which give

$$\tan\phi_2 = \frac{2p}{b}. \tag{2.5}$$

On the other hand, it can be expressed in terms of energy transfer, T, by

$$\cos\phi_2 = \sqrt{\frac{T}{\Gamma E_k}} \tag{2.6}$$

where $E_k = \frac{1}{2}M_1v^2$ is the kinetic energy of the projectile and $\Gamma = 4\frac{M_1m_e}{(M_1+m_e)^2}$ is the energy transfer efficiency. From the Eqs.(2.5) and (2.6) the energy transfer in close collisions can be defined as the following

$$T_{close}(p) = \Gamma E_k \left(\frac{b}{2p}\right)^2 \frac{1}{1+\left(\frac{b}{2p}\right)^2},\ 0 < p < p_0. \tag{2.7}$$

For heavy ions, where $M_1 \gg m_e$, $\Gamma \approx 4\frac{m_e}{M_1}$, the maximum energy transfer at $p = 0$ is

$$T_{max} = \Gamma E_k = 2m_ev^2. \tag{2.8}$$

Since the *stopping cross-section* is defined as

$$S = \int 2\pi p dp T, \tag{2.9}$$

and by introducing Eg.(2.8) into Eq. (2.7), we get

$$S_{close} = \int_0^{p_0} 2\pi p\ dp\ T_{close}(p) = m_ev^2\pi b^2 \frac{1}{2}\ln\left[1+\left(\frac{2p_0}{b}\right)^2\right]. \tag{2.10}$$

In case of distant collisions the electrons are considered as the above mentioned harmonic oscillators. The treatment is far more complicated compared to the close collisions, and only the result is described in the following. The energy transfer in the distant collisions is described by

$$T_{dist}(p,\omega_i) = \Gamma E_k \left(\frac{b}{2p}\right)^2 \left(\left[\frac{\omega_i p}{v}K_0(\frac{\omega_i p}{v})\right]^2 + \left[\frac{\omega_i p}{v}K_1(\frac{\omega_i p}{v})\right]^2\right),\ p > p_0, \tag{2.11}$$

where K_n are the modified Bessel functions[1]. The complete derivation of the Eq. (2.11) is presented in [50]. Introduction of Eq. (2.11) into Eq. (2.9) gives

$$S_{dist}(\zeta_i) = \int_{p_0}^{\infty} 2\pi p \; dp \; T_{dist}(p) = m_e v^2 \pi b^2 \zeta_0 K_0(\zeta_0) K_1(\zeta_0) \overset{2}{\simeq} m_e v^2 \pi b^2 \ln\left(\frac{2e^{-\gamma}}{\zeta_0}\right), \tag{2.12}$$

where $\zeta_0 = \frac{\omega_i p_0}{v}$ and $\gamma = 0.5772\ldots$[3]. By introducing a dimensionless parameter $\xi_i = \frac{2v}{b\omega_i}$ the total electronic stopping cross-section can be written

$$S_{total}(\xi_i) = S_{close} + S_{dist} = \frac{1}{4\pi\epsilon_0^2}\frac{e^4 Z_1^2}{m_e v^2}\left[\frac{1}{2}\ln\left(1+\zeta_o^2\xi_i^2\right) + \ln\left(\frac{2e^{-\gamma}}{\zeta_0}\right)\right]. \tag{2.13}$$

Now we have derived the *stopping number* for the classical Bohr's theory as

$$L_{Bohr}(\xi_i) = \frac{1}{2}\ln\left(1+\zeta_o^2\xi_i^2\right) + \ln\left(\frac{C}{\zeta_0}\right), \tag{2.14}$$

where $C = 2e^{-\gamma} \simeq 1.1229$. At values $\xi_i \gg 1$ Eq. (2.14) approaches

$$L_{Bohr}(\xi_i) \simeq \ln\left(C\xi_i\right), \tag{2.15}$$

which is the familiar expression for the Bohr's stopping number. Now summing over all electrons in the target atom we get

$$L_{Bohr} = \sum_i f_i \ln\left(C\xi_i\right) = \ln C\xi, \tag{2.16}$$

where f_i is the weighting factor[4] corresponding an individual electron. We can write,

$$\xi = \frac{m_e v^3}{Z_1 I \alpha c}, \tag{2.17}$$

where $I = \hbar\omega_0$ is the material dependent *mean excitation energy* corresponding the mean frequency. In this work the focus is in silicon target, thus in the calculations value of $I = 173$ eV, taken from page 39 in Ref. [45], is used if not stated otherwise.

There is a drawback in Eq. (2.16) at low projectile velocities, i.e. $\xi \leq 1/C \Rightarrow L_{bohr} \leq 0$.

[1] $K_n(x) = \int_0^\infty \exp[-x\cosh(t)]\cosh(nt)\mathrm{d}t$

[2] Product of Bessel functions can be expressed by its series expansion and only taking into account the leading term, i.e. $xK_o(x)K_1(x) = \ln\left(\frac{2e^{-\gamma}}{x}\right) + O[x]^2 \simeq \ln\left(\frac{2e^{-\gamma}}{x}\right)$

[3] γ is the Euler-Mascheroni constant usually known as the Euler's constant (not to be confused with the *Euler's number* $e = 2.71828\ldots$)

[4] $\sum_{i=1}^{Z_2} f_i = 1$

This flaw can be solved by making an *educated guess* for the integration limit, $p_0 = \frac{Cv}{\omega_i}$ ($\Leftrightarrow \zeta_0 = C$), in Eq. (2.10). This limit is in fact very close to the *Bohr's adiabatic radius*, which typically is given $\sim \frac{v}{\omega_i}$. By using this selection the Eq. (2.16) reduces to

$$L'_{Bohr} = \frac{1}{2} \ln \left[1 + (C\xi)^2 \right], \tag{2.18}$$

which is exactly the same expression as presented in Ref. [45], where the derivation has been made from the works of Lindhard and Sørensen in Ref. [51]. The selection of the integration limit, done above, gives the impression that the energy transfer in distant collisions would be zero (i.e. $T_{dist} \sim 0$), which is not true.

2.2.2 Bethe's quantal stopping theory

Probably the most widely known and used notation for the electronic stopping force is the *Bethe formula*, where the stopping number is

$$L_{Bethe} = \ln \frac{2m_e v^2}{\hbar\omega_0}. \tag{2.19}$$

This equation is based on the quantum mechanical treatment of the interaction between the projectile and the target electrons. It should be noted that this equation is valid when $2m_e v^2 \gg \hbar\omega_0$. The derivation of this equation is skipped in this work. Similarly to the expressions for the *Bohr's classical stopping*, a comprehensive derivation of Eq. (2.19) is presented in Refs. [45, 50].

2.2.3 A simple approach with modified Bohr's expression

A slightly different approach for estimating stopping force of solids for heavy ions has been proposed in Ref. [52] by the author of this thesis. There it is shown for wide range of ions and solid targets that the stopping number can be estimated with a reasonable accuracy by using relation

$$L_s = \kappa \ln \left(1 + a \frac{Z_2^{1/2}}{Z_1^{1/3}} C\xi \right), \tag{2.20}$$

where

$$\kappa = b_1 \cdot \sqrt{1 + \ln \left(b_2 \frac{Z_1}{Z_2} \right)}, \tag{2.21}$$

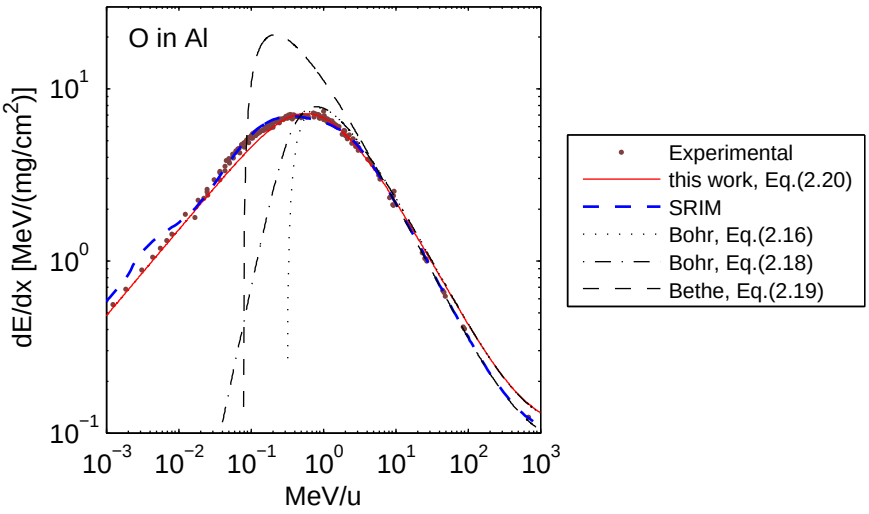

Figure 2.3: Experimental and estimated electronic stopping force of aluminum for oxygen ions. Estimations are calculated by using different models discussed above and also the SRIM-code [53]. Experimental data are taken from Ref. [54].

and

$$\begin{aligned} a &= 0.2853 \\ b_1 &= 1.1209 \\ b_2 &= 0.2021 \end{aligned} \tag{2.22}$$

are parameters derived from the data fit. An example of the good agreement of this model with the experimental data is demonstrated in Fig. 2.3, where the electronic stopping force of aluminum for oxygen is presented. In this graph there is experimental values plotted with estimations from different sources. The agreement between the model described by Eq. (2.20) with experimental values and the estimates from the SRIM-code[53] is fairly good considering the simplicity of the model. The estimates extracted from above mentioned Bohr's and Bethe's models exhibit good agreement only at high energies for the latter and only a reasonable agreement for the former at energies around 10 MeV/u. In Ref. [52] the model, described by Eqs. (2.20) and (2.21), is shown to work for He, O, Ar, Kr, and Xe-ions in carbon, aluminum, nickel and gold targets with relatively good accuracy. Despite the resemblance between the Bohr's expression in Eq. (2.18) and Eq. (2.20), the physical basis for the latter is

not understood, if there is any. The possible physical relations behind the model will be further investigated in the future by the author. Nonetheless, due to the apparent feasibility and the simplicity of this expression, it was employed in this work to construct a semi-empirical stopping force prediction tool (see Section. 5.1.3).

2.2.4 Bloch correction

Obviously, the theories by Bohr and Bethe, give very different outcomes. The Bethe stopping, defined in Eq. (2.19), is proved to be valid at velocities $\beta > Z_1\alpha$, which is essentially the velocities excluded by the Bohr criterion in Eq. (2.3). The transition from the Bethe to the Bohr regime has been accomplished by using correction developed by Bloch in Ref. [55]. This is given by

$$L_{Bloch} = L_{Bethe} + \Delta L_{Bloch} = L_{Bohr} + \Delta L_{invBloch}, \tag{2.23}$$

where

$$\Delta L_{Bloch} = \psi(1) - \mathrm{Re}\psi\left(1 + i\frac{Z_1\alpha}{\beta}\right) \tag{2.24}$$

and

$$\Delta L_{invBloch} = \ln\frac{Z_1\alpha}{\beta} - \mathrm{Re}\psi\left(1 + i\frac{Z_1\alpha}{\beta}\right). \tag{2.25}$$

In above $\psi(x) = \frac{\mathrm{d}\ln\Gamma(x)}{\mathrm{d}x}$ with $\Gamma(z) = \int_0^\infty t^{z-1}e^{-t}\mathrm{d}t$, and Re denotes the real part. The difference between Bohr's and Bethe's model is illustrated in a universal plot presented in Fig. 2.4 with experimental and semi-empirical data taken from Refs. [53, 54, 56, 57]. Also the curve derived from the model, described in Ref. [52] and in Section 2.2.3 above, is plotted for comparison. It can be seen from this figure that Bethe's model describes the stopping with good accuracy at velocities $\beta > 2Z_1\alpha$, as expected. On the other hand, at low velocities experimental values diverge from stopping numbers given by both Bethe's and also Bohr's model, described by Eqs.(2.19) and (2.16), respectively. Also the Eq. (2.18) exhibits deviation from the experimental data, especially for Xe-ions. A fairly good agreement is achieved by using expressions presented in Section 2.2.3. However, this model fails at higher velocities when approaching the *Bethe region*, which is expected. Because in this work the stopping force for heavy ions is studied at velocities $\frac{\beta}{\alpha Z_1} \lesssim 2$, the deviation from the Bethe's model at high velocities is not an issue. This picture supports the use of the model described by Eqs. (2.20) and (2.21) as a basis for parameterization of heavy ion stopping, instead of Bohr's model.

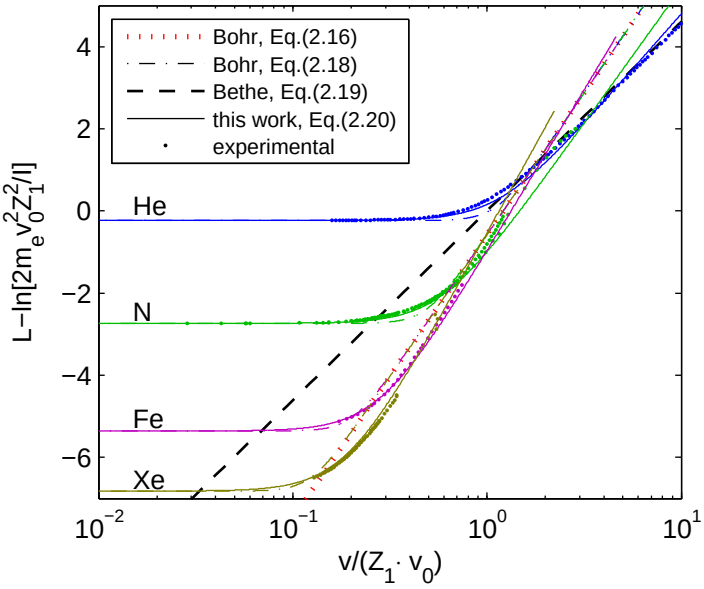

Figure 2.4: Universal plot for stopping numbers derived from different models (lines) and experiments (dots). The thick dotted red, and the dashed black lines are extracted from the Eqs.(2.16) and (2.19), respectively. The experimental (N, Fe and Xe-ions) and semi-empirical (He-ions) stopping numbers are derived from the electronic stopping force values taken from Refs. [54, 56, 57] and [53], respectively. The curves corresponding each of the ions are calculated by using Eq. (2.18) (dash-dot) and Eq. (2.20) (solid).

2.2.5 Effective charge of the projectile

When a particle traverses matter, part of its electrons are stripped away, and the ions charge state fluctuates around an equilibrium. In a simple picture, the electrons which have their orbital velocities above the projectile velocity are considered to move along with the ion and the rest are stripped away [58]. The equilibrium charge can be described by e.g. the *Thomas-Fermi* relation

$$\overline{q} = Z_1 e \left[1 - \exp\left(\frac{-\beta}{\alpha \cdot Z_1^{2/3}} \right) \right] \tag{2.26}$$

where Z_1 is the atomic number of the moving particle. More sophisticated formulas are available, e.g. in [59], but for this work the Eq. (2.26) is sufficient.

At first glance, when considering the $\frac{Z_1^2}{\beta^2}$-dependence in the Eq. (2.2), it seems

that the electronic stopping is heavily governed by the charge state of the projectile. Because of this, the concept of *effective charge* was introduced, which in Ref. [60] has been considered to be closely related with the equilibrium charge. Thus from Eq. (2.26), the effective charge ratio can be written as

$$\eta_{TF} = 1 - \exp\left(\frac{-\beta}{\alpha \cdot Z_1^{2/3}}\right). \tag{2.27}$$

The derivation of effective charge ratio from the experimental stopping data for ions was defined by Northcliffe in Ref. [61], and e.g. in [62] it is written in form

$$\eta^2_{exp} = \frac{Z_1^{-2} S(Z_1, Z_2, \beta)}{2^{-2} S(2, Z_2, \beta)}, \tag{2.28}$$

where $S(Z_1, Z_2, \beta)$ is the experimental stopping cross-section for the projectile (Z_1) moving in a medium (Z_2) with a velocity of β. In the denominator there is the tabulated stopping cross-section for α-particles at the same velocity as the Z_1-projectile. The α-particles are considered to be fully stripped from electrons, which is a reasonable assumption at velocities, where heavy-ion stopping is dominated by the electronic stopping force. This scaling rule has been widely used in order to estimate the electronic stopping force for heavy ions.

In the stopping theories, discussed above, the projectile is considered as a bare ion. By introducing the Eq. (2.2) in the Eq. (2.28) effective charge ratio for the bare ion can be written in a form

$$\eta^2_{bare} = \frac{L(Z_1, \beta)}{L(2, \beta)}. \tag{2.29}$$

If the effective charge would contribute in the stopping force strictly as the scaling rule in Eq. (2.28) implies, η_{bare} should be at unity for all velocities. The effective charge ratios calculated with Eqs. (2.27), (2.28) and (2.29) are plotted in Fig. 2.5 for N-ions in silicon at velocities of $0.02 < \beta < 0.2$. The results in the Fig. 2.5 show that there is no theoretical support for the scaling rule to be valid for high values of Z_1. This is also proven in Ref. [62, and references therein], where a detailed discussion on the dependence of stopping force on the ion's charge state is presented.

On the other hand, practice has shown that the scaling rule, given in Eq. (2.28), can be used as an estimation tool. One just needs to bear in mind the limitations of the concept when dealing with semi-empirical modeling of the heavy-ion stopping.

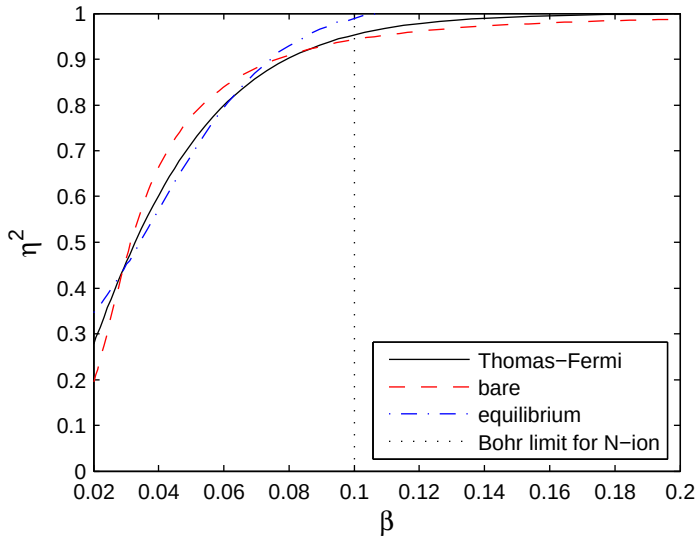

Figure 2.5: Effective charge ratios for nitrogen in silicon extracted from Eqs.(2.27) (solid), (2.29) (dashed) and (2.28) (dash-dot). The classical limit described by the Bohr critetion in Eq. (2.3) is marked with the dotted line.

2.3 Nuclear stopping force

The nuclear stopping is the part of the projectile's energy loss due to *Coulombic interaction* between the target and the projectile nuclei. With a similar treatment, as discussed in Section 2.2 for the electronic stopping, a general equation for nuclear stopping force can be written in form

$$-\frac{\mathrm{d}E}{\mathrm{d}x}\bigg|_{nucl} = \frac{1}{4\pi\epsilon_0^2}\frac{Z_1^2 Z_2^2 e^4}{M_2 v^2} N L_{nucl}, \tag{2.30}$$

where the notations are the same as in Eq. (2.2) and in addition the M_2 is the mass of the target nucleus. The nuclear stopping relative to electronic stopping can be estimated by dividing Eq. (2.30) with Eq. (2.2) yielding a ratio of

$$\frac{-\frac{\mathrm{d}E}{\mathrm{d}x}\big|_{nucl}}{-\frac{\mathrm{d}E}{\mathrm{d}x}\big|_{elec}} = \frac{m_e}{M_2} Z_2 \frac{L_{nucl}}{L_{elec}} \approx 2.7 \cdot 10^{-4} \frac{L_{nucl}}{L_{elec}}. \tag{2.31}$$

From this it can be seen that the contribution of the nuclear stopping in the total stopping force is several orders of magnitude lower compared to the electronic stopping. This holds at projectile velocities considered in this work. The ratio of the

stopping numbers, and thus the nuclear stopping, becomes significant only at low velocities[45]. Eventhough, in the nuclear stopping process the energy lost by the projectile is transferred mainly to the kinetic[5] energy of the target nucleus and the recoil loses its energy partly via electronic stopping, the *ionization effect* is typically considered to be less significant (see more discussion in Section 3.5). Hence the nuclear stopping is not discussed in detail in this work.

2.4 Ion induced nuclear reactions

As listed on page 15, the ions can lose their energy also by inducing nuclear reactions. The cross-sections for the nuclear reactions are much lower compared to the ones for the other mechanisms discussed above, and they are typically neglected. This is especially the case for heavy ions. Nevertheless, in microelectronics the products from the nuclear reactions may induce failures (see Section 3.1.1). Thus the ion induced nuclear reactions will be briefly introduced here.

When considering positively charged projectile (Z_1, A_1, R_1) and target (Z_2, A_2, R_2) nuclei, there is a repulsive electromagnetic force acting on them. Here Z_i, A_i and R_i correspond to the atomic and mass numbers, and the radii of the nuclei, respectively. The radius of a nucleus is typically estimated

$$R_i = R_0 \cdot A_i^{1/3} \text{ fm}, \tag{2.32}$$

where R_0 is an empirical constant. In this work $R_0 = 1.2$ fm is used, which is a typical value. This constant can vary in the range 1 fm$< R_0 <$4.5 fm depending on the nuclei[64].

In order to a nuclear reaction to occur the nuclei need to be in close contact. This means that the *impact parameter* has to be less than the sum of the radii of the nuclei, $R = R_1 + R_2$, and the total kinetic energy in the system has to exceed the potential energy formed by the repulsive Coulombic force. This limit in the potential energy is called the *Coulomb barrier*, which can be estimated by

$$\begin{aligned} U_{CB} &= \frac{1}{4\pi\epsilon_0}\frac{Z_1 Z_2 e^2}{R} \\ &\approx 1.2\frac{Z_1 Z_2}{(A_1^{1/3} + A_2^{1/3})} MeV. \end{aligned} \tag{2.33}$$

[5] E.g. for silicon the minimum lattice binding energy is in the range of 10-20 eV [63]

From the conservation laws of momentum and energy, the threshold kinetic energy in the *laboratory-frame* for the projectile to overcome the Coulomb barrier can be written [64]

$$K_{cbt} = U_{CB} \cdot \left(1 + \frac{A_1}{A_2}\right). \tag{2.34}$$

For light projectiles, where $A_1 \ll A_2$, the kinetic energy threshold is essentially the same as the Coulomb barrier given by Eq. 2.33. Classical estimation for the maximum total cross-section for nuclear reactions is given by

$$\sigma = \pi R^2 \left(1 - \frac{K_{cbt}}{E_k}\right), \tag{2.35}$$

where E_k is the initial kinetic energy of the ion [65]. This applies when $E_k \geq K_{cbt}$. Eq. (2.35) gives an estimate for the upper limit for the total cross-section for all possible nuclear reactions.

There are several different types of nuclear reactions. In this work the most interesting reaction type is the *ion induced fission*, where relatively light particle (i.e. with low electronic stopping) produces higher-Z fragments after hitting a heavy target nucleus. The most typical example in the context of this work is the $Si(p, X)Y$-reaction, where a energetic proton induces reaction fragments by hitting a silicon nucleus. These fragments may experience higher electronic stopping force (i.e. they have higher LET) than the primary proton and thus their effect in the electronics is more severe (see more discussion in Section 3.1.1).

The equations given above can be used for rough estimation for the energy loss in the nuclear reaction processes. As an example, let's consider protons ($Z_1 = 1$ and $A_1 = 1$) at 30 MeV in silicon ($Z_2 = 14$, $A_2 = 28$). From Eqs. (2.33) and (2.34) we get K_{cbt} ≈4.309 MeV. By introducing this in Eq. (2.35) the cross-section for nuclear reactions becomes $\sigma \approx 6.23 \cdot 10^{-25}$ cm^2. If we now assume (unrealistically) that within this cross-section the proton loses its whole energy, we get the energy loss cross-section of $S_{react} \approx 1.87 \cdot 10^{-17}$ eV$\cdot$ cm^2. Respectively, the energy loss cross-section for the electronic stopping for protons in silicon, taken from the SRIM-code [53], is $S_e \approx 6.88 \cdot 10^{-16}$ eV$\cdot$cm^2. The ratio of energy loss cross-sections due to nuclear reactions and electronic stopping is now ~ 0.027. Already this rough and rather unrealistic estimation implies that the nuclear reactions are less pronounced compared to electronic stopping. In reality according to Ref. [66] the energy loss cross-section for the nuclear reactions, in case of 30-MeV protons in silicon, is $\sim 1.5 \cdot 10^{-19}$ eV$\cdot$cm^2, which gives the ratio of $\sim 2.1 \cdot 10^{-4}$. For heavier ions the ratio becomes even lower.

3 Radiation effects in materials and devices

In the preceding chapter the different interaction mechanisms between energetic particles and matter were discussed. This chapter will present different phenomena occurring in materials due to the energy deposition by these particles. In this work the studied materials were: *silicon* (Si) and *silicon dioxide* (SiO_2). In some examples in the text also other materials may be considered.

From the electronics point of view, the generation of *electron–hole pairs* (e–h) due to the energy deposition of any radiation quantum (photon or particle) is considered to be the dominant effect. The atomic displacements are in a minor role, which are discussed in Section 3.5.

When considering the influence of particle radiation in electronics, typically only the electronic stopping (mechanisms 1 and 2 in page 15) is taken into account. The electronic stopping force can be related directly to ionization, whereas nuclear stopping and other mechanisms are only causing ionization indirectly. Nuclear reaction products and elastic recoils can cause also ionization, but usually in case of heavy ions their contributions have been neglected. However, recently there has been an increasing interest toward their contribution as discussed in Ref. [67, and references therein]. The effects of nuclear reactions in materials and devices will be briefly discussed in Section 3.1.1.

3.1 Generation of electron–hole pairs

At room temperatures the energy gap in the silicon band structure is ~ 1.1 eV [68] and in SiO_2 the corresponding value is ~ 9 eV [69]. These are the minimum energies at which the upmost electrons in the *valence band* (VB) are excited to the *conduction band* (CB). The average energies required to generate an e–h pair in Si and SiO_2 are 3.6 eV [70] and 17 ± 1 eV [71], recpectively. This is called the *mean e–h pair creation energy*. When considering electronics and the e–h pairs introduced in them by radiation, there are three main criteria which need to be fulfilled in order to induce major ionizing radiation effects. These criteria are

(a) The deposited energy in a single encounter between atomic electron and radiation

quantum (i.e. ion, delta-electron or photon) has to exceed the band gap energy to produce an e–h pair. In practice, the number of generated e–h pairs is estimated by dividing the mean energy deposition with the *mean e–h pair creation energy*.

(b) The density of induced e–h pairs has to exceed the intrinsic free electron density of the target material. I.e. in metals the effect of ionization is negligible due to the intrinsically high count of free electrons.

(c) An electric field is required in order to collect the excess charge carriers.

Otherwise no *Single Event Effect* (SEE) and only limited amount of *Total Ionizing Dose*-effect (TID) will occur. *Displacement Damage Dose*-effect (DDD) may still occur as the atoms are dislocated in the target, which is mainly due to the nuclear stopping mechanisms. See more discussion on the different radiation effects categories in Section 3.6.

3.1.1 Nuclear reactions

Even if an ion is incapable to generate enough e–h pairs via electronic stopping mechanisms to cause problems in electronics, it may induce nuclear reactions as discussed in Section 2.4. In turn, the reaction products may be capable to produce high density plasma of e–h pairs. This is typically encountered with high-energy protons, which exhibit low electronic stopping, but still are capable of inducing errors in the devices. These errors originate from the $^{nat}Si(p, X)Y$ nuclear reactions, already mentioned above. An example of this phenomenon is presented in Fig. 3.1, where a *Single Event Upset* (SEU) cross-section curve from Ref. [72] for a 4 Mbit SRAM is plotted as a function of proton energy. In this figure it is seen that low energy protons (<20 MeV) are less capable to produce errors in the device than high energy protons, for which the cross-section (i.e. probability[1]) is saturated. The low energy behaviour is due to the *Coulomb Barrier*, discussed in Section 2.4, which was estimated to be ~ 4.3 MeV for protons in silicon(see page 28). This is roughly observed in Fig. 3.1, although the data are not precise enough to make solid conclusions. The saturation in the cross-section originates from the limitation in the electronic stopping force for the reaction products. E.g. if we consider the above mentioned reaction, the reaction product which has the highest capablility for energy deposition is *phosphorus* ($Z_1 = 15$). The maximum energy loss value, according to SRIM, for this ion is ~ 14.9 MeV/(mg/cm^2),

[1] more discussion on the Radiation Hardness Assurance testing and characterization of the radiation sensitivity of the devices is presented in Section 4

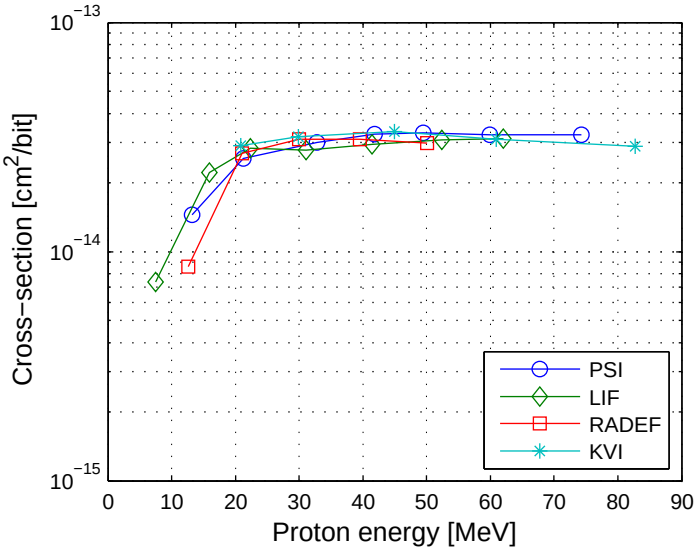

Figure 3.1: The cross-section for proton induced SEUs as a function of proton energy measured from 4 Mbit Atmel AT60142F SRAM used in the *SEU monitor* [73]. Data taken from Ref. [72].

which sets the upper limit for the deposited energy from the reaction. In reality, the probability for ${}^{nat}Si(p,\gamma)P$-reaction can be assumed to be lower compared to other reaction channels, but it enables the highest energy deposition. The accurate cross-section for this reaction channel is irrelevant in this context.

Another demonstration of the contribution of the nuclear reactions in the energy deposition of protons in silicon is presented in Fig. 3.2. In this figure the energy deposition of 30 MeV protons in silicon target is presented as simulated with the *MRED*-code [22] (see more on the MRED-code on page 43). The target was a slab of silicon with arbitrarily chosen dimensions of $100 \times 100 \times 20$ µm (W × H × Δx, see Fig. 2.1). The MRED-code enables the omission of the physics definitions for the nuclear reactions from the simulations. Thus the effect of nuclear reactions is possible to indicate. The spectrum for energy deposition in Fig. 3.2, with only the Coulombic scattering taken into account, exhibits a peak near 60 keV (i.e. 3 keV/µm). Which is comparable with the SRIM-estimation for the electronic stopping force of silicon for 30 MeV protons, which is $\sim$ 3.4 keV/µm. The spread in the spectrum is due to the *straggling* (see Section 3.2.2). The spectrum, where also the nuclear reactions are included in the simulations, shows the same primary ionization peak, but in addition there is a tail reaching up to 10 MeV (0.5 MeV/µm) of energy deposition. Although,

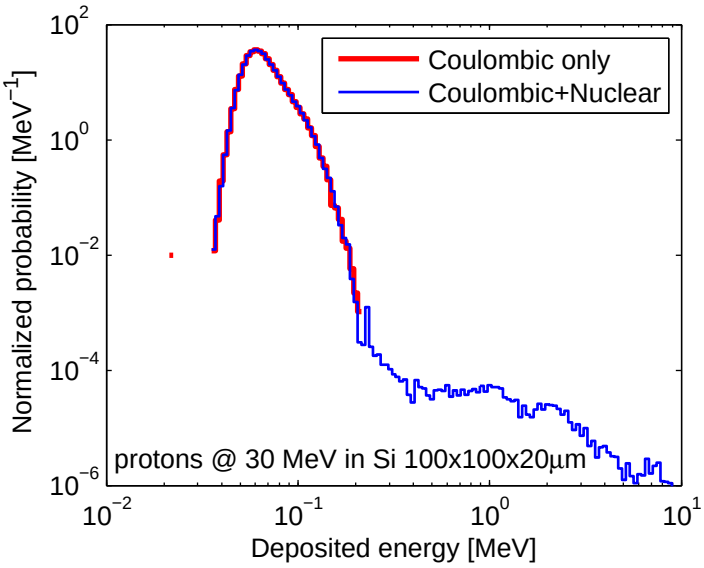

Figure 3.2: MRED-simulation of energy deposition by 30 MeV protons in silicon target with size of $100 \times 100 \times 20$ µm (W × H × Δx).

the probability of these events is orders of magnitude lower than of the primary ionization, in some cases they may turn out to be detrimental.

3.2 Linear Energy Transfer vs. electronic stopping force

When discussing the ion–matter interactions, historically in medical applications and also in radiation testing of microelectronics, the term *Linear Energy Transfer* (LET) has been used for the average *deposited* energy by the impinging particle per unit length. Typically the concepts of LET and electronic stopping force has been used interchangeably. The units of these two are the same, typically given in MeV/(mg/cm^2). However, there is a slight difference between these two, as the electronic stopping force quantifies the mean energy *lost* by the particle per unit length (in collisions with the target electrons). In case of bulky objects, e.g. old technology electronic components with large sensitive volumes (SV), where the energy is deposited, this is a valid choice. Historically in radiology the irradiated tumors have been considered to be bulky, thus justifying the use of mean energy *loss* as a metric for the mean energy *deposition*. For

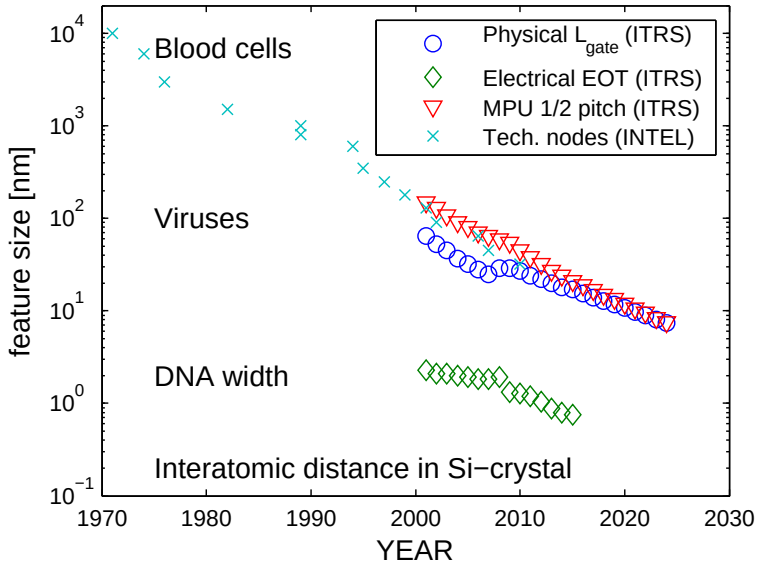

Figure 3.3: Scaling trends of some feature sizes in microelectronics, including physical gate length (L_{gate}), electrically equivalent oxide thickness (EOT) and half-pitch in MPU presented by the ITRS [83] and development of Intel's®technology nodes [84]. Also approximates of biological and physical feature sizes are illustrated.

a long time, in both communities, considering either radiation effects in the electronics [74–77], or the radiology [78–81], there has been discussions about the validity of LET as a metric and the comparability of LET and electronic stopping force. Although, in biology the radiation effects are shown[82] to be rather complicated, the similarity in these two different fields is in the feature sizes, where the radiation effects takes place. In radiology the noteworthy effects are considered to occur in very small dimensions, e.g. width of a DNA double strain, which have become comparable with the evolved feature sizes in modern microelectronics. In Fig. 3.3 the scaling trends of some key feature sizes in electronics set by the International Technology Roadmap for Semiconductors (ITRS)[83] and the Intel®corporation[84] are presented along with some typical feature sizes in nature for comparison. The applicability of LET in radiology is out-of-scope for this work. In the following section the dependence of feature size and projectile energy on the mean energy deposition, in a electronics point of view, is discussed.

3.2.1 Spatially restricted LET

The energy lost by an ion, discussed in Chapter 2, is transferred to kinetic (T_{kin}) and potential (T_{pot}) energy of the target electrons. In order to contemplate the spatial distribution of the deposited energy, first the energy transfer to the target electrons needs to be defined. This was done in Section 2.2.1. By rewriting the Eg.(2.7), the differential cross-section for *Coulomb scattering* becomes

$$\mathrm{d}\sigma = \mathrm{d}(\pi p^2) = \frac{1}{4\pi\epsilon_0^2}\frac{Z_1^2 e^4}{2m_e v^2}\frac{\mathrm{d}T}{(T)^2}, \quad 0 < T < \Gamma E, \tag{3.1}$$

which gives the probability for the projectile to transfer energy to a target electron in the range of $(T, T + \mathrm{d}T)$, which is dependent on the projectile's *velocity and charge*. Here $T = T_{kin} + T_{pot}$. From this the radial distribution of the energy deposition delivered by the *delta-electrons* can be derived. This has been done in Ref. [85], where an analytical formulation for the radial dose distribution has been given by

$$D_1(r) = \frac{1}{(4\pi\epsilon_0)^2}\frac{Z_1^{*2} e^4 N Z_2}{\alpha m_e c^2 \beta^2 r}\left[\frac{\left(1 - \frac{r+R_{th}}{R_{max}+R_{th}}\right)}{r + R_{th}}\right]. \tag{3.2}$$

This expression has been revised in Refs. [86, 87], in order to improve the agreement between the calculations, and *Monte-Carlo* (MC) simulations and experiments. The revision was made by introducing a semi-empirical correction as follows

$$D(r) = D_1(r)[1 + K(r)]. \tag{3.3}$$

This semi-empirical function was defined for other targets than water in Ref. [87], where

$$K(r) = A\beta^B(r - 0.1)e^{-r/C}, \tag{3.4}$$

with r given in *nanometers* and coefficients

$$\begin{aligned} A &= \begin{cases} 0, & \beta < 0.0081 \\ 112\beta - 0.899, & 0.0081 < \beta < 0.091 \\ 0.674\beta + 9.21, & \beta > 0.091 \end{cases} \\ B &= 0.215 \\ C &= 3.127 - 0.434\beta. \end{aligned} \tag{3.5}$$

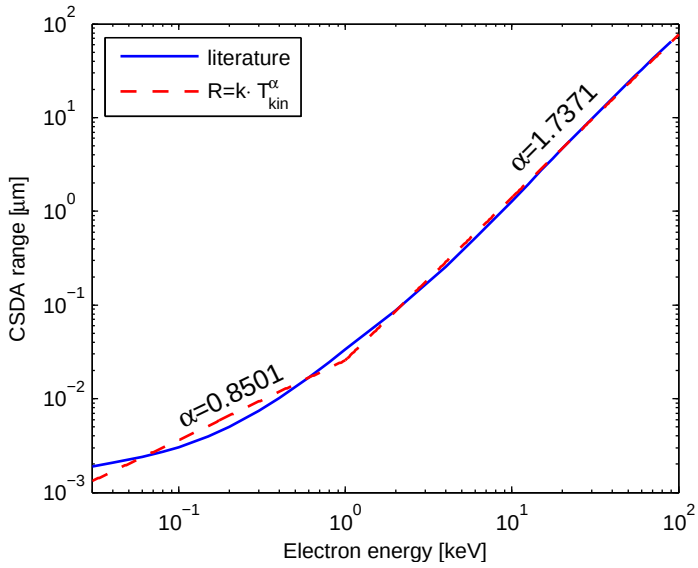

Figure 3.4: CSDA range of electrons in silicon as a function of electron energy. Data for silicon (solid) for the energy range from 30 eV to 10 keV are derived from the data published in Ref. [88]. The data for the energy range from 10 keV to 100 keV is taken from [89]. The dashed line represent the approximation defined by Eq. (3.6) used for the dose distribution calculations.

In Eq. (3.2) α is a coefficient describing the energy–range relation for the delta-electrons given by the following equation

$$R = k \cdot T_{kin}^{\alpha}, \tag{3.6}$$

where $k = 2.585$ µm·keV$^{-\alpha}$ is a coefficient given in Ref [86]. The electron range in silicon as a function of electron energy is plotted in Fig. 3.4, where the range is derived using the *Continuous Slowing Down Approximation* (CSDA). The data are taken from Refs. [88, 89]. To simplify the calculations, the range-energy relation in silicon is piecewise approximated with Eq. (3.6) by using $\alpha = 0.8501$ and $\alpha = 1.7371$ at energies below and above 1 keV, respectively. Now in Eq. (3.2), $R_{max} = k(\Gamma E)^{\alpha}$ gives the range of the electrons with maximum transfer energy. In Refs. [85–87] the value used for the minimum ionization energy is 10 eV. Thus $R_{th} = k(10\text{ eV})^{0.8501}$ is the lowest electron range limited by the minimum ionization energy of the outmost electrons in the target atom. The model assumes the velocity vectors of the delta-electrons to be perpendicular to the ion's trajectory, which is not entirely a valid

assumption due to the high scattering of moving electrons in medium. Nonetheless, the model is shown to agree with MC-simulations and experiments, supposedly due to the semi-empirical parametrization.

This model uses the *Barkas'* expression for *effective charge* of the projectile given by

$$Z_1^* = Z_1 \left(1 - e^{-125\beta \cdot Z_1^{-2/3}}\right), \tag{3.7}$$

which is slightly different from the *Thomas-Fermi* expression, given in Eq. (2.26).

From all this, the radial energy distribution deposited by the delta-electrons can be derived. Example calculations for xenon and nitrogen ions at 9.3 MeV/u, and for protons at different energies are presented in Fig. 3.5. Here the target material is silicon, and the radially deposited energy is described by the density of e–h pairs. The conversion is done by dividing the deposited energy with 3.6 eV/e–h pair (see page 29). In this graph it can be seen that the energy deposition is highly concentrated in the vicinity of the particle's trajectory. As the maximum delta-electron energy is dependent on the velocity of the projectile, the distribution exhibits also dependence on the ion velocity. This is observed in Fig. 3.5, where the end of each curve in x-direction corresponds to R_{max}. The elevation in the y-direction is due to higher total electronic stopping. The concentration of energy in the core of the ion track is also illustrated in Fig. 3.6, where the fraction of the deposited energy, f, within a radius R from the ion's trajectory is plotted as a function of the radius for different ion velocities (given in MeV/u). This is a universal graph and is valid for all ions regardless of their atomic number. The fraction of the deposited energy is defined as

$$f(R) = \frac{\int_0^R 2\pi r D(r) dr}{\int_0^{R_{max}} 2\pi r D(r) dr}. \tag{3.8}$$

Fig. 3.6 demonstrates the effect of (1) the size of the region, where the energy is deposited, and (2) the ion velocity on the LET. At the point, where curve reaches unity, the LET can be considered to equal the electronic stopping force. This is because in Eq. (3.8) the integration in the denominator gives the total energy deposition to the delta-electrons, i.e. electronic stopping force by definition. Thus by decreasing the size of the region of interest the deposited energy in this region becomes smaller than the electronic stopping. This is called the *spatially restricted LET*[75]. The implications of the restricted LET in the microelectronics can be portrayed by considering the *length of the chords*, l, in the sensitive volume. The *mean chord length*

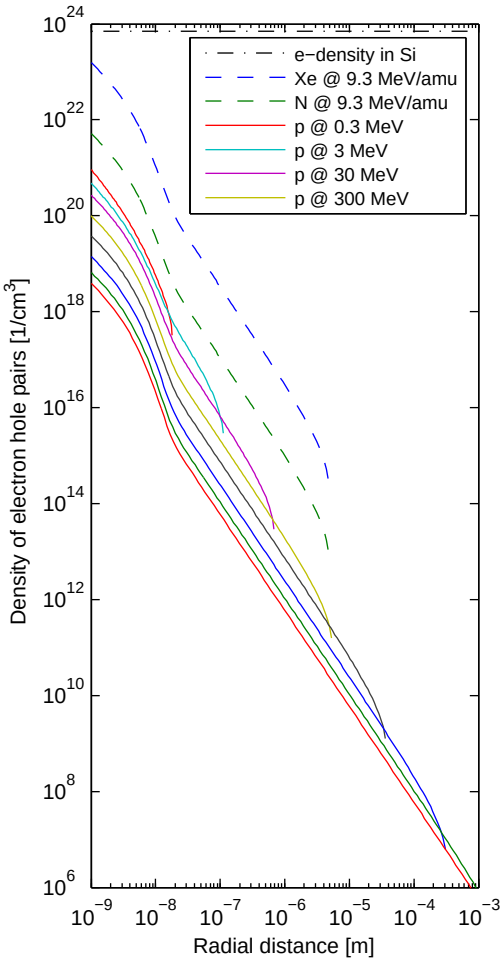

Figure 3.5: The radial distribution of e–h pairs in silicon generated by Xe- and N-ions at 9.3 MeV/u, and for protons at energies of 0.3, 3, 30 and 300 MeV as calculated from Eq. (3.3). The dash-dotted line represent the total electron density in Si, i.e. $\sim 7 \cdot 10^{23}$ cm^{-3}.

for any convex body has been derived in Ref. [74] to be

$$\bar{l} = \frac{4 \cdot V}{S}, \tag{3.9}$$

where V is the volume and S the surface area of the body. The mean chord length can be used for estimating the deposited energy in the SV, with size relative or smaller than the characteristic delta-electron ranges generated by the ion. In this approach the abscissa in Fig. 3.6 can be approximated with the mean chord length. Although the model above for the radial distribution of the energy deposition assumes the electrons to move perpendicular to the ion's trajectory, this is not exactly the case. In other words, there is also back- and forward-scattered electrons along the trajectory axis.

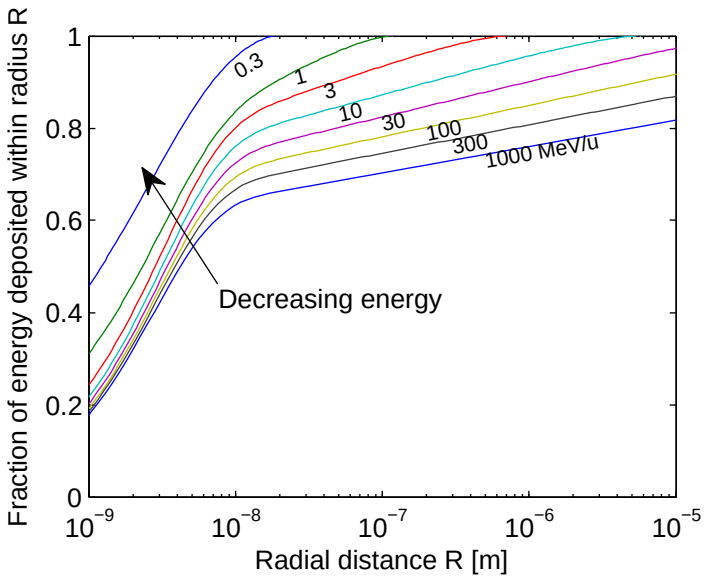

Figure 3.6: The fraction of deposited energy within radius from the ion track as a function of radial distance for ion velocities (or energies) 0.3, 1, 3, 10, 30, 100, 300 and 1000 MeV/u, from top to bottom, respectively. The curves are obtained by using Eq. (3.8).

Thus electrons (i.e. energy) are escaping the sensitive volume also in those directions.

3.2.2 Energy loss straggling

Energy loss of an ion in a single collision with the target electron is a stochastic event considered to follow the *Poisson statistics*. The expressions for the stopping force discussed in Chapter 2 give only the average energy loss per unit length. In relatively large volumes this applies, but when the volume size decreases also the randomness in the energy loss, *or* deposition, becomes significant, in addition to the *spatially restricted LET* discussed above.

A simple demonstration of the dependence of the SV size on the fluctuation in the deposited energy is presented in Fig. 3.7. Here results from *Geant4*-simulations[2][90, 91] for energy deposition of 1 MeV α-particles passing through silicon targets with different thicknesses are presented. The simulations were made by "bombarding" slabs of silicon (cf. Fig. 2.1) with α-particles. The lateral dimensions (W and H) in the slabs were much larger compared to the thickness (Δx). Thus from Eq. (3.9) the

[2] *GEometry ANd Tracking* toolkit for the simulation of the passage of particles

mean chord length becomes $\bar{l} = 2\Delta x$. The effect of the spatially restricted energy deposition is considered to be less significant in this case. It is seen in Fig. 3.6 that, for 1 MeV α-particles, from the total energy loss ~90% is deposited within 20 nm from the ion's trajectory. Thus we can assume in a SV with the mean chord length of >20 nm (corresponding the 10 nm slab) the deposited energy is more than this percentage of the average energy loss.

The shift in the spectra in Fig. 3.7 to higher energies for thicker targets originates from the decrease in the ion energy (thus increase in the stopping force) along the ion's path. This increases the total deposited energy in the thicker targets compared to the average energy loss for 1 MeV α-particles given by the SRIM-calculations, ~305 keV/µm. Also one should bear in mind that the descriptions for stopping in the SRIM and the Geant4 are slightly different, thus possibly yielding different average energy loss values. The physical descriptions for the nuclear reactions, discussed in Section 3.1.1, were omitted in these simulations.

The most distinct feature in this graph is the broadening of the spectra due to the straggling. The dependence of the target thickness on the broadening is clearly observed. In thin targets the relative fluctuation in the deposited energy around the average value increases with decreasing thickness. E.g. in Fig. 3.7 for the 10 nm silicon target some of the α-particles deposit even *twice* the average energy.

3.2.3 Applicability of LET

By combining the above mentioned aspects with the concept of LET, different regions governed by these mechanisms can be separated in the phase space determined by the ion's *velocity* and SV's *mean chord length*. These regions are depicted in Fig. 3.8, where the same definitions are used as in Refs. [74, 76]. The limits drawn in the graph represent so called 10 % thresholds where the individual effects (*spatial restriction* and/or *straggling*) are causing more the 10 % variation in the energy deposition defined by the *electronic stopping*. Here the limits are calculated for protons, α-particles and N-ions to demonstrate the dependence of the ion specie on the effects. The different regions in the graph are explained in the following list.

(1) For protons and heavier ions the LET can be considered to describe the energy deposition with sufficient accuracy.

(2) The effect of straggling contributes to the energy deposition for protons, but for heavier ions the use of LET is still valid.

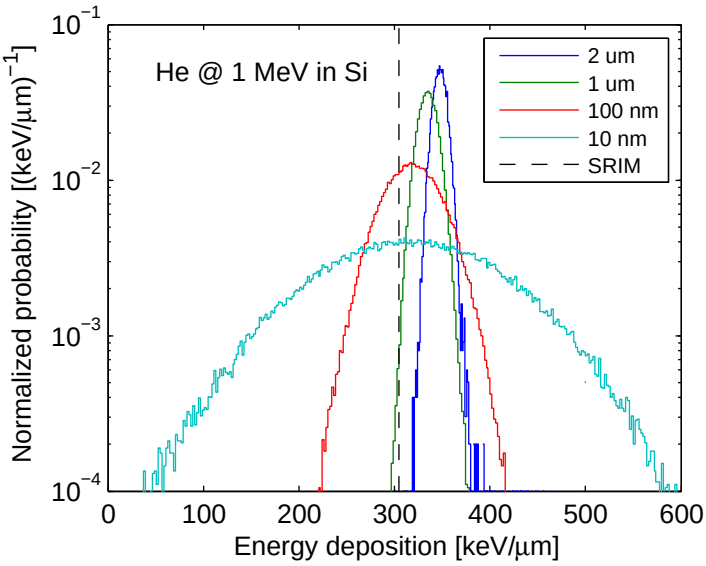

Figure 3.7: The spectra of deposited energy from Geant4-simulations for 1 MeV α-particles traversing silicon targets with thicknesses of 1 µm, 2 µm, 100 nm and 10 nm. The electronic stopping force value for 1 MeV α-particles, taken from SRIM, is plotted with dashed line, i.e. $\sim$305 keV/µm.

(3) The straggling for the α-particles becomes significant.

(4) The spatial restriction for the energy deposition becomes into play for all ions, the straggling for N-ions is still in a minor role.

(5) For N-ions all three concepts: the LET, its spatial restriction and the straggling, need to be taken into account when considering the energy deposition.

The above discussion shows that when the technology is approaching the *nano-scale* the conventional description of LET becomes increasingly insufficient to characterize the phenomena in the electronics. Thus more sophisticated models would be needed. At this point there is no simple concept to replace the LET as a metric used in the field of radiation effects in electronics.

3.2.4 Prediction tools for stopping force

Because no consensus has been reached on the alternatives among the community, the LET concept has yet remained in use in the characterization of the radiation effects. Moreover as the concepts of the spatially restricted LET and the straggling require

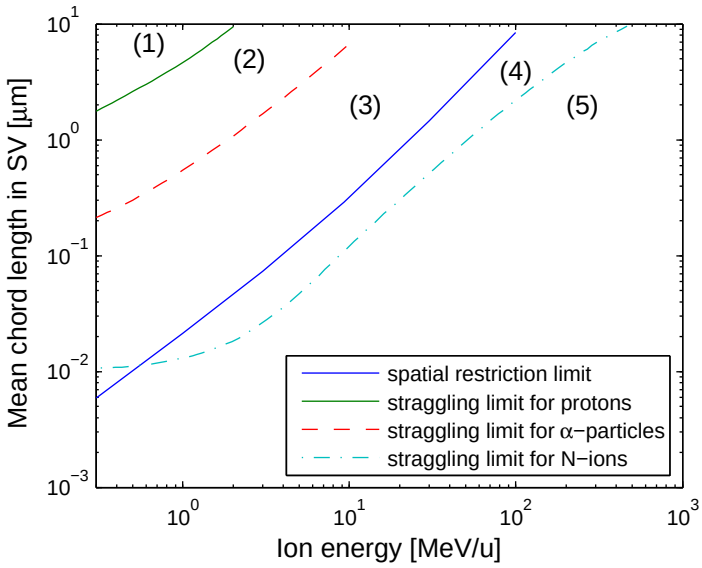

Figure 3.8: Regions of mean chord length and ion energy (MeV/u) where parameters LET, straggling and spatial restriction affect on the energy deposition. The different regions (1)–(5) are explained in the text.

information on the SV(s) in the studied structures, which is usually unavailable, the values of electronic stopping force are used as the LET. For estimating the electronic (and in some cases also nuclear) stopping for a given ion in a given target, there is a variety of tools available, both semi-empirical and theoretical, in addition to tabulations of experimental data. A collection of the prediction tools and data tables are presented in Table 3.1 with brief introductories. These are the ones that are mostly referenced in the literature, except the *ECIF Cocktail Calculator*. This tools is listed because it is part of this work, but has not yet attracted wide publicity. From the listed tools the SRIM-code has received the widest acceptance among the users, and at least in the radiation effects community it is the primary repository of stopping force values. This is due to its user-friendly interface, and in average, if all ion-target combinations are accounted for, its accuracy is fairly good.

In addition to these tools listed in Table 3.1, the *Geant4 simulation toolkit*[101] has become increasingly into use in predicting radiation effects in electronics. The disadvantage in the Geant4 calculations is the relatively high threshold for deployment. On the other hand, the Geant4 is a powerful tool to investigate radiation effects in complex volumes. There is also a Geant4-based *Monte-Carlo Radiative Energy De-*

Table 3.1: Stopping force prediction tools.

Source	Type	Description
SRIM [53]	semi-empirical	The most well-known of them all. Based on the work of Ziegler *et al.* described in Ref. [92]. Over the years, numerous updates have been made in the calculations. Last major update was in 2003. This code and its user-interface are very versatile and user friendly. It enables calculations for a wide energy range with huge variety of ion-target combinations with a reasonable accuracy. Software is freely available at http://www.srim.org.
LET Calculator [93, 94]	semi-empirical	Another relatively widely used tool developed by Zajic and Thieberger in Brookhaven National Laboratory. Based on an earlier version of SRIM with parametrization to experimental data measured by the developers. Available online at http://tvdg10.phy.bnl.gov/let.html.
ECIF Cocktail Calculator [95]	semi-empirical	Based on parametrization of modified Bohr's classical stopping theory. This model will be presented in more detail in Section 5.1.3. Web-interface can be found at https://www.jyu.fi/accelerator/radef/ECIFCalc.
PASS [96]	theory	Based on the work by Sigmund and Schinner[97]. The calculations are fully based on fundamental physics without any parameterization to the experimental data. Stopping force values are available upon request from the model developers.
CaSP [98]	theory	Convolution approximation for Swift Particles developed by Grande and Schiwietz and described in Ref. [99, and references therein] . Available online at http://www.casp-program.org/.
Paul's database[54]	data table	Extensive tabulation of published experimental stopping force data maintained by Helmut Paul. Available online at http://www.exphys.jku.at/stopping/.
Hubert tables [100]	data table	Tabulation of experimental stopping force values in the energy range from 2.5 to 500 MeV/u. Not as comprehensive as Paul's database above.

position (MRED) tool developed in Vanderbilt University, USA, which is available online [22]. This tool enables estimations for the particle-induced energy deposition in complex geometries via user friendly interface. For this tool user registration is required, whereas the Geant4 is fully open-source.

All the above mentioned are *estimation tools* (except the data tables), and they provide *estimations* for the stopping force. Each of them have their *pros and cons*, and in cases where there is no experimental data to compare, it is in the user's judgement whether or not to rely on the values given by the predictor. Discussions have aroused among the radiation effects community about the differences in the estimated stopping force values between the tools especially for heavy ions like xenon[57]. The differences are illustrated in Fig. 3.9, where the ratio of values for electronic stopping force of silicon for different heavy ions, estimated by two different predictors: *LET Calculator* and *SRIM*. For lighter ions, such as nitrogen, the agreement is fairly good, as expected due to the existing experimental data for the code parametrization. However, for heavier ions the divergence increases, e.g. xenon ions exhibit a difference of 12 %. This is due to the extrapolation of the parameters based on experimental data in other ion-target combinations.

In May 2005 the *RADECS 2005 Thematic Workshop on European SEE Accelerators* was held in Jyväskylä, where these discrepancies in LET predictions were addressed. This meeting actually instigated the experimental part of the electronic stopping presented in this work. The results of these experiments are discussed further in Section 5.1.

3.2.5 Channeling

Typically in the considerations of electronic stopping, the electrons are considered uniformly distributed in the target. In reality, in many materials the atoms are aligned, forming crystal structures, which lead to anisotropic electron densities. This yields a non-uniform energy loss for an ion along its path. In most of the cases this is not an issue as the density variations average out along the ion trajectory. Nevertheless, in materials with well-defined crystal structures, such as silicon, the energy loss may depend substantially on the crystal orientation. This is a minute effect when considering isotropic radiation fields in space or on ground, but may lead to unexpected results e.g. in radiation effects testing or in stopping force experiments, where parallel ion beams are used. The effect of channeling on energy loss measurements (see Section 5.1.1) is demonstrated in Fig. 3.10, where spectra of Xe-ions at 9.3 MeV/u

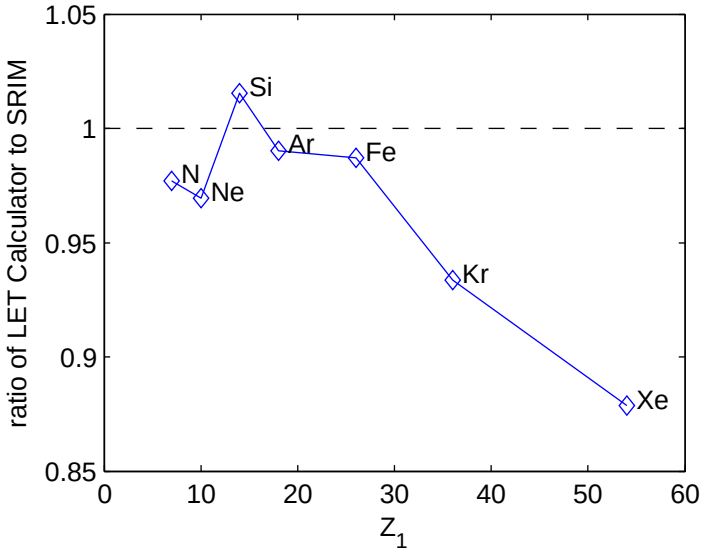

Figure 3.9: Ratio of estimated LET values from LET Calculator [93] to ones from SRIM[53].

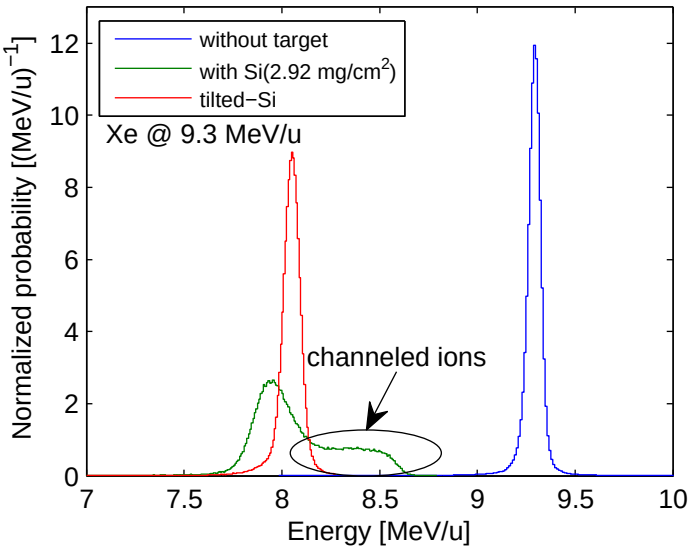

Figure 3.10: The effect of channeling in the measured energy spectra. The data are taken from [57].

are presented with and without silicon target placed before the energy detector. In these experiments the channeling effect was observed by accident. Apparently in the first setting the silicon target was placed just in the right position, i.e. the *channels*, formed in the crystal, being parallel with the beam. Whereas the primary beam exhibits a gaussian-shaped energy spectrum, the spectrum, measured after introducing the Si-target with "channels open", have a *tail* representing lower energy loss. This problem was solved by simply tilting the target by few degrees, thus making the silicon structure to appear more *amorphous*. After tilting, the energy spectrum became a gaussian-shaped, confirming the absence of channeling.

3.3 Recombination

In order to cause further damage in electronics, the electron–hole pairs induced by the radiation need to survive the *recombination*. Very comprehensive reviews for the recombination mechanisms are presented in Refs. [102, 103]. In this work the recombination is discussed only in a qualitative manner without detailed contemplation of different models (*geminate* and *columnar*), which are presented in the literature.

Typically the recombination is considered to be significant primarily in dielectrics, such as SiO_2, due to low mobility of the charge carriers, namely holes. Recombination of heavy-ion induced e–h pairs has been also observed in silicon (intrinsic or lightly doped) in Ref. [104], where the effect is demonstrated in *Solid State Detectors* (SSD). Generally the recombination is attributed to high e–h pair densities in the ion track, as discussed in Section 3.2.1. Contrary to this view, in Ref. [104], the recombination is shown *not* to depend on the e–h pair density, but on the atomic defects produced by the nuclear stopping mechanisms. Usually in the field of radiation effects testing of electronics, the recombination in silicon gets very little attention if not fully ignored, and main focus is in dielectrics. According to above mentioned aspects, the recombination can be considered to depend primarily on two things: (1) the external electric field, and (2) the target material (insulator and semiconductor). There is no such thing as an e–h pair in metals, as defined in Section 3.1, because of non-existing bandgap. Despite the results presented in Ref. [104], also the e–h pair density has to be taken into account, at least in dielectrics.

Due to the high density e–h pair plasma in the core of heavy-ion track, the prompt recombination is expected to be relatively high regardless of external electric fields. Obviously, in the absence of electric field the recombination rate is very high for all

radiation sources and in all materials. Increase in the external electric field reduces the recombination by moving the electrons and holes apart from each other more effectively. Still the influence of external field inside a dense e–h pair plasma is weak due to the *Debye shielding*[105], thus limiting the escape of the charge carriers from the core of the plasma. Resulting in high recombination rates. This is observed in the charge yield results for heavy ions, presented in Section 5.2.2. The charge yield in SiO_2 is observed to be nearly an order of magnitude lower for Fe-ions than for x-rays. In Section 5.2 the recombination of e–h pairs in SiO_2 is presented via experimental results from the measurements of heavy-ion induced charge yield in silicon dioxide.

3.4 Thermal effects

Although the energy lost by an ion is in the first stage primarily transferred to kinetic and potential energy of the target electrons, the end point of the deposited energy is not entirely there. External electric field can be used to remove the induced free charge carriers (namely the electrons) from their site of origin, thus removing also the deposited energy, as done e.g. in *Solid State Detectors*. Otherwise the e–h pairs, i.e. the energy, remain more or less stationary, and their movement is mainly governed by diffusion and space charge effects. At this point the recombination becomes more significant as discussed above.

In the recombination processes the e–h pairs are annihilated, but the energy does not disappear, it is just transformed e.g. into photons and phonons. Partially the energy of these secondary (or actually *tertiary*) quanta is turned into thermal energy of the target lattice. This is for instance the basic principle in the bolometer based particle detectors (see e.g. Ref. [106]), where the particle energies are determined by measuring the thermal changes in the detector due to ion impact.

Moreover, the complex transformation of energy, from the kinetic energy of an ion passing by into atomic vibrations in the target, may lead to material modification, such as amorphization or changes in density, along the the ions track. Very extensive reviews on the thermal effects of ion beams in materials are given in Ref. [107]. Experimental and theoretical results, e.g. in Refs. [108, 109], show that the sizes of the regions modified by the ion impact in SiO_2 are in the order of nanometers depending on the ion's velocity and the electronic stopping force. The thermal effects of heavy ions have been largely ignored in the field of radiation effects in electronics. Nevertheless, these effects will become more significant in electronic structures when

the characteristic feature sizes are approaching deeper into the nano-scale.

3.5 Non Ionizing Energy Loss (NIEL)

The part of the deposited energy by the ion in the target, which do not create e–h pairs, is referred to as the *Non Ionizing Energy Loss* (NIEL). The NIEL has been used in characterizing the effects of displacement damage in electronic devices, e.g dark current in solar cells, and the decrease in minority carrier lifetimes in bipolar devices. In many occasion nuclear stopping force (see the energy loss mechanisms in page 15) has been used interchangeably with the NIEL, but one must note the difference between these two.

Primarily the energy transfer from the projectile to the target recoils is a *non-ionizing* event, but these energetic recoils lose their energy by both electronic and nuclear stopping mechanisms. Hence the total NIEL is *less* than the nuclear stopping force. Only at high energies, where the nuclear reactions dominate the NIEL over the *coulomb scattering*, the total NIEL becomes higher than the nuclear stopping. This is illustrated in Fig. 3.11, where the NIEL of protons in silicon is presented. In the graph the contributions due to *coulombic scattering* and *nuclear reactions* in the total NIEL are specified. Also the energy losses due to the electronic and the nuclear stopping are plotted for reference. At proton energies above 10 MeV the total NIEL becomes higher than the nuclear stopping due to nuclear reactions (see Section 2.4). Methods to estimate the heavy-ion NIEL in silicon have been proposed in Refs. [110, 111]. The proton NIEL in silicon is presented e.g. in Ref [66]. As the main focus in this work is in the electronic stopping force for heavy ions and the recombination of generated e–h pairs, the NIEL concept is not discussed in detail. Also the energy range of the heavy ions considered in this work is at such level, where the nuclear stopping, and thus the NIEL, is much less than electronic stopping and the LET (cf. Fig. 3.11 and Eq. (2.31)).

3.6 Categories of radiation effects in electronics

All the above mentioned mechanisms of energy deposition for heavy ions produce myriad of different effects in electronics. These effects are typically divided into two main categories: *Cumulative* and *Single Event Effects* (SEE), which are briefly introduced next.

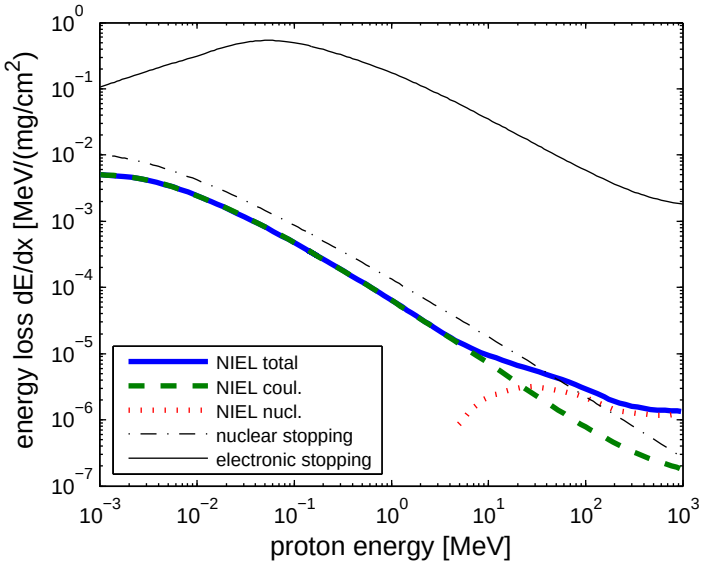

Figure 3.11: NIEL for protons in silicon with contributions due to the coulombic(dashed) and nuclear reactions(dotted) specified. For reference the energy loss due to the electronic and the nuclear stopping as calculated from SRIM[53] are also plotted. The data for the NIEL is taken from Ref [66].

3.6.1 Cumulative effects

Cumulative stress of radiation may cause gradual changes in the characteristic properties of electronics, such as *threshold voltage shifts* and *decrease in the minority carrier lifetimes*, etc. There is two subdivisions for the cumulative effects: *Total Ionizing Dose* (TID) and *Displacement Damage Dose* (DDD). They are related to the concepts of the LET and the NIEL, respectively.

The TID effects are governed by those radiation-induced charge carriers, which have survived the recombination and are not swept away by the electric fields. Because the electron mobilities, especially in dielectrics, are higher than those of holes, typically the trapped charges are the holes. Moreover, the effect is more pronounced in dielectrics than in semiconductors. Although, in case of interface trapped charge, it is located in the semiconductor side of a dielectric-semiconductor interface. The TID effects can occur in both *Metal-Oxide-Semiconductor* (MOS) devices and *bipolar devices*. In this work the TID and recombination effects of heavy ions are studied in MOS *Field Effect Transistors* (MOSFETs) (see Section 5.2). For more detailed information on TID effects the reader is referred to Refs. [103, 112].

The DDD effects in electronics are induced by the NIEL associated with particle radiation (see Section 3.5). The atoms may get knocked out from their lattice site due to an ion hit, creating a vacancy-interstitial pair, called a *Frenkel defect or pair* (FP). Typically the reduction in current gain of bipolar transistors or dark currents in CCDs are attributed to these defects. This work is mainly concentrating on the ionizing particle radiation and the effects of NIEL or DDD are not discussed further.

3.6.2 Single Event Effects

The *Single Event Effects* (SEE) are referred to as the prompt response of electronics to ionization event, induced by a single energetic charged particle. As discussed above, charged particles are capable to ionize matter, i.e. generating e–h pairs in semiconductors and dielectrics. The SEEs can be divided in two groups: non-desctructive *soft errors* and destructive *hard errors*. In the following sections these two groups are briefly introduced.

3.6.2.1 Soft errors

When ion induces a temporary disturbance in a electronic circuit, which can be fixed by e.g. reprogramming the device, the effect is considered as a *soft error*. The main types of soft errors and their definitions according to Refs. [113, 114] are listed below.

SEU *Single Event Upset*, is an event where a memory bit (or bits) is (are) flipped, from 0 to 1 or vice versa. Typically only one bit is affected at the time and the effect can also be called *Single Bit Upset* (SBU). In case of corruption of multiple bits, the event is referred to as *Multiple Bit Upset* (MBU), which can be a concern in highly scaled memories or with ion hits at high grazing angles. The basic principle of a SEU in a *SRAM* cell based on *Complementary Metal Oxide Semiconductor* (CMOS) technology is discussed below.

SET *Single Event Transient* is a progressive disturbance in *combinatorial logic systems* caused by a single ion hit. The ramifications of a SET are dependent on e.g. the operation frequency of the circuit. SET may turn into a SEU, if it gets latched. In case of analog devices (e.g. operational amplifiers, comparators, voltage regulators) the transient disturbance due to a ion hit is called *Analog Single Event Transient* (ASET). The faulty signal caused by an ASET can propagate in an integrated circuit and lead to significant anomalies, such as data corruption or system failure [115, and references therein].

SEFI *Single Event Functional Interrupt* results in a loss of device functionality. After occurence of SEFI the malfunction can be fixed without power cycling the device. SEFIs are typically associated with SEUs in a control bit or in register.

Because the SEU is the "*oldest*" SEE-type, being observed in the first studies [25], it is chosen here as an example. The *anatomy* of a SEU in a typical SRAM cell is illustrated next.

In typical SRAMs the individual memory cells are consisted of p- and n-type MOSFETs (so called CMOS technology). A common 6 transistor SRAM-cell is presented in Fig. 3.12(b). The information is stored in two cross-linked inverters, consisted of transistors $T_1 - T_4$. Transistors T_5 and T_6 are used as the access point for reading and writing cell. In this configuration T_1 and T_3 are NMOS, and T_2 and T_4 PMOS.

In a static situation the memory cell is either in state "1" or "0". Let's now assume our cell to be in state "1", which we[3] have defined to prevail while the transistors T_1 and T_4 are conducting (ON), and T_2 and T_3 non-conducting (OFF). Now the potential at points Q and $\overline{Q}$ equals V_{CC} and 0 (ground), respectively. Furthermore, let's assume there would be an ion hit, illustrated in Fig. 3.12(a), on (or close to) transistor T_3. If the ion hit introduces enough charge in the channel beneath the gate oxide to momentarily "switch" ON the T_3, the potential at point Q would respectively reduce momentarily close to zero. If T_3 is ON long enough so that consequential low voltage at the gate of T_1 turns it OFF, transistors T_2 and T_4 will follow and change also their state leading eventually to a *bit flip*, i.e. the *SEU*.

The mitigation of these above mentioned soft-errors has become more important, not only in *space electronics* but general commercial electronics also, due to the technological evolution [116]. The mitigation techniques can be applied either in circuit or software level. The reader is referred to Ref. [117] for detailed discussion on different mitigation methods for soft errors in modern microelectronics, as they are not discussed further in this work.

3.6.2.2 Hard errors

In some cases particle-induced "cloud" of e–h pairs may generate current peak in a device, which may initiate high currents, leading to a desctructive failure. These kind of irreversible hard errors are typically less probable to occur than the soft errors discussed above. Of course, their weight in radiation reliability of electronics is higher

[3]There is no standard way how the states of memory cells (*zeros* and *ones* are defined as a respect to the transistors $T_1 - T_4$.

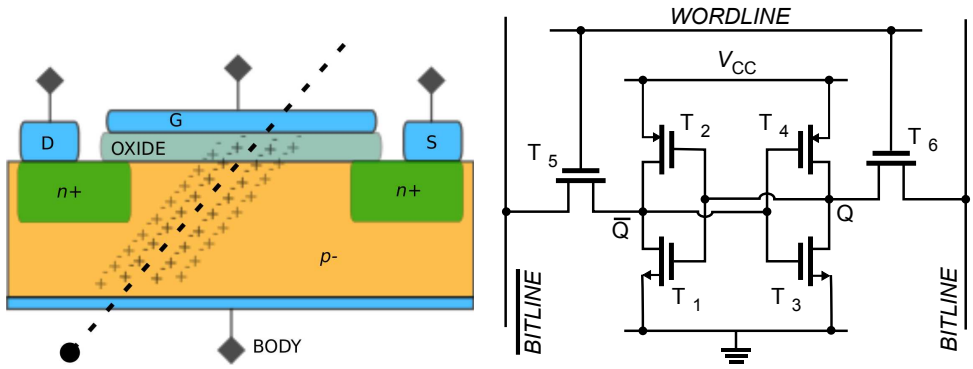

(a) Schematic view of a particle hit in a NMOS transistor.

(b) Basic 6 transistor CMOS memory cell.

Figure 3.12: A schematic view of an ion hit in a NMOS transistor (a) and a basic configuration of a 6-transistor SRAM cell (b).

because once they occur, the device is partially or totally out of service. The typical destructive SEE types are listed below with short descriptions after Refs. [113, 114, 118]:

SEL *Single Event Latchup* is potentially a destructive state in a device, where hit of a single ion creates conductive path between the device power supply and ground. The current through this path is stopped only by shutting down the power supply. The SEL may destroy the device if the current from the power supply is not limited and/or the power cycling is not performed fast enough after the current increase.

SEGR *Single Event Gate Rupture* is a breakdown of gate oxide in MOS devices, attributed to ion-induced conductive path. The excessive current through the dielectric leads to material meltdown via thermal runaway. The basic physical mechanisms underlying SEGR are yet unknown, mainly because the rapid nature of the event impedes accurate measurement of the current spikes. Only some qualitative or semi-empirical models exist for SEGR prediction.

SEB *Single Event Burnout* is a failure, which can be observed typically in power devices (MOSFET or bipolar). In SEB event there is a highly conductive path created in lightly doped epitaxial layer of the device, which leads to excessive current, and ultimately to thermal runaway with a permanent damage. In many cases SEB and SEGR occur simultaneously in power MOSFETs.

Mitigation of SEL and SEB is possible by limiting the supply current. The SEL is also possible to avoid with *Silicon On Insulator* (SOI) technology [119]. However, SEGR is found to be impossible to avoid once the threshold conditions (oxide electric field and energy deposition density) are exceeded [118]. This work is more concentrating on the basic mechanisms and do not consider the different SEEs in detail. Nevertheless, SEGR was observed in the charge yield measurements (see Section 5.2). However, these finding were unusable in this work due to the scarcity of obtained data.

4 Radiation Hardness Assurance Testing

As mentioned above in Chapter 1, there is various particle radiation sources present at ground level and in space. The radiation endurance (or hardness) of electronics operating in harsh radiation environments, such as nuclear power plants, accelerators or in space, needs to be assured either by manufacturing them *RadHard* or by testing them. In the earlier days, there were dedicated manufacturers for RadHard-components, which were competitive in performance with commercial products. When the *Cold War* ended and the rivalry over space supremacy cooled down, the production of RadHard electronics was no longer a prosperous business. Only a few manufacturers remained in the field, none of them exclusively on RadHard products. Because of high production costs, nowadays the RadHard industry is mainly focused on parts with high reliability requirements. In addition to lower prices, the performance of commercial electronics (COTS, *commercial-of-the-shelf*) is typically much higher than that of RadHard devices. Thus, COTS devices are often favoured in space projects due to superior performance and low cost, however, the drawback is their lack of being space qualified and unknown radiation performance.

As said, in order to ensure the radiation hardness of an electronic component, if not manufactured RadHard, it needs to be tested under radiation. There are some requirements (or "rules") for these *Radiation Hardness Assurance* (RHA) tests, agreed by the radiation effects community. Some of the commonly used specifications are presented in Refs. [113, 120–123]. These documents determine the framework, within which RHA tests typically need to be performed. As the aforementioned particle radiation environments are dominated by light particles (i.e. protons and electrons), the total dose issue is the first to be considered. Due to the focus of this work, which is on particle radiation and particularly on heavy ions, the total dose testing is not discussed further. Instead, an introductory on the basics for RHA testing in terms of SEEs is given.

The radiation environment is usually presented by its LET spectrum, which is considered to represent the ionizing efficacy. This can be done by first defining individual particle spectra (see Fig. 1.4) in terms of their LET and merging them together. The result is a single spectrum representing the given environment. As an example, four

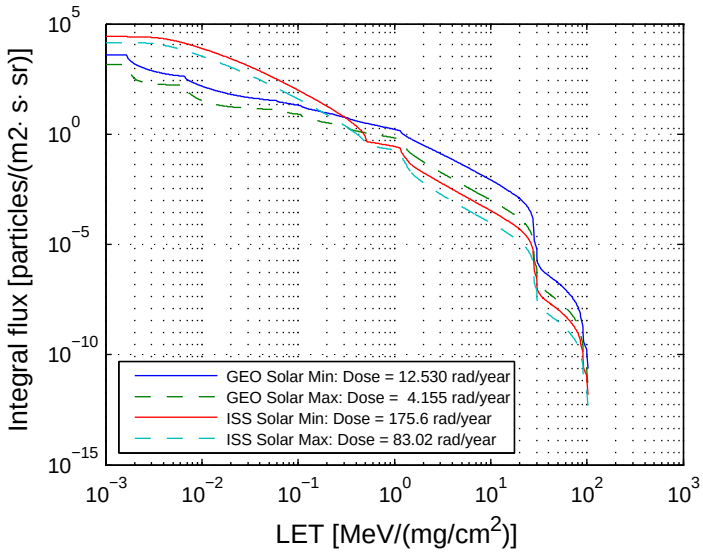

Figure 4.1: Integral flux of galactic cosmic ray particles during solar minimum (solid) and solar maximum (dashed) as a function of Linear Energy Transfer in GEO or near Earth interplanetary space (blue and green) and International Space Station orbit (red, cyan). Data taken from [22].

LET spectra are presented in Fig. 4.1, where radiation environments in two different regions are estimated during solar maximum and minimum (the data are taken from Refs. [21, 22]). Because of the presence of heavy ions (or high LETs) in these environments, not only the total dose effects are a concern, but the electronics need to be determined also for their susceptibility to SEE. In principle, SEEs can be produced by any source emitting particle radiation, if the particles are capable of intruding into the device and produce enough ionization. In addition, the used radiation needs to mimic the effects in the real operational environment.

In laboratory, radiation sources, such as Ra-226 (∼100% α-emitter, with some gamma radiation) and Cf-252 (α-emitter, with 3% of spontaneous fission, producing also neutrons) [124] etc., are convenient for this purpose because of their relatively low price and ease of use. The disadvantage in these sources is the restricted ion energies and species as well as the limited intensities. Furthermore, there may be more than one energy or particle type emitted from the source. Also, radiation type may be multifaceted, e.g. including also gamma or neutron radiation, which limits the use of these sources even more. Due to these limitations, the use of radioisotope sources is prohibited in the official RHA tests by the specifications[113, 120]. These sources are

typically used only for trial runs of the setup for the RHA testing. The specifications for RHA testing for SEEs require the use of particle accelerators.

The particle accelerators are multi-purpose tools, which in the past have been used mainly in basic nuclear physics studies. In recent years the accelerators have been increasingly harnessed also for applications, such as the RHA tests. Next, a short introduction is given on basic principle of SEU testing by use of heavy ions. In the following paragraphs there is also an introduction given on the Accelerator Laboratory in the University of Jyväskylä (JYFL) with its dedicated *Radiation Effects Facility*, RADEF.

As discussed in Section 3.6.2.1, SEUs are the most prominent error type in electronics. The SEU testing of e.g. memory device is done by irradiating the memory with certain ion (LET) and with fluences ranging from 10^6 to 10^7 cm^{-2} depending on the device sensitivity [113, 120]. Typically above the sensitivity threshold, more than 100 upsets are required to obtain adequate statistics. The required ion fluxes are from 100 to 10^5 cm^{-2}s^{-1}. In a typical test procedure after the ion exposure, the memory is read and the number of bit flips (SEUs), N_{err}, are determined. From this the SEU cross-section per bit can be calculated by using equation

$$\sigma_{SEU} = \frac{N_{err}}{n_{bit}\Phi}, \tag{4.1}$$

where n_{bit} is the number of bits in the tested memory and Φ is the ion fluence in cm^{-2}. By changing the LET by using different ions, the characteristic SEU sensitivity of a device can be obtained. See more discussion on the different ions used for the testing at RADEF in Section 4.1.3. Moreover the LET can be varied by tilting. This introduces a concept of *effective LET* which is defined as

$$\mathrm{LET}_{eff} = \frac{\mathrm{LET}}{\cos\theta} \tag{4.2}$$

where θ is the angle of incident for the impinging ion and LET is the electronic stopping of the ion. By definition $\theta = 0°$, when ion trajectory is perpendicular to the device surface. The applicability of the effective LET has also been questioned over the years, along with the concept of LET in general (see Section 3.2 and references given there). No further comments will be made on the suitability of the effective LET concept here. One should also note, that in tilted condition the ion fluence, Φ,

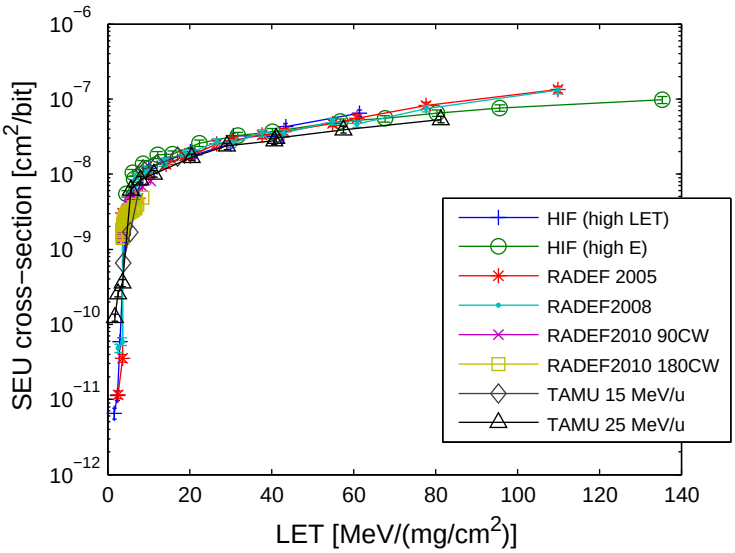

Figure 4.2: SEU cross section for 4 Mbit Atmel AT60142F SRAM used in the *SEU monitor* [73]. The data are partly taken from Refs. [72, 125] and is partly unpublished.

should be replaced with *effective fluence*

$$\Phi_{eff} = \Phi \cdot \cos\theta. \tag{4.3}$$

In Fig. 4.2 there is a SEU cross-section data for a SRAM plotted as a function of (effective) LET. This is a typical way to characterize the radiation susceptibility of electronics. In this graph there are data measured in three different facilities: the Heavy Ion Facility (HIF) in Louvain-la-Neuve, Belgium[126], the Radiation Effects Facility (RADEF) in the University of Jyväskylä (see Section 4.1.3) and the Radiation Effects Facility in the Texas A&M University, USA[127].

This kind of characteristic plot can be used for estimating the SEU rates in the operational environment. This can be done by using a dedicated software, e.g. *CREME-96* [22], by assigning the environment as depicted in Fig. 4.1 and entering the parameterized SEU cross-section curve. From these input data the code will give an estimation for the SEU rate in orbit. A very good demonstration of this procedure is given in Ref. [128], where one of the studied devices is the 4 Mbit Atmel AT60142F SRAM, discussed above. The agreement reported in this paper between estimated and observed SEU rates is fairly good.

4.1 RHA test facility at JYFL

As mentioned above, particle accelerators are required for the RHA testing of electronics. In the Accelerator Laboratory of the University of Jyväskylä (JYFL) there is a cyclotron type particle accelerator, which is being utilized in the RHA testing. The effective utilization requires a seamless cooperation between different groups in the laboratory: *ion source developers*, *accelerator operators* and the personnel in the *Radiation Effects Facility* (RADEF) itself. The reader is referred to Ref. [129], where a good review on the use of the JYFL cyclotron for the RADEF facility is presented. This reference is used as a basis for the following brief introductions on the key elements in the operation of the RHA test facility at JYFL.

4.1.1 K=130 Accelerator

The nominal *K-value* of the JYFL cyclotron is 130 [130, 131]. In cyclotron-type accelerators the beam energy is dependent on its K-value, the charge state (Q) and the mass (A) of the accelerated ion species by

$$\frac{E}{A} = K \cdot \left(\frac{Q}{A}\right)^2 \text{ [MeV/u]}, \tag{4.4}$$

where A is given in atomic mass units. E.g. for $^{131}Xe^{+35}$ ions, by substituting value $K = 130$ into Eq. (4.4), it gives ion energy of ∼9.3 MeV/u. The cyclotron enables production of so called *ion cocktails* (see Table 4.1). These cocktails are enabled by simultaneous acceleration of the used ions due to the sufficiently small differences in their *mass-to-charge ratio*, $\frac{A}{Q}$. Within the cocktail, the ion energies, in terms of MeV/u, are nearly the same for all the species. However, some difference is required in the $\frac{A}{Q}$-values in order to extract them separately. This is possible due to the very good mass resolution ($\sim 0.3‰$) of the JYFL cyclotron, which has been demonstrated in Ref. [132]. The final selection of ion species is done either by the fine-tuning of the *radiofrequency* (RF) or the magnetic field of the coils in the extraction part of the cycltron. Both of these methods enable a fast beam change without readjusting the whole accelerator. The details of acceleration techniques are outside the scope of this work and are not discussed further.

4.1.2 Electron Cyclotron Resonance Ion Sources

In order to produce the ion cocktails, the selection of ions with nearly the same $\frac{A}{Q}$-values have to be simultaneously injected into the cyclotron. At JYFL this is done by using its two *Electron Cyclotron Resonance Ion Sources* (ECRIS), which play a key role in the whole operation of the RADEF facility. The older ECRIS of the laboratory is operated with microwave frequency of 6.4 GHz [133] and the newer one with 14.1 GHz [134]. Both of the ECR ion sources enable the simultaneous production of high charge state ions.

Due to the assembly of the modern, high-density memories, the RHA testing is often done by irradiating the devices from the *backside* through the silicon substrate. This issue has been discussed in Ref. [135]. Typically in this approach the ions need to penetrate approximately 50 µm or more of silicon before they reach the sensitive volume. This requires high penetration depths, i.e. high energies, for the ions. Because of this, there has been an extensive development work done with the ECRIS at JYFL in order to increase the ion energies. This has been done by improving the ionization capability of the ion source. The detailed description of the upgrades is presented in Ref. [132]. Because of the Q^2-dependence in Eq. (4.4), the increase in the ion charge state is the most straightforward way to increase the energy. Thus no major modifications are needed in the cyclotron itself. With the upgrade of the JYFL ECRIS the energy of the heaviest ion in the RADEF cocktail, which is Xe, was increased from 475 MeV to 1217 MeV. This corresponds to an increase in the penetration depth from 44 µm up to 89 µm, which is considered to be sufficient for the RHA tests.

4.1.3 The RADiation Effect Facility, RADEF

The *RADiation Effects Facility* (RADEF) located in the Accelerator Laboratory of the University of Jyväskylä has been utilized in RHA testing since 1998. The RADEF has been operated under the contract with the European Space Agency (ESA) since 2004 and was accredited in 2005 as one of the ESA's *European Component Irradiation Facilities* (ECIF). The other external irradiation facilities belonging to the ECIF consortium are the *Proton Irradiation Facility* (PIF) at the Paul Scherrer Institute, Switzerland [136] and the Heavy Ion Facility (HIF) at the Université catholique de Louvain (UCL), Belgium [126]. Also part of ECIF is ESA's own internal Co-60 irradiation facility for TID studies, which is located at the *European Space Research and Technology Centre* (ESTEC) in Noordwijk, the Nethelands. The ESTEC facility

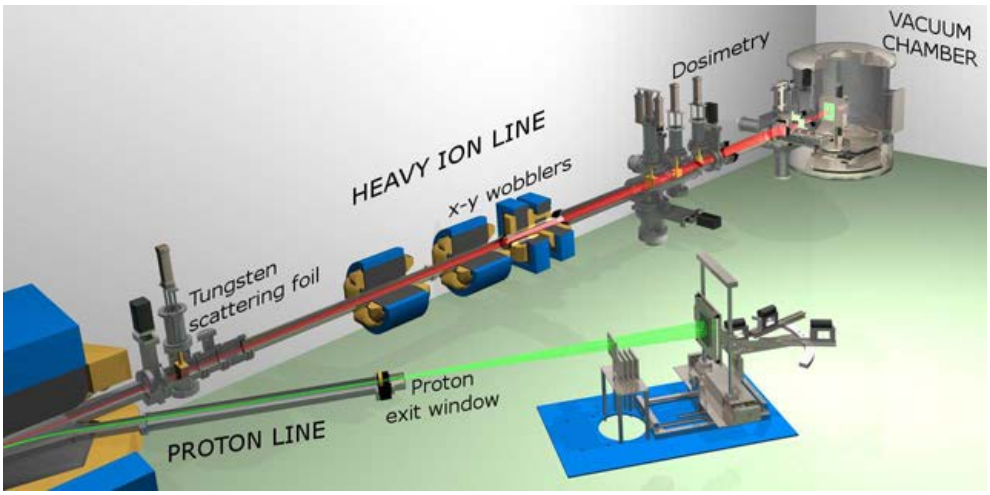

Figure 4.3: An artistic illustration for the overview of the RADEF facility. Image courtesy of Dr. Heikki Kettunen.

is also equipped with a *Californium-252 Assessment of Single-event Effects* (CASE) for preliminary heavy-ion testing of devices. The CASE equipment is not approved for official RHA testing as discussed above.

The RADEF consists of two separated beam lines, one for heavy ions and another for protons. An overview of the facility is illustrated in Fig. 4.3, where both of the beam lines are marked. The proton beam is taken in air through a 200 µm thick tungsten window. The proton dosimetry consists of an ionization chamber at the beam exit, and particle detectors behind the target stage. The ionization chamber enables accurate and real time monitoring of the beam intensity and the particle detectors are used for the initial beam calibration.

In the heavy-ion line the beam homogeneity is obtained by using: (1) a 1 µm thick scattering foil, made of tungsten, upstream in the beamline, and (2) x–y wobblers. With these equipment beam homogeneity of better than the required ±10% can be achieved over an area of 4×4 cm^2, or even larger if needed. Typically an area of 2×2 cm^2 is used. The heavy-ion dosimetry is made of four *photomultiplier tubes* (PMT) equipped with scintillator crystals. The illustration of the heavy-ion dosimetry is presented in Fig. 4.4. The PMT detector assemblies are used in the online monitoring of the beam during the experiment runs. The detectors are located on the edge of the collimator plates. The detectors provide also energy spectra, thus the beam purity can be assured.

Table 4.1: High penetration heavy-ion cocktail available in the RADEF.

Ion	Energy[a]	LET[b] @ surface	LET[b] @ Bragg peak	$\text{Range}_{\text{SRIM}}$[c]
$^{15}N^{+4}$	139	1.87	5.92 (@191 µm)	202
$^{20}Ne^{+6}$	186	3.68	9.41 (@138 µm)	146
$^{30}Si^{+8}$	278	6.74	13.7 (@114 µm)	130
$^{40}Ar^{+12}$	372	10.1	18.9 (@100 µm)	118
$^{56}Fe^{+15}$	523	18.8	29.7 (@75 µm)	97
$^{82}Kr^{+22}$	768	30.4	41.7 (@68 µm)	94
$^{131}Xe^{+35}$	1217	55.0	67.9 (@57 µm)	89

[a] in units of MeV
[b] in units of MeV/(mg/cm^2)
[c] in units of µm

The heavy-ion irradiations can be performed either in *vacuum* or in *air*. The devices under test (DUT) are attached in a standard fixture plate which is affixed to a *linear movement apparatus* (LMA). The LMA can be moved in x–y–z direction and also tilted with respect to the beam. When the irradiations are performed in air, the upper part of vacuum chamber is lifted up and a 25 µm thick Kapton foil is used as a beam exit window. Although, the ion energy is slightly reduced in the window and in air, this is an efficient way of testing devices, where the sensitive volume is near the surface. The feasibility of irradiating devices in air at RADEF is demonstrated in Ref. [72].

There are two different ion cocktails available in the RADEF with energies of 3.6 MeV/u and 9.3 MeV/u. Recently the former is no longer routinely used, as the cocktail with higher energy (i.e. higher penetration) has been favoured by the users performing the RHA tests. The ions in the high energy cocktail, and their charactistic information, including the energy, LET and projected range, are listed in Table 4.1. In the table the LET values are estimated from the experimental values discussed in Section 5.1.2 and the ranges are taken from the SRIM-code.

It is the combination of the JYFL's ECR ion sources and cyclotron, which makes the RADEF and its heavy-ion cocktail very attractive for the RHA testing. The high penetration depth, even for the heaviest ions, and the fast change of ion species within the cocktail enable very efficient testing. Since its inauguration in 2005 RADEF has served 35 different users in more than 130 separate irradiation campaigns. During last three years an average of 28 campaigns a year has been performed.

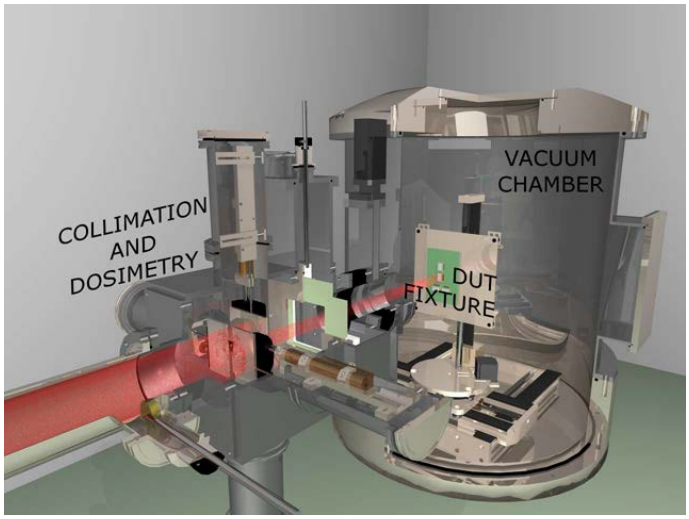

Figure 4.4: Close-up of the heavy-ion dosimetry, and the vacuum chamber with the DUT fixture and linear movement apparatus. The red haze represents the beam. Image courtesy of Dr. Heikki Kettunen.

5 Experimental work

The experimental part of this work consists of: (1) energy loss measurements of heavy ions in silicon, and (2) heavy-ion induced charge yield in silicon dioxide. The results for (1) and (2) are published in Refs. [56, 57, 137] and in Ref. [138], respectively. The experimental methods and the obtained results are discussed in this chapter.

5.1 Electronic energy loss

Typically experimental energy loss of an ion in certain material can be determined by measuring the ion energy before and after the target. With the target thickness the mean energy loss per unit length (dE/dx) is obtained. This is called a *transmission method*. Typically, these transmission experiments are based on *solid state detectors* (SSD), or combinations of SSD and *Time-Of-Flight telescopes* (TOF)[139, 140]. The disadvantage in using SSDs in the stopping experiments for heavy ions, is the *Pulse Height Defect* (PHD)[141], which requires corrections in the stopping data at low energies. The PHD in SSDs refers to a phenomenon, where the signal from the detector is not linearly proportional to the actual deposited energy by the ion. This is due to the energy losses in inactive regions of the detector, the contribution of the nuclear stopping, and the recombination of the electron–hole pairs (cf. Section 3.3). The energy lost in nuclear stopping (i.e. to the target recoils) contributes only partially in the generation of electron hole pairs in the active region of the detector.

With TOF-telescopes the ion energy is determined from its mass and its velocity, which is derived from the time that ion takes to travel between two *timing-gates*. In the timing-gate the secondary electrons induced by the ion passing through thin carbon-foils are collected by using high electric fields (kV) to a *micro-channel-plate* (MCP), which locates at the bottom of the gate. A photograph from one of the timing-gates used in this work is presented in Fig. 5.1. In TOF-telescopes the non-linearity in energy-response is weaker than in SSDs, as only the foils in the timing-gates contribute in the energy loss, which needs to be taken into account at low energies. Typically, relatively thin carbon foils are used ($\sim$ 20 µg/cm^2 in this work) in order to minimize the effect. On the other hand, in thicker foils more secondary electrons are produced and stronger signal in the MCP is observed. Thus a compromise is needed in the selection of the foil thickness. In case of the heavy ions the number of secondary

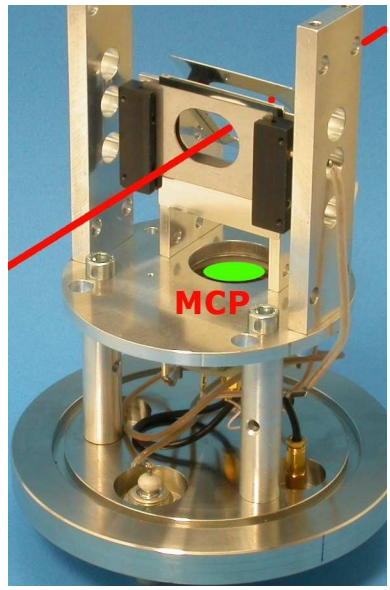

Figure 5.1: Photograph of a single timing-gate used in this work. The red line represents the beam and the micro-channel-plate is illustrated with the green ellipsoid.

electrons and thus the efficiency of the timing-gate-detectors is higher compared to lighter ions, thus thinner foils can be used.

In transmission measurements the detectors, in downstream after the target on the beam axis, are placed in such a way that they cover only a small solid angle. This ensures the detection of ions that have experienced small angle scattering, mainly due to collisions with target electrons, during their passage though the target. Thus in the measured energy loss only the contribution from the *electronic stopping* can be considered. Still in these systems, with low energy ions the contribution of nuclear stopping increases with decreasing energy. This is due to the fact that the ions have also experienced multiple small angle scattering events with target nuclei[45]. In this work the used energy range is considered to be high enough in order to neglect the contribution of nuclear stopping in the measured energy loss.

5.1.1 B–TOF Method

In this work a new method was developed for the electronic stopping force measurements [57]. The B–TOF, or *magnetic–time-of-flight*, method utilizes the *Lorentz force* acting on a point charge moving in a magnetic field. In Fig. 5.2 the schematic overview

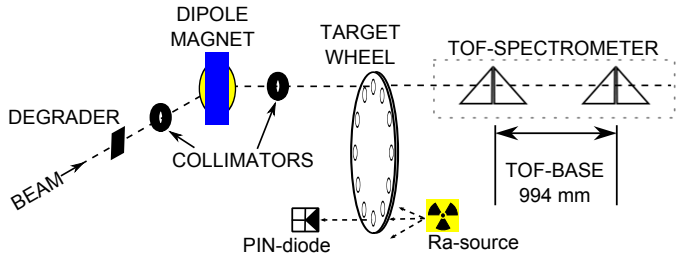

Figure 5.2: Set-up for measuring the LET by using B–TOF method (after [56, 142]). The key elements are the degrader, the dipole magnet, the motorized target wheel and the high-resolution TOF spectrometer. The thicknesses of different targets were measured by using a spectroscopic quality Ra-226 α-source.

of the B–TOF setup is presented. The primary beam (9.3 MeV/u in this work, see Table. 4.1) was steered to the target stage through a 30-degree bending magnet. The different targets were fixed in a rotating wheel in order to enable measurement of multiple targets in a single run. Also in the wheel there was one empty position for measuring the energies without a target. After the target stage the beam energy was measured with a TOF-telescope consisting of two timing-gates. Also there was an additional SSD located in the end of the beam line in order to check the beam quality if needed.

Although, there were several different target materials studied during the same experiments, in this work only the data for silicon targets are considered. Two Si-targets were used with thicknesses of 2.92 ± 0.03 mg/cm^2 and 0.300 ± 0.003 mg/cm^2, in order to cover wide range of energies. The thicknesses of the targets were determined by comparing the measured energy loss of the α-particles with stopping force values calculated with SRIM-code[53]. This method was considered to be accurate enough due to the high amount of existing experimental data for α-particles in silicon, which agrees with SRIM. For the thickness determination, a spectroscopic quality ^{226}Ra α-source was used as illustrated in Fig. 5.2. Nevertheless, the determination of the foil thicknesses was considered to be the major source of uncertainty in the results.

When measuring beam energies below the maximum energy, the beam was degraded before the bending dipole magnet. The distribution of beam energy and also charge state (see Section 2.2.5) are altered in the degrader. As mentioned, the method is based on the Lorentz force which is described by

$$\vec{F}_L = q(\vec{E} + \vec{v} \times \vec{B}), \tag{5.1}$$

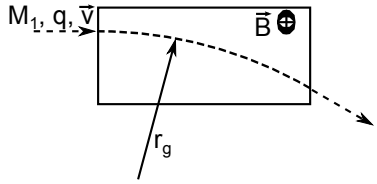

Figure 5.3: Moving point charge, q, with mass of M_1 in a magnetic field of B. Inside the box the direction of magnetic field is into the plane.

where $\vec{E}$ is the electric field and $\vec{B}$ the magnetic field acting on a particle with charge q and velocity v. In this work only the magnetic field perpendicular to the ion beam was used in guiding the ions, thus Eq. (5.1) reduces to $|\vec{F_L}| = qvB$. The magnetic field enforces the ion in a circular motion, as illustrated in Fig. 5.3, and the Lorenz force can be considered to equal the centrifugal force,

$$|\vec{F_L}| = qvB = M_1 \frac{v^2}{r_g}, \tag{5.2}$$

where M_1 is the ion mass, v is the ion velocity and r_g is the *gyroradius*, or *Larmor radius*, which is considered constant. The magnetic rigidity is defined as

$$\chi = B\ r_g = \frac{p}{q}, \tag{5.3}$$

where $p = M_1 v$ is the kinetic momentum of the ion. As the charge states of ions can occur only in integer numbers, at constant magnetic field only ions with the same magnetic rigidity are selected. Thus the bending magnet can be used as a energy selector. Furthermore, in this work beams consisting only one ion species at a time were used, thus eliminating residuals in the energy spectra. Some additional collimation was used in the measurements (see Fig. 5.2) before and after the bending magnet to improve the energy resolution.

As an example, let's assume the primary ion beam to be ^{56}Fe with energy of 9.3 MeV/u and charge state of +15 (i.e. 15 electrons stripped from the atom). When using a pure beam with only the ^{56}Fe-ions at well defined energy and with only single charge state, and without any scatterers in the beam's path, the measured energy spectrum is consisted of a sharp Gaussian peak (cf. Fig. 3.10 for xenon ions). The magnetic field, at which the primary beam is guided through the bending magnet, to the target stage and the detectors, is denoted as B_1. By introducing the degrader before the bending magnet the mean beam energy is decreased and the width of

the distribution broadened depending on the relative thickness of the degrader. In this work there were several different types of degraders used, mostly aluminium foils with different thicknesses and a grid made of tungsten wires (ø20 µm). One of these degrader assemblies was used at a time depending on the desired energy. The charge state of an ion moving through matter is dependent on the ion velocity, which can be estimated coarsely by using Eq. (2.26). Thus the scattered beam may contain several charge states, depending on the width of the energy distribution. In order to guide the beam to the target stage, the magnetic field need to be decreased according to relation

$$\frac{B_d}{B_1} = \frac{\chi_d}{\chi_1}, \tag{5.4}$$

where subscripts d and 1 denote for the degraded and the primary beam, respectively. Example spectra are presented in Fig. 5.4 with measured energies from the degraded ^{56}Fe-beam with and without the Si-target. The distinct peaks representing different charge states in the spectrum obtained without a target are indicated. After introducing a target the peaks shift toward lower energies (i.e. higher in time-of-flight). The charge states in the peaks of this spectrum no longer correspond to the ones in the original spectrum. Nonetheless, from this shift the energy loss in the target, and thus the stopping force can be obtained.

In this method the absolute magnetic field values are irrelevant here because only magnetic fields relative to B_1 are needed. The information was used mainly for planning the experiments. The charge-state effect in the measured stopping forces was considered negligible, due to the relatively thick targets used. The ions can be considered to reach their equilibrium charge state within the first few tens of nanometers after entering the target [143, 144].

5.1.2 Experimental electronic stopping force of silicon for heavy ions

The B–TOF method described above was utilized in measuring the electronic stopping force of silicon for ions included in the RADEF's high penetration cocktail (see Table. 4.1). The data has been published in Refs. [56, 57] and are presented in Figs. 5.5–5.11, with estimations from SRIM[53], LET Calculator[93] and PASS-code[96, 97]. Also estimations from Eq. (2.20) with parameter κ fitted to the silicon data are presented. The graph includes also all the experimental data for these ions available in Ref. [54], which can be considered to be the widest stopping force database. Accord-

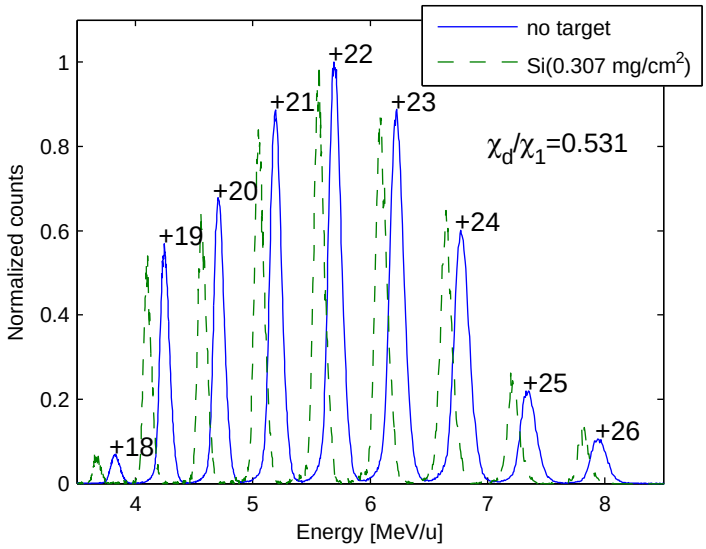

Figure 5.4: An example energy spectra before and after silicon target where the 9.3 MeV/u Fe-beam was degraded before the bending magnet and the ratio of the magnetic moments is $\chi_d/\chi_1 = 0.531$. Data taken from [56].

ing to this database, the experimental stopping data collected in this work for Ne-, Ar-, Fe-, Kr-, and Xe-ions in silicon were the first ones in these energy ranges.

Although the model, introduced in Section 2.2.3, is supposed to work by using Eq. (2.21) to scale the logarithm in Eq. (2.20), for silicon target better agreement with the experimental data was obtained by reassigning the κ via data fit. The obtained κ-parameters are given in Table 5.1, with the parameters calculated with Eq. (2.21) for comparison. As noticed, only small modification is needed in the parameters.

Readily from Figs. 5.5–5.11 one can see that all the represented estimation tools

Table 5.1: κ-parameters for the electronic stopping of different ions in silicon as extracted from the data fit and from Eq. (2.21)

ion	κ (fitted)	κ (Eq. (2.21))
N	1.0394	1.0804
Ne	1.0821	1.1160
Si	1.1209	1.1555
Ar	1.1490	1.1740
Fe	1.1890	1.2074
Kr	1.2232	1.1729
Xe	1.2646	1.1854

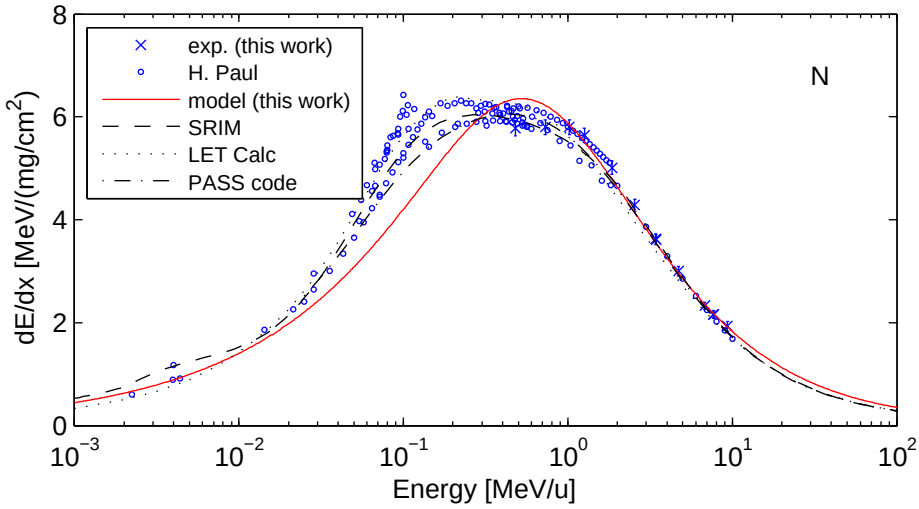

Figure 5.5: The experimental stopping force data for nitrogen in silicon from this work(dots) and from Ref. [54](circles) with comparison to estimates from Eq. (2.20) with fitted κ-parameters given in Table 5.1 (solid red), SRIM[53](dashed), LET Calculator[93](dotted) and PASS-code[96, 97](dash-dot).

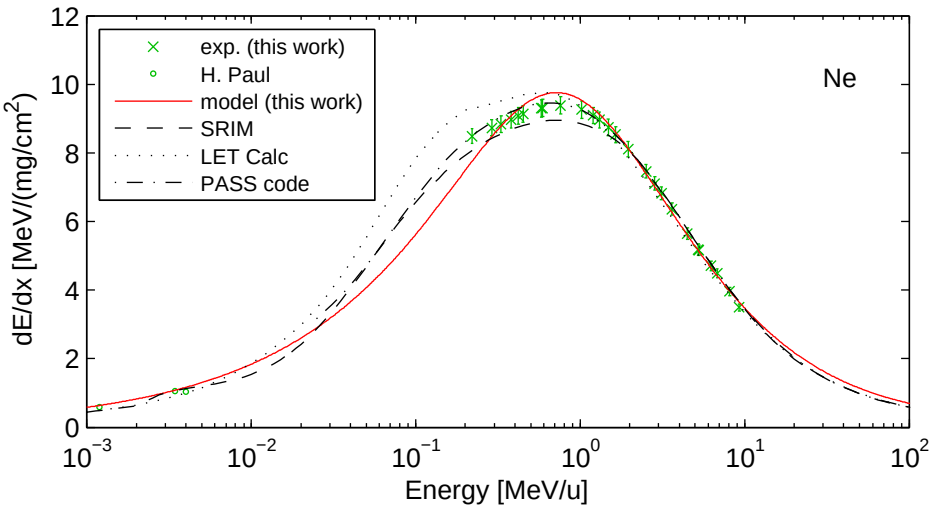

Figure 5.6: The experimental stopping force data for neon in silicon from this work(dots) and from Ref. [54](circles) with comparison to estimates from Eq. (2.20) with fitted κ-parameters given in Table 5.1 (solid red), SRIM[53](dashed), LET Calculator[93](dotted) and PASS-code[96, 97](dash-dot).

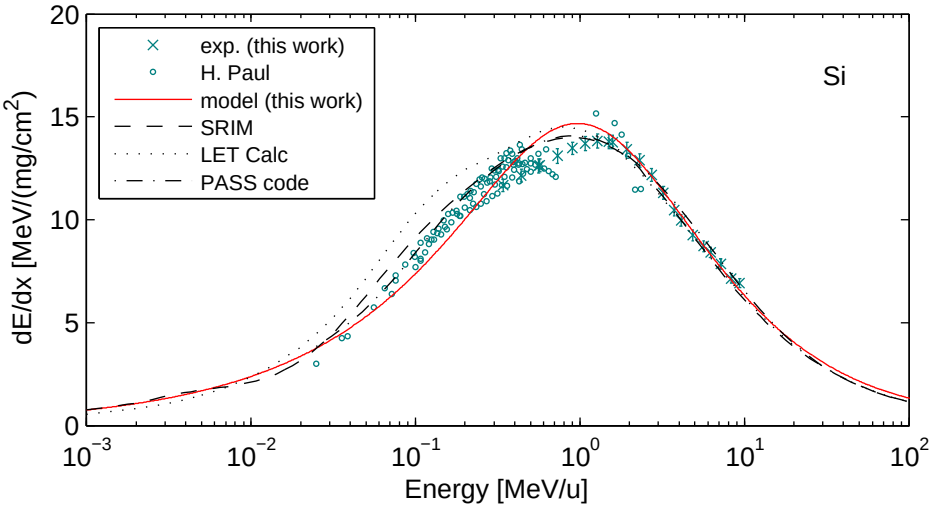

Figure 5.7: The experimental stopping force data for silicon in silicon from this work(dots) and from Ref. [54](circles) with comparison to estimates from Eq. (2.20) with fitted κ-parameters given in Table 5.1 (solid red), SRIM[53](dashed), LET Calculator[93](dotted) and PASS-code[96, 97](dash-dot).

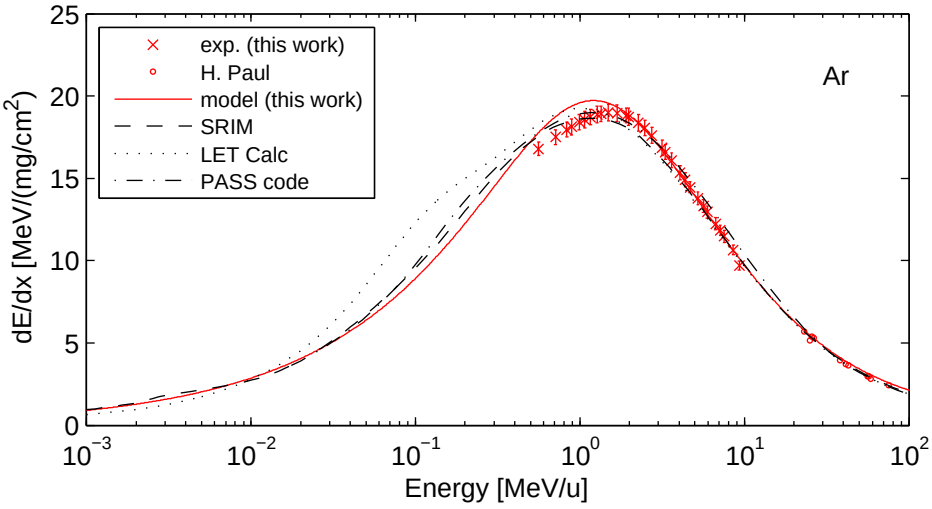

Figure 5.8: The experimental stopping force data for argon in silicon from this work(dots) and from Ref. [54](circles) with comparison to estimates from Eq. (2.20) with fitted κ-parameters given in Table 5.1 (solid red), SRIM[53](dashed), LET Calculator[93](dotted) and PASS-code[96, 97](dash-dot).

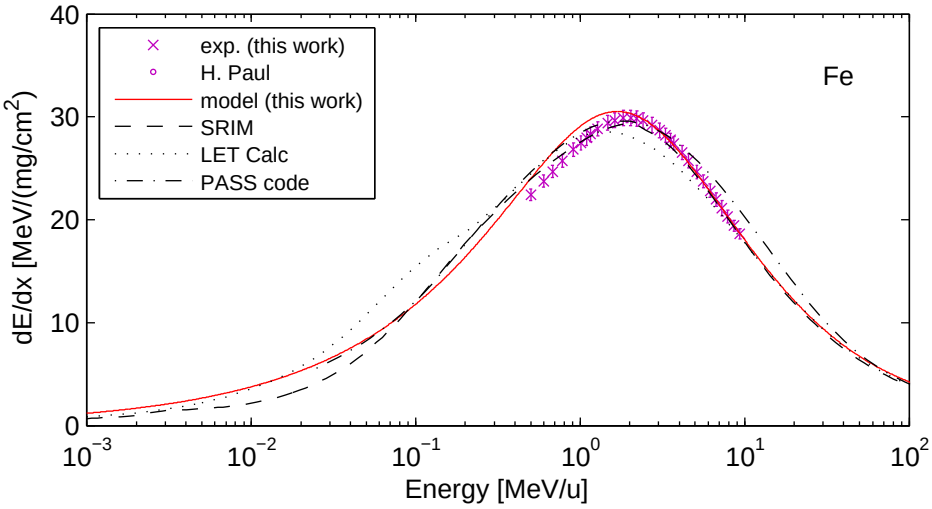

Figure 5.9: The experimental stopping force data for iron in silicon from this work(dots) and from Ref. [54](circles) with comparison to estimates from Eq. (2.20) with fitted κ-parameters given in Table 5.1 (solid red), SRIM[53](dashed), LET Calculator[93](dotted) and PASS-code[96, 97](dash-dot).

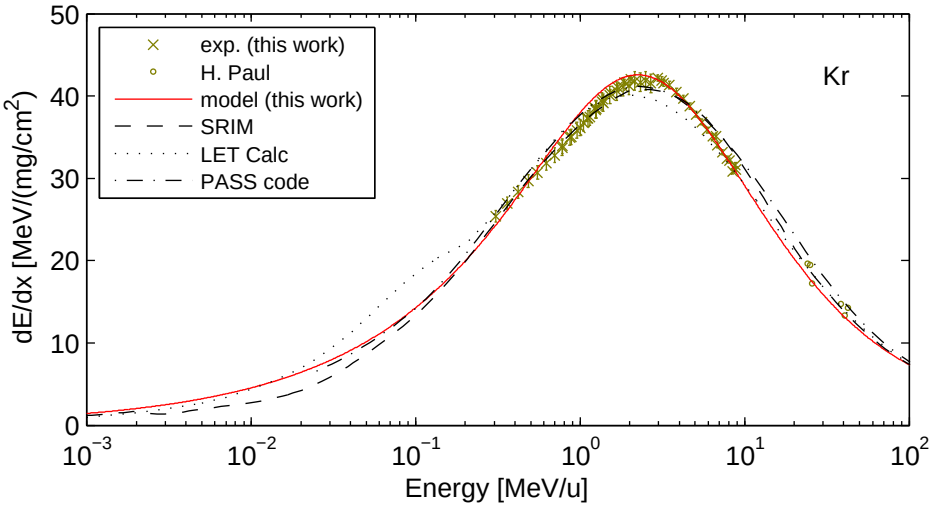

Figure 5.10: The experimental stopping force data for krypton in silicon from this work(dots) and from Ref. [54](circles) with comparison to estimates from Eq. (2.20) with fitted κ-parameters given in Table 5.1 (solid red), SRIM[53](dashed), LET Calculator[93](dotted) and PASS-code[96, 97](dash-dot).

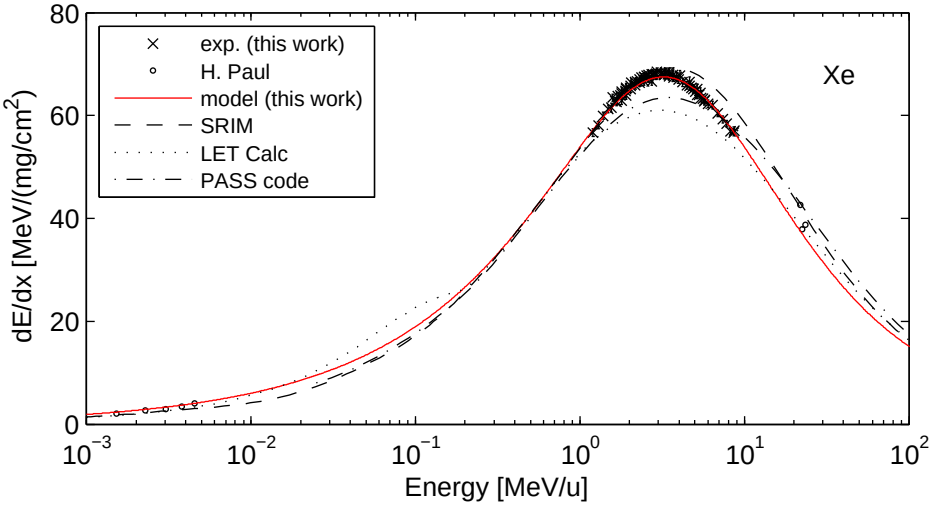

Figure 5.11: The experimental stopping force data for xenon in silicon from this work(dots) and from Ref. [54](circles) with comparison to estimates from Eq. (2.20) with fitted κ-parameters given in Table 5.1 (solid red), SRIM[53](dashed), LET Calculator[93](dotted) and PASS-code[96, 97](dash-dot).

give reasonable agreement with the experimental data. This is confirmed in Fig. 5.12, where the relative differences between the experimental data and all four estimation tools are presented. Here it can be seen that by using fitted κ-parameters, the model described by Eq. (2.20) gives very good agreement with the data in the energy range from 2 to 10 MeV/u. Especially good agreements over this energy range are observed with xenon-data, where the other estimation tools are exhibiting differences even up to 10% or more. These data verify the problem exhibited with the estimated electronic stopping force values for heavy ions. The heavier the ion, the higher is the discrepancy. The aim of this part of the work is to deliver data to the database, which is used for improving the description in the stopping force estimation tools.

5.1.3 Semi-empirical modeling of stopping

Eventhough, there are several tools available for estimating stopping force (see discussion in Section 3.2.4), they all have their restrictions. As discussed above the heavy-ion stopping data, used for the model parameterization of electronic stopping in silicon, is in many cases very scarce or non-existing. Also the graphs presented in the previous section show the divergence of different estimation tools from the

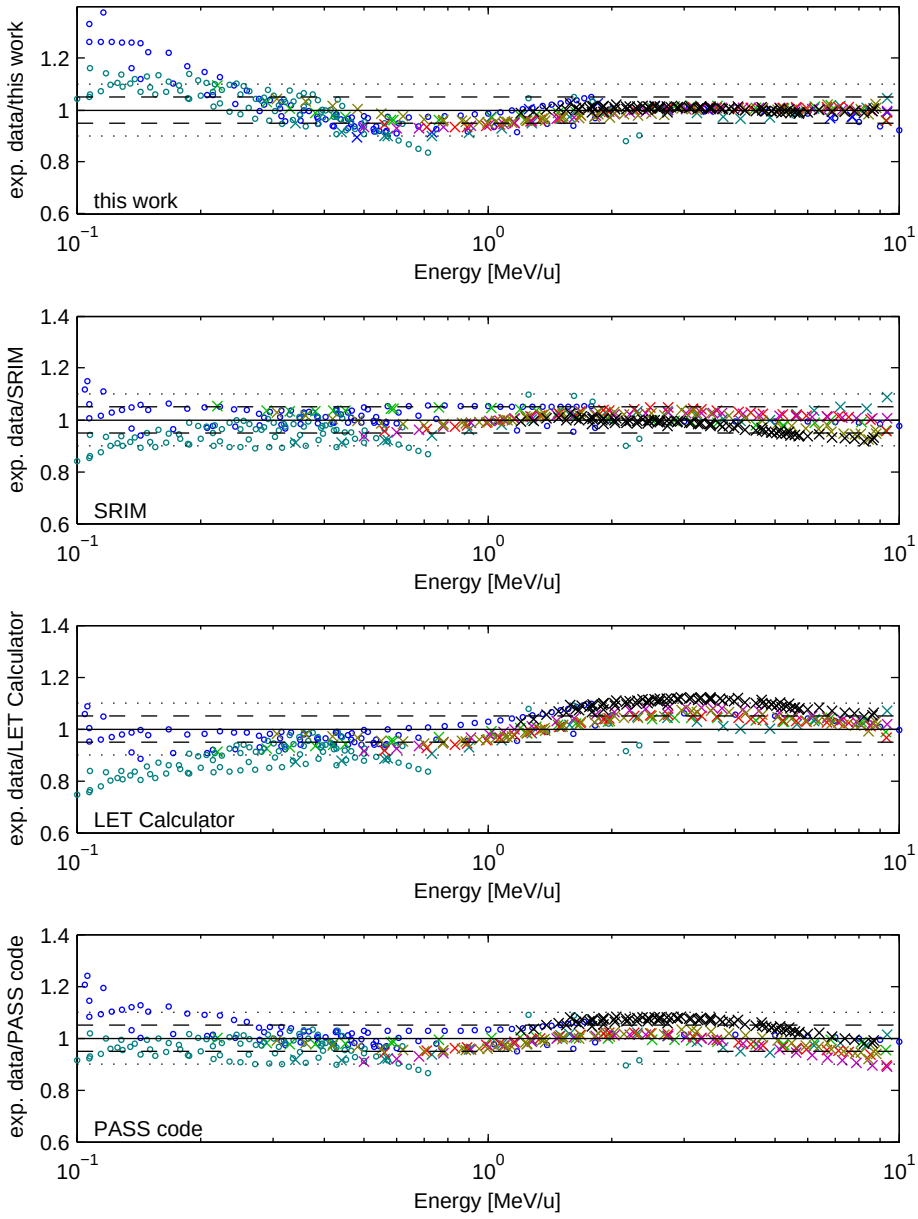

Figure 5.12: Relative difference between all experimental stopping force data in silicon and values estimated with Eq. (2.20) with κ-parameters given in Table 5.1(top), SRIM-code, LET Calculator and PASS-code (bottom). The color and marker designation is the same as in the previous stopping force graphs. The dashed and dotted lines represent ± 5 % and ± 10% limits, respectively

exprimental data. It may take a while before these new data are included in the descriptions of the existing codes, and thus a new prediction tool was established. This tool is called *ECIF Cocktail Calculator*[1][95]. The first version of this tool was introduced in Ref. [137]. The disadvantage in this initial approach is that it is limited only to silicon as a target and the seven ions given in Table 4.1. The validity of the expressions and parameters given in that work are also limited in energy to only where experimental data exist.

As it is observed from Figs. 5.5–5.11, by using the model introduced in Section. 2.2.3, the experimental data can be expressed with a reasonable agreement, requiring very limited parametrization. The validity of obtained expression can be considered to cover a wider range in energy. This new model will be implemented in the future version of the ECIF Cocktail Calculator, also covering targets other than silicon.

5.2 Heavy-ion induced charge yield in silicon dioxide

The TID effects in dielectrics especially in *MOS oxides* has been studied extensively for radiation types such as electrons, light ions (protons and α-particles), gamma rays and x-rays [103, and references therein]. For ions heavier than helium the experimental work has been very limited. Despite the high recombination rate, also heavy ions can cause cumulation of excess charge in the devices, which can lead to malfunction. Thus in order to estimate the remaining ionizing dose from heavy-ion irradiation, information on the charge yield in dielectrics is needed. The charge yield is referred to as the fraction of the induced charge which escapes from the prompt recombination.

In general the heavy-ion TID effects are not a big concern in space considering the low fluxes of heavy ions (see Section 1.1), but in the SEE hardness assurance testing the tested devices may receive high levels of heavy-ion exposure. This cumulated dose can affect the characterization results for device's SEE sensitivity. These aspects are discussed e.g in Refs. [145, 146]. In addition to the gradual cumulation of dose, also *microdose effects* in advanced electronics, attributed to heavy ions, have been reported e.g in Refs. [147–149, and references therein]. The microdose effects are referred to as highly localized TID effects caused by a single ion strike, like an aftermath of the SEE. The deposited microdose can alter the device functionality already at low ion fluences. This is considered to be a concern in small transistors[103].

[1]European Component Irradiation Facilities, the consortium of European Space Agency's irradiation facilities

Table 5.2: The tested devices in the charge yield measurements.

Device type	Process lot	gate dimensions W×L [µm^2]	oxide thickness [nm]
TA-629	G1928A	16×3	64.8
TA-629	G1928A	16×4	64.8
TA-629	G1928A	100×10	64.8
RADFET	P-3418	300×50	400
RADFET	P-3418	690×15	400

The second experimental part of this work was focussing on the yield of heavy-ion induced charge in SiO_2. The recombination and the resulting charge yields were determined by measuring the heavy-ion and the x-ray induced parametric changes in MOSFETs. The first results from these experiments have been published in Ref. [138]. The experimental methods, including the devices under test and the results, are discussed next. The results reported here include some previously unpublished data.

5.2.1 Experimental methods and devices under test

For the charge yield measurements different types of MOSFET devices were used as test vehicles. One device type was, referred to as *TA-629*, manufactured by Sandia National Laboratories[2] in Albuquerque, New Mexico, USA. Another device was, so called *RADFET* (RADiation sensitive Field Effect Transistor), manufactured by Tyndall Institute, Ireland. Micrographs of both device types are presented in Figs. 5.13 and 5.14. The device geometries including the widths and the lengths of the gate as well as the oxide thicknesses in the tested devices are listed in Table 5.2.

Both *n-* and *p-type* MOSFETs were among the Sandia's TA-629 devices, whereas RADFETs were solely p-type. The channel doping concentrations in the Sandia's TA-629 devices were $N_A = 4 \cdot 10^{16}$ cm^{-3} and $N_D = 2 \cdot 10^{15}$ cm^{-3} for the n- and p-type, respectively. In the RADFETs doping concentration was $N_D = 2 \cdot 10^{15}$ cm^{-3}.

The devices were irradiated with heavy ions and x-rays. The x-rays were used as reference due to the vast amount of data available for the charge yield of x-rays in SiO_2.

The x-ray studies took place at Sandia National Laboratories by using *ARACOR Model 4100 Semiconductor Irradiator* with 10 keV x-rays. The heavy-ion irradiations

[2]Sandia is a multiprogram laboratory operated by Sandia Corporation, a Lockheed Martin Company, for the U.S. Department of Energy's National Nuclear Security Administration under Contract DE–AC04–94AL85000

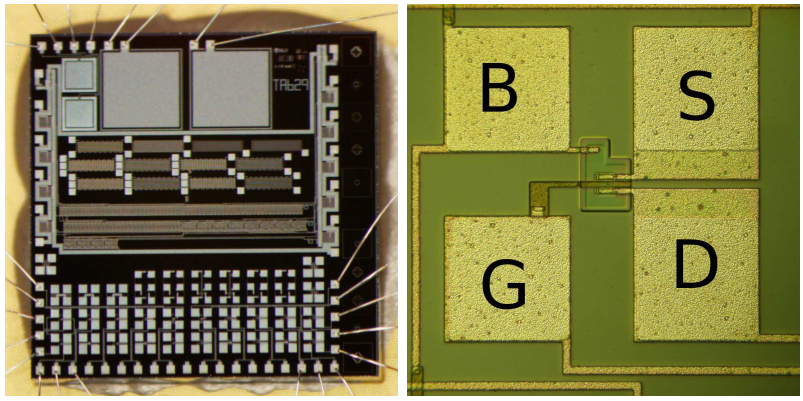

Figure 5.13: Optical micrographs of a TA629 device manufactured by Sandia National Labs, NM, USA. A full die on the left and magnified image of an individual 16x3 µm MOSFET device on the right. The MOSFET devices are located in the lower part of the chip. The gate (G), drain (D), source (S) and base (B) contacts are indicated.

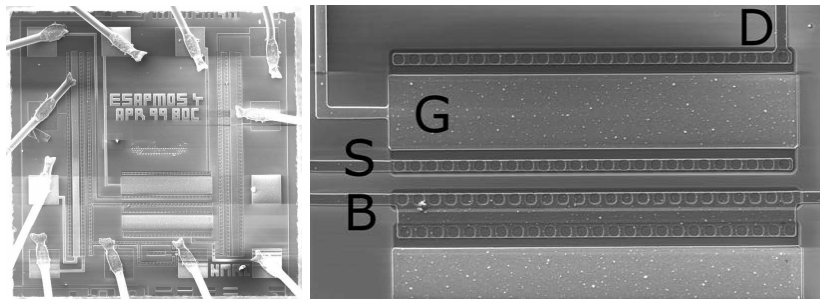

Figure 5.14: Scanning electron micrographs of a RADFET device manufactured by Tyndall National Institute, Ireland. Bare die on the left and the magnification of a 300x50 µm MOSFET-device is on the right hand picture. The gate (G), drain (D), source (S) and base (B) contacts are indicated.

Table 5.3: The ion beams used in the charge yield measurements with their energies before and after the 25 µm Kapton foil and 0.5 cm of air. Also the corresponding LET values in SiO_2 are given as calculated from SRIM-code [53].

Ion	E(initial) [MeV]	E(@ DUT) [MeV]	LET(SiO_2) @ DUT
He-4	20	18.7	0.27
N-15	139	130	2.09
Ar-40	372	320	11.9
Fe-56	523	426	22.2
Xe-131	1217	917	69.6

were performed at RADEF Facility[150] (see Section 4.1.3). All the experiments were done at room temperature.

In the heavy-ion irradiations the beam intensities were typically from 10^5 to $5 \cdot 10^6$ cm^{-2}s^{-1} and the total fluences were in the order of $10^8 - 10^{10}$ ions per cm^2, depending on the device. Some of the ions from the standard RADEF ion cocktail were used at the primary energy of 9.3 MeV/u. The irradiations were performed in air, thus the ion energies were slightly lower than the primary energies. Also an α-particle beam at primary energy of 20 MeV was used. The beam exit window was a 25 µm thick Kapton foil. The devices were placed behind the window at distance of 0.5 cm. The used ions and their energies at the device surface as well as their LET values in SiO_2 are given in Table 5.3 (cf. Table 4.1). The LET values are estimated by using SRIM-code.

During the irradiation, the gate was biased with a fixed positive voltage for both p-type and n-type devices. All the remaining contacts (drain, source and body) were grounded. Because in n-type MOSFETs the substrate is lightly doped with *acceptors*, at positive gate voltages the majority carriers (holes) are depleted from the channel region beneath the gate oxide, and at higher voltage an *inversion* occurs. Conversely, due to *donor* doping in p-type MOSFETs, at positive voltages there is an *accumulation* of electrons in the channel. Several different voltage values were used in order to determine the charge yield dependence on the oxide electric field. As it was discussed in Section 3.3 the recombination of e–h pairs is dependent on the external electric field.

The current-voltage characteristics on the devices were measured before and after each irradiation step by using a HP4145 *Semiconductor Parametric Analyzer*. The gate–to–source voltage V_{gs} was swept from region of *accumulation* to *strong inversion*, while the drain–to–source voltage V_{ds} was kept at a constant values of -2 V and 2 V

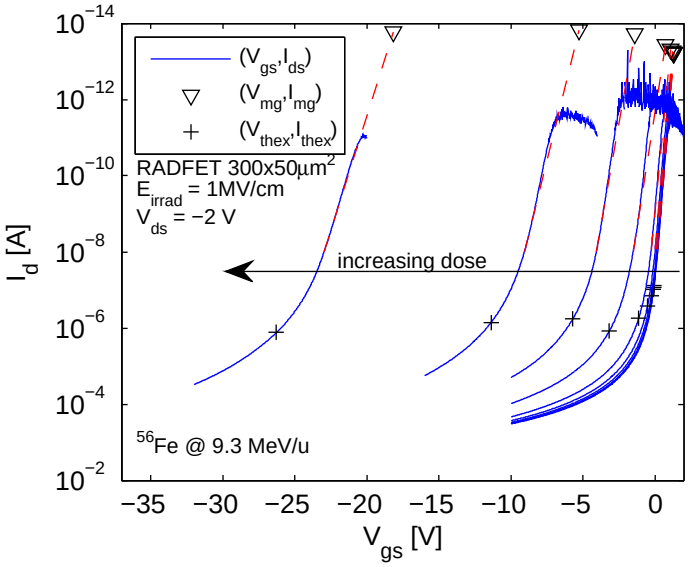

Figure 5.15: The I–V curves for RADFETs with W/L=300/50 irradiated by using Fe-beam at 9.3 MeV/u while an electric field of 1 MV/cm was applied on the gate oxide. There is also indicated points for the midgap and extrapolated threshold voltage for each curve (see text for the definitions for these). Data are previously unpublished.

for p- and n-type TA-629 devices. For RADFETs $V_{ds} = -5\ V$ during the gate sweep. The rest of the pins, i.e. the source and the body, were grounded for all the devices.

The change in the I–V characteristics due to heavy-ion exposure is illustrated in Fig. 5.15. These curves are from the measurements for a pristine RADFET with W/L=300/50 µm and after nine consecutive exposure steps with Fe-beam at 426 MeV, with maximum cumulative dose being 165 krads. The heavy-ion induced total ionizing dose, D, in the gate oxide, given in units[3] of rad, can be estimated from the ion fluence, Φ, by using relation

$$D = 1.602 \cdot 10^{-5} \cdot \Phi \cdot \mathrm{LET}(SiO_2), \tag{5.5}$$

where Φ is given in cm^{-2} and the LET(SiO_2) is the electronic stopping force in SiO_2 in units of MeV/(mg/cm^2). From Fig. 3.6 it can be seen that for ion energies of 10 MeV/u the spatially restricted energy deposition is approximately 90% and 95% of the total energy loss for the mean chord lengths in the Sandia's devices ($\bar{l} \approx 130$ nm) and RADFETs ($\bar{l} \approx 800$ nm), respectively. The used energies were below 9 MeV/u and the overall experimental uncertainty in the beam intensity and current–voltage

[3] 1 rad = 0.01 Gray = 0.01 J/kg

measurements was in the order of ±10%, hence the spatial restriction was ignored and the ion's energy loss and the deposited energy were considered to be equal. Also the effects of straggling were ignored. Eq. (5.5) assumes that all the deposited charge (energy) remains unrecombined.

After different processes, like (1) prompt recombination, (2) diffusion and (3) drift, the radiation induced charge (mainly holes) gets trapped, on one hand in the bulk oxide and the other hand in the Si–SiO_2 interface. The threshold voltage shift, ΔV_{th}, is considered to be a sum of voltage shifts due to *oxide trapped* (ot) and *interface trapped* (it) charge,

$$\Delta V_{th} = \Delta V_{ot} + \Delta V_{it}. \tag{5.6}$$

These voltage shifts are considered to be linearly proportional to the trapped charges as follows

$$\Delta V_{ot} = \frac{\Delta Q_{ot}}{C_{ox}} \tag{5.7}$$

$$\Delta V_{it} = \frac{\Delta Q_{it}}{C_{ox}}, \tag{5.8}$$

where $\Delta Q_{ot,it}$ are the increase in the oxide and the interface trapped charge per cm^2 and C_{ox} is the oxide capacitance in units of F/cm^2. The oxide trapped charge is related to the initial induced charge Q_0 via

$$\begin{aligned} Q_{ot} &= f_{ot} f_\gamma Q_0 \\ Q_{it} &= f_{it}(1 - f_{ot}) f_\gamma Q_0 \end{aligned} \tag{5.9}$$

where f_{ot}, f_{it} and f_γ are coefficients for the charge trapping efficiency in the oxide and the interface, and the charge yield, respectively. All of them have values between 0 and 1. The charge yield is considered to depend only on the radiation type and the oxide field, whereas the trapping efficiencies are highly process dependent. Hence the calculation of the charge yield directly from the deposited charge (or energy) and the voltage shifts is not possible. Alternatively, by comparing device responses between x-rays and heavy ions, the charge yield can be derived. This is done by determining the components in the total threshold voltage shift, namely the ΔV_{ot}. The two trapped charge components Q_{ot} and Q_{it} have different rates of buildup and anneal. In this work the contribution of the oxide trapped charge was used in characterization the

charge yield. The radiation induced ΔV_{ot} can be considered to be dependent only on the total deposited dose and the recombination rate for devices with the same total time of irradiation and anneal, regardless of the radiation source.

The analysis of the I–V curves has been made by using the *midgap technique* presented in Ref. [151]. With this technique the contributions of ΔV_{ot} and ΔV_{it} can be separated. First, the dependence of subthreshold drain current on the gate voltage needs to be defined. According to Ref. [151, and refences therein], in saturation the subthreshold drain current in a MOSFET can be written in form

$$I_d(\phi_s) = \sqrt{2}\frac{W}{L}\frac{e\mu N_d L_B}{2\beta}\left(\frac{n_i}{N_d}\right)^2 \frac{\exp(\beta\phi_s)}{\sqrt{\beta\phi_s}}, \tag{5.10}$$

where ϕ_s is the band bending potential in the Si-surface (in the Si–SiO_2 interface), N_d is the doping concentration in the substrate, n_i in the intrinsic carrier concentration of silicon, $L_B = \sqrt{\frac{\epsilon_s}{\beta e N_d}}$ is the *Debye length* with ϵ_s being the permittivity of silicon, $\beta = \frac{e}{k_B T} \approx 40$ V^{-1} (at room temperature) and μ is the carrier mobility in the Si-channel. The midgap current is defined to occur when the silicon band structure is bent at the Si–SiO_2 interface by value of $\phi_s = \phi_b = \frac{k_B T}{e}\ln\left(\frac{N_d}{n_i}\right)$[152]. Hence the current is written as $I_d(\phi_b) \equiv I_{mg}$. The gate voltage associated with I_{mg} is called the *midgap voltage*, V_{mg}. It has been shown, e.g in Ref. [102], that the shift in the midgap voltage, ΔV_{mg}, can be attributed to oxide trapped charge, i.e. $\Delta V_{ot} = \Delta V_{mg}$, which can be extracted from the I–V curves. The problem is that the I_{mg} values are typically in the order of tens of femtoamperes, which are often below the noise levels of used ammeters. In the subthreshold region $\phi_s \propto V_{g(s)}$, thus due to the exponential dependence of the drain current on the gate voltage as given in Eg. (5.10), the midgap voltages can be derived by extrapolating the I–V curves down to the I_{mg} values. This is illustrated by the red dashed lines in Fig. 5.15 and with the triangles representing the points for I_{mg} and V_{mg}.

At voltages above the threshold, in the saturation region, the MOSFET's drain current can be estimated with the well-known relation

$$|I_d(V_{gs})| = \mu\frac{W}{L}\frac{C_{ox}}{2}(V_{gs} - V_{th})^2, \tag{5.11}$$

where C_{ox} is the gate oxide capacitance. From the I–V data the V_{th} is derived by introducing an *extrapolated threshold voltage*, V_{thex}. Above the threshold $\frac{\partial I_d}{\partial V_{gs}}$ is

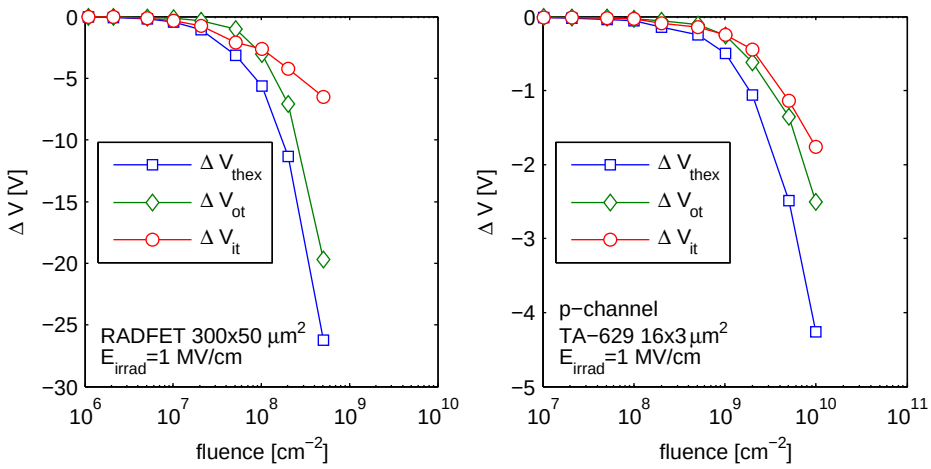

Figure 5.16: Voltage shifts as a function of ion fluence for a RADFET (left) and a TA-692 p-channel device (right) irradiated by Fe-beam at 9.3 MeV/u with oxide field of 1 MV/cm. The contributions from the oxide (ΔV_{ot}) and interface (ΔV_{it}) trapped charge are plotted along with the extrapolated threshold voltage shift (ΔV_{thex}).

linearly proportional to V_{gs}. Thus V_{thex} can be determined from

$$\left.\frac{\partial I_d}{\partial V_{gs}}\right|_{V_{gs}=V_{thex}} = 0 \tag{5.12}$$

via extrapolation. The points for V_{thex} are also indicated in Fig. 5.15. Now ΔV_{th} in Eq. (5.6) is been replaced with ΔV_{thex}, and the contributions of ΔV_{ot} and ΔV_{it} can be extracted accordingly.

An example for the results obtained from the charge separation analysis is presented in Fig. 5.16, where the contributions of the oxide and the interface trapped charges in the total voltage shifts in Fe-irradiated RADFET and p-type TA-629 are plotted as a function of cumulative ion fluence. These graphs are for devices, which have been irradiated by using oxide field of 1 MV/cm. In the left-hand graph for the RADFET one should note that the ΔV_{it} dominates the ΔV_{thex} at fluences below 10^8 cm^{-2}(=1 µm^{-2}), corresponding to ionizing doses below 30 krad. At these fluence levels there are $\sim 1.5 \cdot 10^4$ ion strikes in the gate area of a RADFET with W×L= 300 × 50 µm^2. Typically in pMOS-devices $|\Delta V_{ot}| > |\Delta V_{it}|$ is expected. For TA-629 p-channel devices in this work, $|\Delta V_{it}|$ was observed to be only slightly higher than $|\Delta V_{ot}|$ at lower doses, but generally the behavior was as expected. This can be observed in the right-hand graph in Fig. 5.16. The effect is considered to be a result of

non-uniform distribution of dose in the gate at low fluences (cf. *microdose*). Apparently, if there is less than 1 ion strike per μm^2, the induced charge is not distributed uniformly over the whole gate. This can be qualitatively deduced by considering the ion track structure (see Section 3.2.1). The deposited energy, and thus the e–h pairs are localized strongly in the vicinity of the ion track. This means that the oxide trapped charge from a single ion strike is within a small area. On the other hand, the charge, which is finally trapped in the Si–SiO_2 interface has drifted from its origin to the interface. During the drift process this charge has more likely experienced some spreading laterally, and hence would cover a larger area of the gate compared to the oxide trapped charge.

Because of the thinner oxides in the TA-629 devices they require more TID (fluence) to exhibit similar relative voltage shifts as RADFETs. Hence the non-uniform dose deposition is not that evident in the response of TA-629 devices. Because of this effect, even if the RADFETs exhibited reasonable voltage shifts (few volts) at lower fluences, the final ion fluences were kept above 10^8 cm^{-2}.

Another thing to consider is the *space charge effect*. As charge is accumulated in the oxide, at some point the adjacent charges start to repel each other and cause nonlinear behaviour in the response. This is a concern especially at low oxide fields, but also starts to play a role at higher fields at high cumulated doses. In order to minimize the space charge effect the data were characterized at $\Delta V_{ot} = -0.5$ V for TA-629 devices and $\Delta V_{ot} = -3$ V for RADFETs.

The x-rays and heavy ions exhibit qualitatively the same ΔV_{ot}-behaviour as a function of oxide field: increase with the oxide field at low fields and decrease after reaching a maximum at ~1 MV/cm. According to Ref. [153], the decrease at higher field is due to $E^{-0.5}$ oxide field dependence for the hole capture cross-sections near the Si–SiO_2 interface. The oxide field dependence for both n- and p-type TA-629 devices, measured for x-rays, N- and Fe-ions is illustrated in Fig. 5.17. In the upper graph the total ionizing dose required to induce voltage shift of $\Delta V_{ot} = -0.5$ V is plotted as a function of oxide field. In the lower graph the voltage shifts ΔV_{ot} at fixed TID levels are plotted respectively as a function of oxide field. In these graphs it can be seen that for N- and Fe-ions it requires higher dose levels in order to achieve the same voltage shifts as for the x-ray irradiated devices. This is due to the lower charge yield for heavy ions than that of x-rays. One notable observation can be made in these graphs: for heavy ions, in the p-type devices, more TID is required for the same ΔV_{ot} than in the n-type devices. This would suggest that the charge yield is

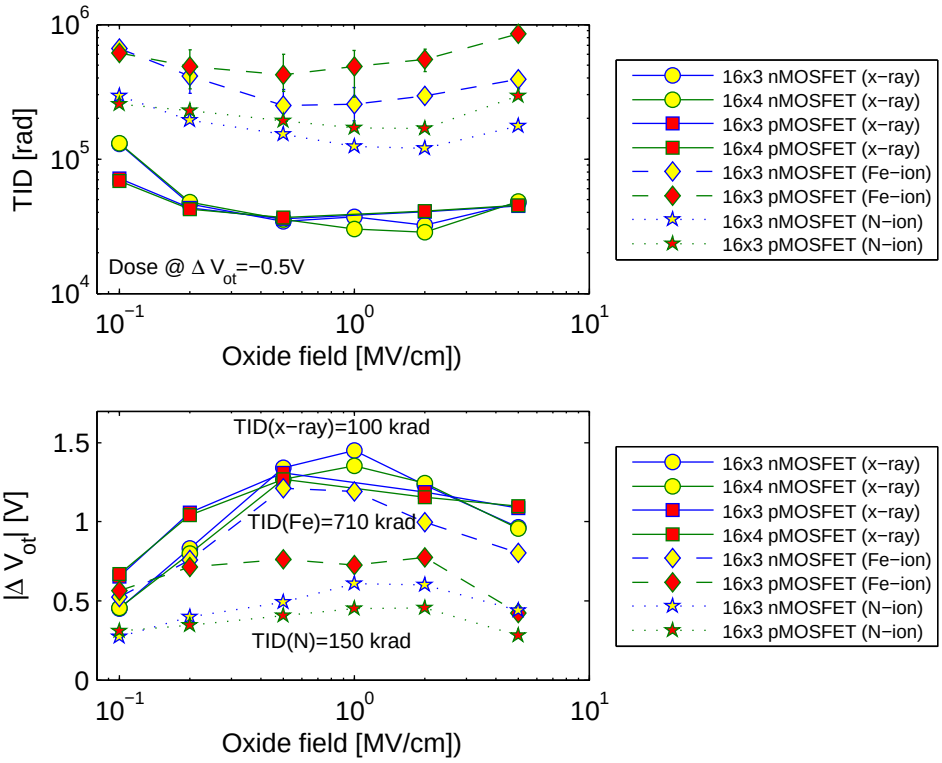

Figure 5.17: The response of n- and p-type TA-629 devices to x-rays, N- and Fe-ions at different oxide fields. In the upper graph the total ionizing dose required to induce shift of $\Delta V_{ot} = -0.5$ V is plotted as a function of electric field. The lower graph presents respectively the ΔV_{ot} values at a fixed TID levels for each device and radiation source combinations. Data previously unpublished.

lower for p-type than for the n-type. This is not observed with x-rays and to author's knowledge this kind of behaviour is not reported previously. The possible reason for this effect is discussed in the next section.

5.2.2 Charge yield results and discussion

The dependence of charge yield on both the oxide field and the initial energy deposition has been experimentally determined. Generally the latter is considered to be described by the LET, like e.g. in Ref. [154, and references therein]. Alternative model has been proposed in Ref. [155, and references therein], where charge yields for different radiation sources are determined via Monte-Carlo simulations. These simulations take into account the spatial distribution of the energy deposition (see

Section 3.2.1) and the results indicate that LET solely does not describe the charge yield. The experimental results, obtained in this current work, support qualitatively the results from the Monte-Carlo simulations in Ref. [155]. The accurate comparison between the experimental data here and the simulation data is not possible due to different energies considered in these works.

In Fig. 5.18 there is a collection of ΔV_{ot} data as a function of total ionizing dose for RADFETs, and n- and p-type TA-629 devices, irradiated with x-rays and several different ions at oxide field of 1 MV/cm. Despite the large *part-to-part* variations observed in the response for heavy ions (especially for ions heavier than nitrogen) in all the devices, the results consistently contradict the models where the charge yield is described solely by the LET. This effect is more readily observed in Fig. 5.19, where the compilation of the charge yield data for different devices, irradiated with different ions at 1 MV/cm oxide field, are presented as a function of LET. E.g. He-ions ($LET = 0.27$ MeV/(mg/cm^2) exhibit lower charge yield than N-ions ($LET = 2.1$ MeV/(mg/cm^2). Also the charge yield for Ar-ions ($LET = 11.9$ MeV/(mg/cm^2) is observed to be in the same level or lower than that of Xe-ions ($LET = 69.6$ MeV/(mg/cm^2) in all the device types. No clear correlation can be seen with the LET. According to the model presented in Ref. [155] and intuitively considering the track structure in Section 3.2.1, the charge yield can be considered to be governed also by the ion velocity (energy). Physical mechanisms underlying the e–h pair recombination in dense plasmas in the ion track are not well established and need further investigations.

The oxide field dependence of the heavy-ion induced charge yield is presented in Fig. 5.20 with comparison of charge yield data found in the literature for gamma rays, x-rays, 2 MeV α-particles, and 12 MeV C-ions. The heavy-ion data obtained in this work exhibit very similar qualitative behaviour as the other radiation sources, which was demonstrated already in Fig. 5.17. This confirms that the electric field dependence of the charge yield is well behaved, regardless of the radiation source. In this context only data for the TA-629 devices are presented, because the RADFETs were tested mainly at 1 MV/cm. Some individual measurement runs were performed for RADFETs also at other oxide field values. Unfortunately the fluence levels in these runs remained too low and the non-uniform dose distribution, mentioned above, was not obtained. Hence these results are not fully applicable for the examination of field-dependence of the charge yield. In addition, in these measurements, RADFETs were observed to fail at high oxide fields (i.e. 5 MV/cm) while irradiating them

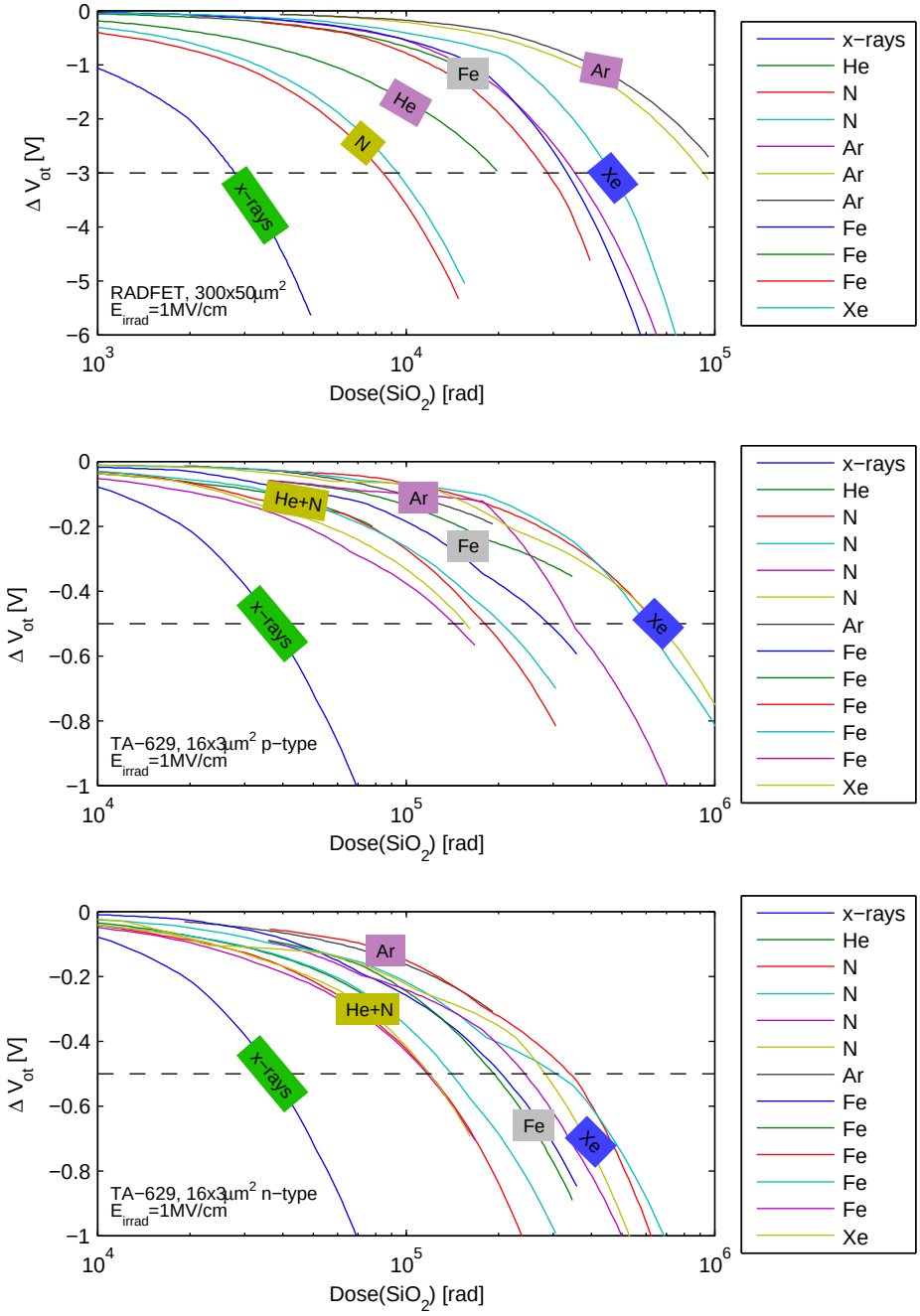

Figure 5.18: ΔV_{ot} as a function of TID for X-rays and various heavy ions measured for RADFETs (top) and both p- (middle) and n-type (bottom) TA-629 devices. Data are previously unpublished.

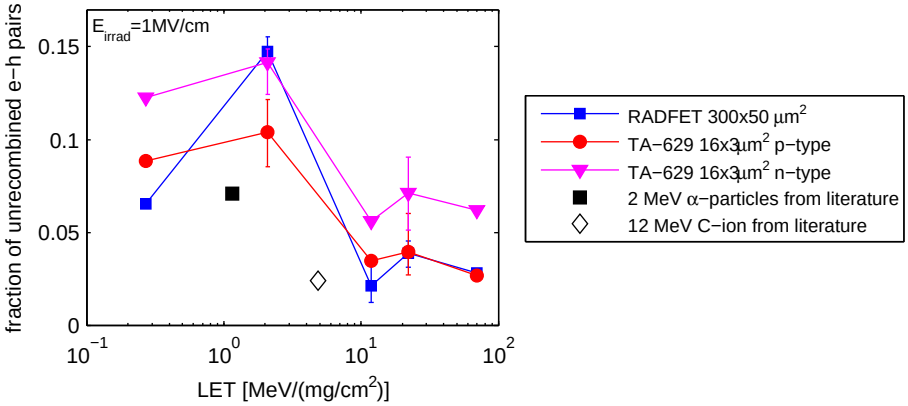

Figure 5.19: Charge yield for different ions in SiO_2 as a function of ion LET at oxide field of 1 MV/cm. The literature data are from Refs. [156] and [155] for 2 MeV α-particles and 12 MeV C-ions, respectively. The rest of the data are previously unpublished.

with Xe- and Fe-ions, presumably due to *Single-Event-Gate-Rupture* (SEGR) (see Section 3.6.2.2). No breakdown was observed in the TA-629 devices at these oxide fields. This observation is in conjunction with the findings in Refs. [157, 158], where the oxide breakdown fields are shown to decrease with increasing oxide thickness, both with and without radiation stress. At oxide field of 1 MV/cm, as presented in Fig. 5.19, no clear correlation can be observed between the charge yield and the oxide thickness. Especially for the heaviest ions, i.e. Fe and Xe, the differences in the obtained charge yields in different p-type devices are within the experimental uncertainties.

As mentioned above, the charge yield in the oxides of MOS devices is expected to be independent on the type of the semiconductor substrate. This is actually the case for the x-ray data obtained in this work. Surprisingly, the heavy-ion data are consistently exhibiting higher charge yields for n-type MOSFETs than that for p-type devices. To the author's knowledge this kind of behaviour has not been reported previously. This could be explained with the combination of (1) the high density e–h pair plasma in the ion track core, and (2) the different amount of accumulated electrons in the Si–SiO_2-interface due to the gate bias and the doping type. At positive gate voltages the n-type transistor is in depletion (or inversion) corresponding to a low number of electrons in the conduction band of silicon channel, whereas in p-type transistor there is higher acculumation of electrons in the channel.

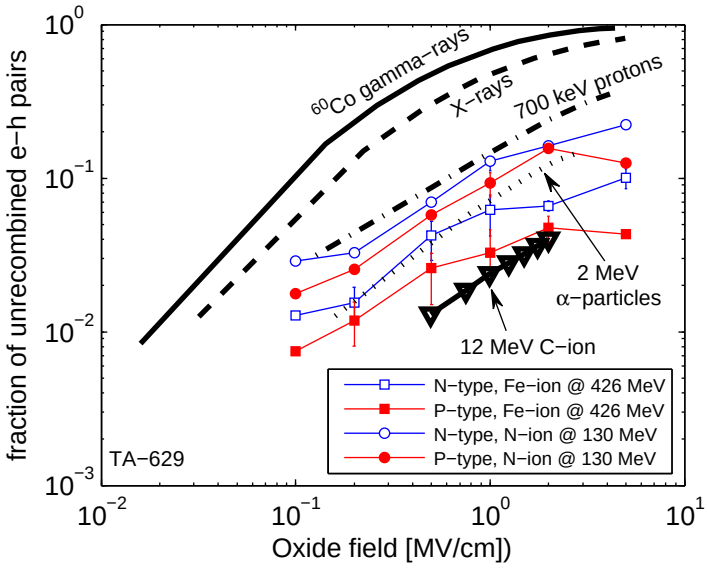

Figure 5.20: The survival rate of e–h pairs generated by different radiation sources in SiO_2 as a function of electric field parallel to the radiation field. Data for 2 MeV α-particles and 700 keV protons are taken from Ref. [156], for x-rays and gamma rays from Ref. [159], and the data for C-ions is from Ref. [155]. The heavy-ion data are previously unpublished except the data for Fe-irradiated n-type (blue hollow squares), which are published in Ref. [138].

Considering the ion strike in the oxide qualitatively. Some evidence of fast charge conduction in the oxides due to heavy-ion strikes has been reported e.g. in Refs. [160, 161, and references therein]. The phenomenon is attributed to the high ionization densities in the heavy-ion track (see Section 3.2.1), which would create a short-lived *conductive pipe* in the oxide. This would suggest that promptly after the heavy-ion strike there might be an injection of electrons from the Si-substrate to the oxide. In case of p-type transistor (n-substrate) the amount of possibly injected charge would be higher compared to n-type transistor (p-substrate). Thus because the final trapped charge in the oxide, causing the voltage shifts, are holes, the assumably higher charge injection in p-type transistor would lead higher recombination of electrons and holes. This would explain the difference in the observed charge yields. For radiation types like x-rays, gamma rays and low LET ions (e.g. protons) this effect would be much weaker due to much lower ionization densities, resulting negligible current conduction and thus lowercharge injection. The thorough exploration of this phenomenon would require such extensive measurements that for the current work no conclusions can

be drawn based on these findings. Plans have been made to investigate this effect further in the future, along with the above mentioned studies of overall recombination of heavy-ion induced e–h pairs in SiO^2.

6 Summary

This thesis provides a review of radiation effects in microelectronics. Different radiation environments in space, atmosphere and on the ground level are discussed. In addition, basic theories on the interaction mechanisms between energetic particles and matter are introduced, followed by discussion about the effects on electronics due to energy deposition by the particles. A semi-empirical model was developed for predicting the electronic stopping force of solids for heavy-ions, which is introduced in this thesis. The model is based on a reasonably simple expression with only three parameters required. The model is used as a basis for a stopping force prediction code, where experimental stopping force data are employed in the parameterization. The developed stopping force code is used by the European Space Agency in its heavy-ion irradiation facilities.

The basic methodology of radiation hardness assurance (RHA) testing of electronics by using heavy ions is presented in this thesis. Utilization of the *RADiation Effects Facility* (RADEF) in RHA testing is introduced, along with the key elements for the RADEF operation: the *K130 cyclotron* and the *Electron Cyclotron Resonance Ion Sources* (ECRIS). RADEF is located in the Accelerator Laboratory (JYFL) of the University of Jyväskylä, Finland. The combination of the JYFL cyclotron and the ECR ion sources has been found very useful for RHA testing due to their capability to produce ion cocktails with high energies (i.e. 9.3 MeV/u). Heavy-ion cocktails are very efficient in RHA testing due to the fast switching between different ion species. The success of RADEF is to a large extent because of the expertise of both the ECR ion source group and the cyclotron staff.

The experimental part of this thesis provides new data on electonic stopping force of silicon for heavy ions, as well as for the heavy-ion induced charge yield in SiO_2. These data improve the knowledge on the interaction mechanisms of heavy ions in silicon, and also on the heavy-ion induced radiation effects in Si and SiO_2. For the heavy-ion stopping force measurements a new method called *Magnetic–Time-Of-Flight* (B–TOF) was developed. The method utilizes the *Lorentz force* and TOF-spectrometry. This method provides a flexible and accurate way of measuring heavy-ion stopping in multiple samples and in wide range of energies. The stopping force measurements done in this work and the B–TOF method have inspired the permanent installation of a TOF-station in RADEF, which is still under construction. It will

be used in heavy-ion stopping measurements especially in materials important for electronics, such as SiO_2 and Ge.

The data for heavy-ion induced charge yield confirms the basic trend in electron–hole pair recombination, which is considered in the literature to be dependent on the density of the deposited energy. To first order it is typically assumed to depend on the LET of the ion. However, the results presented here clearly indicate that the charge yield, i.e. the recombination, is not entirely LET dependent, but also other characteristics (e.g. velocity) of the ion need to be taken into account. Due to the scarcity of charge yield data no solid conclusions can be made on the detailed mechanisms underlying the recombination process, and further investigations are needed. Another finding in the heavy-ion charge yield measurements, which requires further attention, is that p- and n-type devices consistently exhibit different charge yields. This kind of behaviour is not observed with x-rays and, to the author's knowledge, has not been reported previously in the literature.

The technological evolution, with its approach toward nano-scale and the increased use of electronics "everywhere", will inevitably lead to higher demand for radiation hardness assurance, either by testing with irradiation or by design and manufacturing. Clearly this observation makes the topic of this thesis important for the future.

References

[1] Union of Concerned Scientists, "UCS satellite database.". Available from: http://www.ucsusa.org/nuclear_weapons_and_global_security/space_weapons/technical_issues/ucs-satellite-database.html.

[2] D. Binder, E. C. Smith, and A. B. Holman, "Satellite Anomalies from Galactic Cosmic Rays," *IEEE Trans. Nucl. Sci*, vol. 22, pp. 2675 –2680, Dec. 1975. Available from: http://dx.doi.org/10.1109/TNS.1975.4328188.

[3] E. Normand, J. Wert, H. Quinn, T. Fairbanks, S. Michalak, G. Grider, P. Iwanchuk, J. Morrison, S. Wender, and S. Johnson, "First Record of Single-Event Upset on Ground, Cray-1 Computer at Los Alamos in 1976," *IEEE Trans. Nucl. Sci*, vol. 57, pp. 3114 –3120, Dec. 2010. Available from: http://dx.doi.org/10.1109/TNS.2010.2083687.

[4] E. Normand, "Single-event effects in avionics," *IEEE Trans. Nucl. Sci*, vol. 43, pp. 461 –474, Apr 1996. Available from: http://dx.doi.org/10.1109/23.490893.

[5] B. Sierawski, M. Mendenhall, R. Reed, M. Clemens, R. Weller, R. Schrimpf, E. Blackmore, M. Trinczek, B. Hitti, J. Pellish, R. Baumann, S.-J. Wen, R. Wong, and N. Tam, "Muon-induced single event upsets in deep-submicron technology," *IEEE Trans. Nucl. Sci*, vol. 57, pp. 3273 –3278, Dec. 2010. Available from: http://dx.doi.org/10.1109/TNS.2010.2080689.

[6] J. Wallmark and S. Marcus, "Minimum size and maximum packing density of nonredundant semiconductor devices," *Proceedings of the IRE*, vol. 50, pp. 286 – 298, march 1962. Available from: http://dx.doi.org/10.1109/JRPROC.1962.288321.

[7] ACE Science Team, "ACE Level 2 Data.". Available from: http://www.srl.caltech.edu/ACE/ASC/level2/index.html.

[8] D. H. Hathaway, "NASA/Marshall Solar Physics.". Available from: http://solarscience.msfc.nasa.gov/SunspotCycle.shtml.

[9] C.Fröhlich and J. Lean, "The Sun's Total Irradiance: Cycles, Trends and Related Climate Change Uncertainties since 1976," *Geophys.Res.Let.*, vol. 25, pp. 4377–4380, 1998. Available from: http://dx.doi.org/10.1029/1998GL900157.

[10] C. Fröhlich, "Solar Irradiance Variability," in *Solar Variability and Its Effects on Climate, Geophysical Monograph Series* (J. M. Pap, *et al.*, ed.), vol. 141, pp. 97–110, American Geophysical Union, 2004. Available from: http://dx.doi.org/10.1029/141GM09.

[11] "NOAA/NESDIS/NGDC/STP,Boulder-Total Solar Irradiance Data.". Available from: http://www.ngdc.noaa.gov/stp/solar/solarirrad.html.

[12] International Bureau of Weights and Measures and United States. National Bureau of Standards, *The International System of units (SI)*. No. 330–331 in NBS special publication, Dept. of Commerce, National Bureau of Standards : for sale by the Supt. of Docs., U.S. Govt. Print. Off., 1977. Available from: http://books.google.fi/books?id=YvZNdSdeCnEC.

[13] E. Stone, A. Frandsen, R. Mewaldt, E. Christian, D. Margolies, J. Ormes, and F. Snow, "The Advanced Composition Explorer," *Space Science Reviews*, vol. 86, pp. 1–22, 1998. Available from: http://dx.doi.org/10.1023/A:1005082526237.

[14] J. Jokipii, C. Sonett, and M. Giampapa, *Cosmic winds and the heliosphere*. Space science series, University of Arizona Press, 1997. Available from: http://www.google.fi/books?id=8viJVR6xnVYC.

[15] E. Stone, C. Cohen, W. Cook, A. Cummings, B. Gauld, B. Kecman, R. Leske, R. Mewaldt, M. Thayer, B. Dougherty, R. Grumm, B. Milliken, R. Radocinski, M. Wiedenbeck, E. Christian, S. Shuman, and T. von Rosenvinge, "The Solar Isotope Spectrometer for the Advanced Composition Explorer," *Space Science Reviews*, vol. 86, pp. 357–408, 1998. Available from: http://dx.doi.org/10.1023/A:1005027929871.

[16] J. A. V. Allen, C. E. McIlwain, and G. H. Ludwig, "Radiation Observations with Satellite 1958 ε," *J. Geophys. Res.*, vol. 64, no. 3, pp. 271–286, 1959. Available from: http://dx.doi.org/10.1029/JZ064i003p00271.

[17] British Geological Survey - Natural Environment Research Council, "Magnetic poles.". Available from: http://www.geomag.bgs.ac.uk/education/poles.html.

[18] SPENVIS Collaboration, "The Space Environment Information System," 1997–2009. Available from: http://www.spenvis.oma.be.

[19] D. M. Sawyer and J. I. Vette, "AP-8 trapped proton environment for solar maximum and solar minimum," *NASA STIRecon Technical Report N*, vol. 77, pp. 18983–+, 1976. Available from: http://hdl.handle.net/2060/19770012039.

[20] A. L. Vampola, "Outer zone energetic electron environment update," in *High Energy Radiation Background in Space, 1997 Conference on the*, pp. 128 –136, jul 1997. Available from: http://dx.doi.org/10.1109/CHERBS.1997.660263.

[21] A. Tylka, J. Adams, J.H., P. Boberg, B. Brownstein, W. Dietrich, E. Flueckiger, E. Petersen, M. Shea, D. Smart, and E. Smith, "CREME96: A Revision of the Cosmic Ray Effects on Micro-Electronics Code," *IEEE Trans. Nucl. Sci*, vol. 44, pp. 2150 –2160, Dec. 1997. Available from: http://dx.doi.org/10.1109/23.659030.

[22] The CREME Collaboration, "CREME-MC site.". Available from: https://creme.isde.vanderbilt.edu.

[23] A. Viljanen and R. Pirjola, "Geomagnetically induced currents in the finnish high-voltage power system," *Surveys in Geophysics*, vol. 15, pp. 383–408, 1994. Available from: http://dx.doi.org/10.1007/BF00665999.

[24] V. F. Hess, "Über Beobachtungen der durchdringenden Strahlung bei sieben Freiballonfahrten," *Phys. Z.*, vol. 13, pp. 1084–1091, 1912.

[25] J. F. Ziegler and W. A. Lanford, "Effect of Cosmic Rays on Computer Memories," *Science*, vol. 206, no. 4420, pp. 776–788, 1979. Available from: http://www.sciencemag.org/cgi/content/abstract/206/4420/776.

[26] E. Normand, "Single event upset at ground level," *IEEE Trans. Nucl. Sci*, vol. 43, pp. 2742 –2750, Dec. 1996. Available from: http://dx.doi.org/10.1109/23.556861.

[27] T. May and M. Woods, "Alpha-particle-induced soft errors in dynamic memories," *IEEE Trans. Electron. Dev.*, vol. 26, pp. 2 – 9, Jan. 1979. Available from: http://dx.doi.org/10.1109/T-ED.1979.19370.

[28] J. F. Ziegler, H. W. Curtis, H. P. Muhlfeld, C. J. Montrose, B. Chin, M. Nicewicz, C. A. Russell, W. Y. Wang, L. B. Freeman, P. Hosier, L. E. LaFave, J. L. Walsh, J. M. Orro, G. J. Unger, J. M. Ross, T. J. O'Gorman, B. Messina, T. D. Sullivan, A. J. Sykes, H. Yourke, T. A. Enger, V. Tolat, T. S. Scott, A. H. Taber, R. J. Sussman, W. A. Klein, and C. W. Wahaus, "IBM experiments in soft fails in computer electronics (1978 – 1994)," *IBM J. of Res. and Dev.*, vol. 40, pp. 3 –18, Jan. 1996. Available from: http://dx.doi.org/10.1147/rd.401.0003.

[29] E. Ibe, H. Taniguchi, Y. Yahagi, K.-i. Shimbo, and T. Toba, "Impact of Scaling on Neutron-Induced Soft Error in SRAMs From a 250 nm to a 22 nm Design Rule," *IEEE Trans. Electron. Dev.*, vol. 57, pp. 1527 –1538, Jul. 2010. Available from: http://dx.doi.org/10.1109/TED.2010.2047907.

[30] M. Mason, "Cosmic rays damage automotive electronics," May 2006. Available from: http://www.eetimes.com/design/automotive-design/4011077/Cosmic-rays-damage-automotive-electronics.

[31] L. Dominik, E. Normand, M. Dion, and P. Ferguson, "Proposal for a new integrated circuit and electronics neutron experiment source at Oak Ridge National laboratory," in *IEEE Int. Rel. Phys. Symp.*, pp. 940 –947, Apr. 2009. Available from: http://dx.doi.org/10.1109/IRPS.2009.5173385.

[32] Bloomberg, "Delta, Qantas, Air Canada Divert Flights Due to Solar Storm," Jan 2012. Available from: http://www.bloomberg.com/news/2012-01-24/delta-reroutes-some-flights-on-solar-flare.html.

[33] *The IEE Seminar on Cosmic Radiation Single Event Effects and Avionics, 2005 (Ref. No. 2005/11270)*, Dec. 2005.

[34] P. Grieder, *Cosmic rays at Earth: researcher's reference manual and data book*. Elsevier Science Ltd., 2001. Available from: http://books.google.com/books?id=MwwRhQ7qEAsC.

[35] J. Kotz, P. Treichel, and J. Townsend, *Chemistry and chemical reactivity*. Thomson Brooks/Cole, 7th ed., 2009. Available from: http://books.google.fi/books?id=jcn6sgt7RpoC.

[36] G. Sai-Halasz, M. Wordeman, and R. Dennard, "Alpha-particle-induced soft error rate in VLSI circuits," *IEEE Trans. Electron. Dev.*, vol. 29, pp. 725 – 731, apr 1982. Available from: http://dx.doi.org/10.1109/T-ED.1982.20769.

[37] K. Itoh, R. Hori, H. Masuda, Y. Kamigaki, H. Kawamoto, and H. Katto, "A single 5V 64K dynamic RAM," in *Solid-State Circuits Conference. Digest of Technical Papers. 1980 IEEE International*, vol. XXIII, pp. 228 – 229, Feb. 1980. Available from: http://dx.doi.org/10.1109/ISSCC.1980.1156076.

[38] S. Martinie, J. Autran, S. Uznanski, P. Roche, G. Gasiot, D. Munteanu, and S. Sauze, "Alpha-Particle Induced Soft-Error Rate in CMOS 130 nm SRAM," *IEEE Trans. Nucl. Sci*, vol. 58, pp. 1086 –1092, Jun. 2011. Available from: http://dx.doi.org/10.1109/TNS.2010.2102363.

[39] R. Wong, P. Su, S.-J. Wen, B. McNally, and S. Coleman, "The effect of radon on soft error rates for wire bonded memories," in *Integrated Reliability Workshop Final Report (IRW), 2010 IEEE International*, pp. 133 –134, oct. 2010. Available from: http://dx.doi.org/10.1109/IIRW.2010.5706506.

[40] I. Batkin, R. B. del Re, J.-G. Boutin, and J. Armitage, "γ -spectroscopy investigation of radon daughter deposition on electrostatically charged surfaces," *Phys. Med. Biol.*, vol. 43, no. 3, p. 487, 1998. Available from: http://stacks.iop.org/0031-9155/43/i=3/a=002.

[41] E. Segrè, "Fermi and neutron physics," *Rev. Mod. Phys.*, vol. 27, pp. 257–263, Jul. 1955. Available from: http://dx.doi.org/10.1103/RevModPhys.27.257.

[42] R. C. Baumann and E. B. Smith, "Neutron-induced ^{10}B fission as a major source of soft errors in high density SRAMs," *Microelec. Rel*, vol. 41, no. 2, pp. 211 – 218, 2001. Available from: http://www.sciencedirect.com/science/article/pii/S0026271400002183.

[43] L. Berkhouse, S. E. Davis, F. R. Gladeck, J. H. Hallowell, and C. B. Jones, "Operation DOMINIC I-1962," Tech. Rep. DNA 6040F, Kaman Tempo, Feb 1983. accessed: 20 May 2011. Available from: http://handle.dtic.mil/100.2/ADA136820.

[44] S. L. Simon and W. L. Robison, "A compilation of nuclear weapons test detonation data for US Pacific Ocean tests," *Health Phys.*, vol. 73, pp. 258–264, Jul. 1997.

[45] P. Sigmund, *Stopping of Heavy Ions - A Theoretical Approach*. Springer, 2004.

[46] P. Sigmund, "Stopping power: Wrong terminology," *ICRU News*, 2000.

[47] N. Bohr, "On the theory of the decrease of velocity of moving electrified particles on passing through matter," *Philos. Mag. Ser. 6*, vol. 25, no. 145, pp. 10–31, 1913.

[48] N. Bohr, "On the decrease of velocity of swiftly moving electrified particles in passing through matter," *Philos. Mag. Ser. 6*, vol. 30, no. 178, pp. 581–612, 1915.

[49] N. Bohr, "The penetration of atomic particles through matter," *Kgl. Danske Videnskab. Selskab, Mat.-Fys. Medd.*, vol. 18, no. 8, pp. 1–144, 1948.

[50] P. Sigmund, *Particle Penetration and Radiation Effects - General Aspects and Stopping of Swift Point Charges*. Springer, 2006.

[51] J. Lindhard and A. H. Sørensen, "Relativistic theory of stopping for heavy ions," *Phys. Rev. A*, vol. 53, pp. 2443–2456, Apr 1996. Available from: http://link.aps.org/doi/10.1103/PhysRevA.53.2443.

[52] A. Javanainen, "A simple expression for electronic stopping force of heavy ions in solids," *Nucl. Instrum. Methods Phys. Res., Sect. B (in press)*, 2012. Available from: http://dx.doi.org/10.1016/j.nimb.2012.05.013.

[53] J. F. Ziegler, J. P. Biersack, M. Ziegler, D. J. Marwick, G. A. Cuomo, W. A. Porter, and S. A. Harrison, "SRIM 2011 code," 1984-2011. Available from: http://www.srim.org.

[54] H. Paul, "Stopping power graphs.". Available from: http://www.exphys.jku.at/stopping/.

[55] F. Bloch, "Zur bremsung rasch bewegter teilchen beim durchgang durch materie," *Annalen der Physik*, vol. 408, no. 3, pp. 285–320, 1933. Available from: http://dx.doi.org/10.1002/andp.19334080303.

[56] A. Javanainen, M. Sillanpää, W. H. Trzaska, A. Virtanen, G. Berger, W. Hajdas, R. Harboe-Sørensen, H. Kettunen, T. Malkiewicz, M. Mutterer, J. Perkowski, A. Pirojenko, I. Riihimäki, T. Sajavaara, G. Tyurin, and H. J. Whitlow, "Experimental Linear Energy Transfer of heavy ions in silicon for RADEF cocktail species," *IEEE Trans. Nucl. Sci*, vol. 56, pp. 2242–2246, Aug. 2009. Available from: http://dx.doi.org/10.1109/TNS.2008.2009983.

[57] A. Javanainen, T. Malkiewicz, J. Perkowski, W. H. Trzaska, A. Virtanen, G. Berger, W. Hajdas, R. Harboe-Sørensen, H. Kettunen, V. Lyapin, M. Mutterer, A. Pirojenko, I. Riihimäki, T. Sajavaara, G. Tyurin, and H. J. Whitlow, "Linear energy transfer of heavy ions in silicon," *IEEE Trans. Nucl. Sci*, vol. 54, pp. 1158–1162, Aug. 2007. Available from: http://dx.doi.org/10.1109/TNS.2007.895121.

[58] N. Bohr, "Scattering and stopping of fission fragments," *Phys. Rev.*, vol. 58, pp. 654–655, Oct 1940. Available from: http://link.aps.org/doi/10.1103/PhysRev.58.654.

[59] G. Schiwietz and P. Grande, "Improved charge-state formulas," *Nucl. Instrum. Methods Phys. Res., Sect. B*, vol. 175-177, pp. 125 – 131, 2001. Available from: http://www.sciencedirect.com/science/article/pii/S0168583X00005838.

[60] J. Knipp and E. Teller, "On the energy loss of heavy ions," *Phys. Rev.*, vol. 59, pp. 659–669, Apr. 1941. Available from: http://link.aps.org/doi/10.1103/PhysRev.59.659.

[61] L. C. Northcliffe, "Passage of Heavy Ions Through Matter," *Annual Review of Nuclear Science*, vol. 13, no. 1, pp. 67–102, 1963. Available from: http://www.annualreviews.org/doi/abs/10.1146/annurev.ns.13.120163.000435.

[62] P. Sigmund and A. Schinner, "Effective charge and related/unrelated quantities in heavy-ion stopping," *Nucl. Instrum. Methods Phys. Res., Sect. B*, vol. 174, no. 4, pp. 535 – 540, 2001. Available from: http://www.sciencedirect.com/science/article/pii/S0168583X01003172.

[63] H. Andersen, "The depth resolution of sputter profiling," *Appl. Phys. A: Mater. Sci. Process.*, vol. 18, pp. 131–140, 1979. Available from: http://dx.doi.org/10.1007/BF00934407.

[64] F. Yang and J. Hamilton, *Modern Atomic and Nuclear Physics*. World Scientific Pub Co., 2009. Available from: http://books.google.fi/books?id=LXv8Xh3GE6oC.

[65] J. Lilley, *Nuclear Physics - Principles and Applications*. John Wiley & Sons Ltd., 2001.

[66] I. Jun, M. Xapsos, S. Messenger, E. Burke, R. Walters, G. Summers, and T. Jordan, "Proton nonionizing energy loss (NIEL) for device applications," *IEEE Trans. Nucl. Sci*, vol. 50, pp. 1924 – 1928, Dec. 2003. Available from: http://dx.doi.org/10.1109/TNS.2003.820760.

[67] P. Dodd, J. Schwank, M. Shaneyfelt, V. Ferlet-Cavrois, P. Paillet, J. Baggio, G. Hash, J. Felix, K. Hirose, and H. Saito, "Heavy Ion Energy Effects in CMOS SRAMs," *IEEE Trans. Nucl. Sci.*, vol. 54, pp. 889 –893, Aug. 2007. Available from: http://dx.doi.org/10.1109/TNS.2007.893425.

[68] Y. Varshni, "Temperature dependence of the energy gap in semiconductors," *Physica*, vol. 34, no. 1, pp. 149 – 154, 1967. Available from: http://www.sciencedirect.com/science/article/pii/0031891467900626.

[69] T. DiStefano and D. Eastman, "The band edge of amorphous SiO_2 by photoinjection and photoconductivity measurements," *Solid State Commun.*, vol. 9, no. 24, pp. 2259 – 2261, 1971. Available from: http://www.sciencedirect.com/science/article/pii/0038109871906430.

[70] R. C. Alig and S. Bloom, "Electron-hole-pair creation energies in semiconductors," *Phys. Rev. Lett.*, vol. 35, pp. 1522–1525, Dec. 1975. Available from: http://link.aps.org/doi/10.1103/PhysRevLett.35.1522.

[71] J. M. Benedetto and H. E. Boesch, "The Relationship between ^{60}Co and 10-keV X-Ray Damage in MOS Devices," *IEEE Trans. Nucl. Sci*, vol. 33, pp. 1317 –1323, dec. 1986. Available from: http://dx.doi.org/10.1109/TNS.1986.4334599.

[72] R. Harboe-Sorensen, C. Poivey, F.-X. Guerre, A. Roseng, F. Lochon, G. Berger, W. Hajdas, A. Virtanen, H. Kettunen, and S. Duzellier, "From the Reference SEU Monitor to the Technology Demonstration Module On-Board PROBA-II," *IEEE Trans. Nucl. Sci*, vol. 55, pp. 3082 –3087, Dec. 2008. Available from: http://dx.doi.org/10.1109/TNS.2008.2006896.

[73] R. Harboe-Sorensen, F.-X. Guerre, and A. Roseng, "Design, Testing and Calibration of a "Reference SEU Monitor" System," in *Radiation and Its Effects on Components and Systems, 2005. RADECS 2005. 8th European Conference on*, pp. B3–1 –B3–7, Sept. 2005. Available from: http://dx.doi.org/10.1109/RADECS.2005.4365561.

[74] G. Messenger and M. Ash, *Single event phenomena*. Chapman & Hall, 1997. Available from: http://books.google.fi/books?id=ntOx9bMHYyQC.

[75] M. A. Xapsos, "A Spatially Restricted Linear Energy Transfer Equation," *Radiat. Res.*, vol. 132, pp. 282–287, Dec. 1992. Available from: http://www.jstor.org/stable/3578235.

[76] M. Xapsos, "Applicability of LET to single events in microelectronic structures," *IEEE Trans. Nucl. Sci*, vol. 39, pp. 1613 –1621, Dec. 1992. Available from: http://dx.doi.org/10.1109/23.211343.

[77] M. A. Xapsos, G. P. Summers, E. A. Burke, and C. Poivey, "Microdosimetry theory for microelectronics applications," *Nucl. Instrum. Methods Phys. Res., Sect. B*, vol. 184, no. 1-2, pp. 113–134, 2001. Available from: http://www.sciencedirect.com/science/article/pii/S0168583X01007169.

[78] J. J. Butts and R. Katz, "Theory of RBE for Heavy Ion Bombardment of Dry Enzymes and Viruses," *Radiat. Res.*, vol. 30, pp. 855–871, Apr 1967.

[79] R. Katz, "Track structure theory in radiobiology and in radiation detection," *Nuclear Track Detection*, vol. 2, no. 1, pp. 1 – 28, 1978. Available from: http://www.sciencedirect.com/science/article/pii/0145224X78900029.

[80] F. A. Cucinotta, R. Katz, and J. W. Wilson, "Radial distribution of electron spectra from high-energy ions," *Radiation and Environmental Biophysics*, vol. 37, pp. 259–265, 1998. Available from: http://dx.doi.org/10.1007/s004110050127.

[81] B. Grosswendt, S. Pszona, and A. Bantsar, "NEW DESCRIPTORS OF RADIATION QUALITY BASED ON NANODOSIMETRY, A FIRST APPROACH," *Radiation Protection Dosimetry*, May 2007. Available from: http://rpd.oxfordjournals.org/content/early/2007/05/12/rpd.ncm088.abstract.

[82] K. M. Prise, G. Schettino, M. Folkard, and K. D. Held, "New insights on cell death from radiation exposure," *The Lancet Oncology*, vol. 6, no. 7, pp. 520 – 528, 2005. Available from: http://www.sciencedirect.com/science/article/pii/S1470204505702461.

[83] "The International Technology Roadmap for Semiconductors.". Available from: http://www.itrs.net/reports.html.

[84] Intel, "Microprocessor Quick Reference Guide.". Available from: http://www.intel.com/pressroom/kits/quickref.htm.

[85] Z. Chunxiang, D. Dunn, and R. Katz, "Radial distribution of dose and cross-sections for the inactivation of dry enzymes and viruses," *Radiation Protection Dosimetry*, vol. 13, no. 1-4, pp. 215–218, 1985. Available from: http://rpd.oxfordjournals.org/content/13/1-4/215.abstract.

[86] M. Waligórski, R. Hamm, and R. Katz, "The radial distribution of dose around the path of a heavy ion in liquid water," *Int. J. of Radiat. Appl. Instrum. Part D.*, vol. 11, no. 6, pp. 309 – 319, 1986. Available from: http://www.sciencedirect.com/science/article/pii/1359018986900579.

[87] O. Fageeha, J. Howard, and R. C. Block, "Distribution of radial energy deposition around the track of energetic charged particles in silicon," *J. Appl. Phys.*, vol. 75, no. 5, pp. 2317–2321, 1994. Available from: http://link.aip.org/link/?JAP/75/2317/1.

[88] J. C. Ashley, C. J. Tung, R. H. Ritchie, and V. E. Anderson, "Calculations of mean free paths and stopping powers of low energy electrons ($\leq$10 kev) in solids using a statistical model," *IEEE Trans. Nucl. Sci*, vol. 23, pp. 1833 –1837, dec. 1976. Available from: http://dx.doi.org/10.1109/TNS.1976.4328586.

[89] M. Berger, J. Coursey, M. Zucker, and J. Chang, "ESTAR - Stopping-power and range tables for electrons." webpage, Aug 2005. Available from: http://physics.nist.gov/PhysRefData/Star/Text/ESTAR.html.

[90] S. Agostinelli, J. Allison, K. Amako, J. Apostolakis, H. Araujo, P. Arce, M. Asai, D. Axen, S. Banerjee, G. Barrand, F. Behner, L. Bellagamba, J. Boudreau, L. Broglia, A. Brunengo, H. Burkhardt, S. Chauvie, J. Chuma, R. Chytracek,

G. Cooperman, G. Cosmo, P. Degtyarenko, A. Dell'Acqua, G. Depaola, D. Dietrich, R. Enami, A. Feliciello, C. Ferguson, H. Fesefeldt, G. Folger, F. Foppiano, A. Forti, S. Garelli, S. Giani, R. Giannitrapani, D. Gibin, J. G. Cadenas, I. González, G. G. Abril, G. Greeniaus, W. Greiner, V. Grichine, A. Grossheim, S. Guatelli, P. Gumplinger, R. Hamatsu, K. Hashimoto, H. Hasui, A. Heikkinen, A. Howard, V. Ivanchenko, A. Johnson, F. Jones, J. Kallenbach, N. Kanaya, M. Kawabata, Y. Kawabata, M. Kawaguti, S. Kelner, P. Kent, A. Kimura, T. Kodama, R. Kokoulin, M. Kossov, H. Kurashige, E. Lamanna, T. Lampén, V. Lara, V. Lefebure, F. Lei, M. Liendl, W. Lockman, F. Longo, S. Magni, M. Maire, E. Medernach, K. Minamimoto, P. M. de Freitas, Y. Morita, K. Murakami, M. Nagamatu, R. Nartallo, P. Nieminen, T. Nishimura, K. Ohtsubo, M. Okamura, S. O'Neale, Y. Oohata, K. Paech, J. Perl, A. Pfeiffer, M. Pia, F. Ranjard, A. Rybin, S. Sadilov, E. D. Salvo, G. Santin, T. Sasaki, N. Savvas, Y. Sawada, S. Scherer, S. Sei, V. Sirotenko, D. Smith, N. Starkov, H. Stoecker, J. Sulkimo, M. Takahata, S. Tanaka, E. Tcherniaev, E. S. Tehrani, M. Tropeano, P. Truscott, H. Uno, L. Urban, P. Urban, M. Verderi, A. Walkden, W. Wander, H. Weber, J. Wellisch, T. Wenaus, D. Williams, D. Wright, T. Yamada, H. Yoshida, and D. Zschiesche, "Geant4—a simulation toolkit," *Nucl. Instrum. Methods Phys. Res., Sect. A*, vol. 506, no. 3, pp. 250 – 303, 2003. Available from: http://www.sciencedirect.com/science/article/pii/S0168900203013688.

[91] J. Allison, K. Amako, J. Apostolakis, H. Araujo, P. Dubois, M. Asai, G. Barrand, R. Capra, S. Chauvie, R. Chytracek, G. Cirrone, G. Cooperman, G. Cosmo, G. Cuttone, G. Daquino, M. Donszelmann, M. Dressel, G. Folger, F. Foppiano, J. Generowicz, V. Grichine, S. Guatelli, P. Gumplinger, A. Heikkinen, I. Hrivnacova, A. Howard, S. Incerti, V. Ivanchenko, T. Johnson, F. Jones, T. Koi, R. Kokoulin, M. Kossov, H. Kurashige, V. Lara, S. Larsson, F. Lei, O. Link, F. Longo, M. Maire, A. Mantero, B. Mascialino, I. McLaren, P. Lorenzo, K. Minamimoto, K. Murakami, P. Nieminen, L. Pandola, S. Parlati, L. Peralta, J. Perl, A. Pfeiffer, M. Pia, A. Ribon, P. Rodrigues, G. Russo, S. Sadilov, G. Santin, T. Sasaki, D. Smith, N. Starkov, S. Tanaka, E. Tcherniaev, B. Tome, A. Trindade, P. Truscott, L. Urban, M. Verderi, A. Walkden, J. Wellisch, D. Williams, D. Wright, and H. Yoshida, "Geant4 developments and applications," *IEEE Trans. Nucl. Sci*, vol. 53, pp. 270 –278, Feb. 2006. Available from: http://dx.doi.org/10.1109/TNS.2006.869826.

[92] J. F. Ziegler, J. P. Biersack, and U. Littmark, *The Stopping and Range of Ions in Solids*. Pergamon Press, 1985.

[93] V. Zajic, "TVDG LET Calculator," 2001. Available from: http://tvdg10.phy.bnl.gov/let.html.

[94] V. Zajic and P. Thieberger, "Heavy ion linear energy transfer measurements during single event upset testing of electronic devices," *IEEE Trans. Nucl. Sci*, vol. 46, pp. 59 –69, feb 1999. Available from: http://dx.doi.org/10.1109/23.747768.

[95] A. Javanainen, W. H. Trzaska, R. Harboe-Sørensen, A. Virtanen, G. Berger, and W. Hajdas, "ECIF Cocktail Calculator.". Available from: https://www.jyu.fi/accelerator/radef/ECIFCalc.

[96] P. Sigmund, "PASS code." private communications.

[97] P. Sigmund and A. Schinner, "Binary theory of electronic stopping," *Nucl. Instrum. Methods Phys. Res., Sect. B*, vol. 195, no. 1–2, pp. 64 – 90, 2002. Available from: http://www.sciencedirect.com/science/article/pii/S0168583X01011624.

[98] G. Schiwietz and P. L. Grande, "Convolution approximation for swift Particles.". Available from: http://www.casp-program.org/.

[99] P. L. Grande and G. Schiwietz, "Convolution approximation for the energy loss, ionization probability and straggling of fast ions," *Nucl. Instrum. Methods Phys. Res., Sect. B*, vol. 267, no. 6, pp. 859 – 865, 2009. Available from: http://www.sciencedirect.com/science/article/pii/S0168583X0900216X.

[100] F. Hubert, R. Bimbot, and H. Gauvin, "Range and stopping-power tables for 2.5–500 MeV/nucleon heavy ions in solids," *Atomic Data and Nuclear Data Tables*, vol. 46, no. 1, pp. 1 – 213, 1990. Available from: http://www.sciencedirect.com/science/article/pii/0092640X9090001Z.

[101] Geant4 Collaboration, "Geant4: A toolkit for the simulation of the passage of particles through matter." http://www.geant4.org/geant4/.

[102] T. P. Ma and P. V. Dressendorfer, eds., *Ionizing Radiation Effects in MOS Devices and Circuits*. John Wiley & Sons Inc., 1989.

[103] T. Oldham and F. McLean, "Total ionizing dose effects in MOS oxides and devices," *IEEE Trans. Nucl. Sci*, vol. 50, pp. 483 – 499, June 2003. Available from: http://dx.doi.org/10.1109/TNS.2003.812927.

[104] Y. Zhang and W. J. Weber, "Role of energy partitioning on electron-hole recombination, trapping, and detection in silicon detectors," *Phys. Rev. B*, vol. 82, p. 075202, Aug. 2010. Available from: http://dx.doi.org/10.1103/PhysRevB.82.075202.

[105] O. Tarvainen. private communication.

[106] M. Bühler and E. Umlauf, "A magnetic bolometer for single-particle detection," *EPL (Europhysics Letters)*, vol. 5, no. 4, p. 297, 1988. Available from: http://stacks.iop.org/0295-5075/5/i=4/a=003.

[107] P. Sigmund, ed., *Ion Beam Science: Solved and Unsolved Problems*, vol. 52 of *Matematisk-fysiske Meddelelser*. Det Kongelige Danske Videnskabernes Selskab, 2006.

[108] A. Meftah, F. Brisard, J. M. Costantini, E. Dooryhee, M. Hage-Ali, M. Hervieu, J. P. Stoquert, F. Studer, and M. Toulemonde, "Track formation in SiO_2 quartz and the thermal-spike mechanism," *Phys. Rev. B*, vol. 49, pp. 12457–12463, May 1994. Available from: http://link.aps.org/doi/10.1103/PhysRevB.49.12457.

[109] P. Kluth, C. S. Schnohr, O. H. Pakarinen, F. Djurabekova, D. J. Sprouster, R. Giulian, M. C. Ridgway, A. P. Byrne, C. Trautmann, D. J. Cookson, K. Nordlund, and M. Toulemonde, "Fine structure in swift heavy ion tracks in amorphous sio_2," *Phys. Rev. Lett.*, vol. 101, p. 175503, Oct. 2008. Available from: http://link.aps.org/doi/10.1103/PhysRevLett.101.175503.

[110] S. Messenger, E. Burke, G. Summers, M. Xapsos, R. Walters, E. Jackson, and B. Weaver, "Nonionizing energy loss (NIEL) for heavy ions," *IEEE Trans. Nucl. Sci*, vol. 46, pp. 1595 –1602, Dec. 1999. Available from: http://dx.doi.org/10.1109/23.819126.

[111] S. Messenger, E. Burke, M. Xapsos, G. Summers, R. Walters, I. Jun, and T. Jordan, "NIEL for heavy ions: an analytical approach," *IEEE Trans. Nucl. Sci*, vol. 50, pp. 1919 – 1923, Dec. 2003. Available from: http://dx.doi.org/10.1109/TNS.2003.820762.

[112] R. Pease, "Total ionizing dose effects in bipolar devices and circuits," *IEEE Trans. Nucl. Sci*, vol. 50, pp. 539 – 551, Jun. 2003. Available from: http://dx.doi.org/10.1109/TNS.2003.813133.

[113] Electronic Industries Association, *Test Procedures for the Measurement of Single-Event Effects in Semiconductor Devices from Heavy Ion Irradiation*, Dec. 1996. EIA/JEDEC Standard No. 57.

[114] JEDEC Solid State Technology Association, *Measurement and Reporting of Alpha Particle and Terrestrial Cosmic Ray-Induced Soft Errors in Semiconductor Devices*, Oct. 2006. JEDEC Standard No. 89A.

[115] P. Adell, R. Schrimpf, C. Cirba, W. Holman, X. Zhu, H. Barnaby, and O. Mion, "Single event transient effects in a voltage reference," *Microelectronics Reliability*, vol. 45, no. 2, pp. 355 – 359, 2005. Available from: http://www.sciencedirect.com/science/article/pii/S0026271404003567.

[116] N. Avirneni and A. Somani, "Low overhead soft error mitigation techniques for high-performance and aggressive designs," *Computers, IEEE Transactions on*, vol. 61, pp. 488 –501, Apr. 2012. Available from: http://dx.doi.org/10.1109/TC.2011.31.

[117] M. Nicolaidis, *Soft Errors in Modern Electronic Systems*. Frontiers in Electronic Testing, Springer, 2010. Available from: http://books.google.fi/books?id=WCqrOkMExu8C.

[118] F. Sexton, "Destructive single-event effects in semiconductor devices and ICs," *IEEE Trans. Nucl. Sci*, vol. 50, pp. 603 – 621, Jun. 2003. Available from: http://dx.doi.org/10.1109/TNS.2003.813137.

[119] J. Schwank, V. Ferlet-Cavrois, M. Shaneyfelt, P. Paillet, and P. Dodd, "Radiation effects in soi technologies," *IEEE Trans. Nucl. Sci*, vol. 50, pp. 522 – 538, Jun. 2003. Available from: http://dx.doi.org/10.1109/TNS.2003.812930.

[120] European Space Agency, *Single Event Effects Test Method and Guidelines*, 1 ed., October 1995. ESA/SCC Basic Specification No. 25100.

[121] European Space Agency, *Total Dose Steady-State Irradiation Test Method*, 1 ed., October 2010. ESA/SCC Basic Specification No. 22900.

[122] Department of Defence, United States of America, *Test Method Standard - Microcircuits*, H ed., Feb. 2010. MIL-STD-883. Available from: http://www.landandmaritime.dla.mil/programs/milspec/ListDocs.asp?BasicDoc=MIL-STD-883.

[123] ASTM International, *Standard Guide for the Measurement of Single Event Phenomena (SEP) Induced by Heavy Ion Irradiation of Semiconductor Devices*, 2006. ASTM F1192.

[124] International Atomic Energy Agency - Nuclear Data Service, "Live Chart of Nuclides.". Available from: http://www-nds.iaea.org/relnsd/vchart/index.html.

[125] R. Harboe-Sorensen, C. Poivey, N. Fleurinck, K. Puimege, A. Zadeh, F.-X. Guerre, F. Lochon, M. Kaddour, L. Li, D. Walter, A. Keating, A. Jaksic, and M. Poizat, "The Technology Demonstration Module On-Board PROBA-II," *IEEE Trans. Nucl. Sci*, vol. 58, pp. 1001 –1007, Jun. 2011. Available from: http://dx.doi.org/10.1109/TNS.2010.2095468.

[126] G. Berger, "Heavy Ion Irradiation Facility (HIF) ," 2004. Available from: http://www.cyc.ucl.ac.be/HIF.

[127] "Radiation Effects Facility/ The Cyclotron Institute/ Texas A&M University.". Available from: http://cyclotron.tamu.edu/ref/.

[128] R. Harboe-Sorensen, C. Poivey, A. Zadeh, A. Keating, N. Fleurinck, K. Puimege, F.-X. Guerre, F. Lochon, M. Kaddour, L. Li, and D. Walter, "PROBA-II Technology Demonstration Module In-Flight Data Analysis," *Nuclear Science, IEEE Transactions on*, vol. PP, no. 99, p. 1, 2012. Available from: http://dx.doi.org/10.1109/TNS.2012.2185062.

[129] A. Virtanen, "The use of particle accelerators for space projects",," *Journal of Physics: Conference Series*, vol. 41, no. 1, p. 101, 2006. Available from: http://stacks.iop.org/1742-6596/41/i=1/a=008.

[130] E. Liukkonen, "The Jyväskylä's K130 Cyclotron Project," in *Twelfth International Conference on Cyclotrons and their applications, Berlin, Germany, May 8-12, 1989* (B. Martin, K. Ziegler, I. U. of Pure, A. Physics, E. P. Society, D. P. G. (1963-), and H.-M.-I. Berlin, eds.), pp. 40–42, World Scientific, 1989.

[131] E. Liukkonen, "New Cyclotron at Jyväskylä," in *Cyclotrons and their applications: proceedings of the 13th international conference, Vancouver, 1992, Vancouver, Canada, July 6-10, 1992* (G. Dutto and M. Craddock, eds.), pp. 22–27, World Scientific, 1993. invited talk.

[132] H. Koivisto, P. Suominen, O. Tarvainen, A. Virtanen, and A. Parkkinen, "Electron cyclotron resonance ion source related development work for heavy-ion irradiation tests," *Rev. Sci. Instrum.*, vol. 77, p. 03A316, Mar. 2006. Available from: http://link.aip.org/link/?RSI/77/03A316/1.

[133] H. Koivisto, M. Moisio, V. Nieminen, P. Suominen, and E. Liukkonen, "The modifications of the JYFL 6.4 GHz ECR ion source," *Nukleonika*, vol. 48, pp. s81–s84, 2003.

[134] H. Koivisto, P. Heikkinen, V. Hänninen, A. Lassila, H. Leinonen, V. Nieminen, J. Pakarinen, K. Ranttila, J. Ärje, and E. Liukkonen, "The first results with the new JYFL 14 GHz ECR ion source," *Nucl. Instrum. Methods Phys. Res., Sect. B*, vol. 174, no. 3, pp. 379 – 384, 2001. Available from: http://www.sciencedirect.com/science/article/pii/S0168583X00006157.

[135] R. Harboe-Sorensen, F.-X. Guerre, J.-G. Loquet, and C. Tizon, "Heavy-ion single-event effects testing of lead-on-chip assembled high-density memories," *IEEE Trans. Nucl. Sci*, vol. 50, pp. 2322 – 2327, Dec. 2003. Available from: http://dx.doi.org/10.1109/TNS.2003.821402.

[136] Paul Scherrer Institute, "Proton Irradiation Facility Home Page (PIF)," 2005. Available from: http://pif.web.psi.ch/.

[137] A. Javanainen, W. H. Trzaska, R. Harboe-Sørensen, A. Virtanen, G. Berger, and W. Hajdas, "Semi-empirical LET descriptions of heavy ions used in the European Component Irradiation Facilities," *IEEE Trans. Nucl. Sci*, vol. 57, pp. 1946–1949, Aug. 2010. Available from: http://dx.doi.org/10.1109/TNS.2009.2036353.

[138] A. Javanainen, J. R. Schwank, M. R. Shaneyfelt, R. Harboe-Sørensen, A. Virtanen, H. Kettunen, S. M. Dalton, P. E. Dodd, and A. Jaksic, "Heavy-ion induced charge yield in MOSFETs," *IEEE Trans. Nucl. Sci*, vol. 56, pp. 3367 –3371, Dec. 2009. Available from: http://dx.doi.org/10.1109/TNS.2009.2033687.

[139] W. H. Trzaska, T. Alanko, V. Lyapin, and J. Räisänen, "A novel method for obtaining continuous stopping power curves," *Nucl. Instrum. Methods Phys. Res., Sect. B*, vol. 183, no. 3-4, pp. 203–211, 2001.

[140] W. H. Trzaska, V. Lyapin, T. Alanko, M. Mutterer, J. Räisänen, G. Tjurin, and M. Wojdyr, "New approach to energy loss measurements," *Nucl. Instrum. Methods Phys. Res., Sect. B*, vol. 195, no. 1, pp. 147–165, 2002.

[141] H. C. Britt and H. E. Wegner, "Response of semiconductor detectors to fission fragments," *Rev. Sci. Instrum.*, vol. 34, no. 3, pp. 274–277, 1963. Available from: http://link.aip.org/link/?RSI/34/274/1.

[142] J. Perkowski, J. Andrzejewski, A. Javanainen, T. Malkiewicz, K. Sobczak, A. Virtanen, and W. H. Trzaska, "The first experimental values for the stopping power of Au ions in nickel," *Act. Phys. Pol. B*, vol. 39, pp. 507–511, February 2008.

[143] O. Osmani and P. Sigmund, "Charge evolution of swift-heavy-ion beams explored by matrix method," *Nucl. Instrum. Methods Phys. Res., Sect. B*, vol. 269, no. 9, pp. 813 – 816, 2011. Available from: http://www.sciencedirect.com/science/article/pii/S0168583X10009481.

[144] F. Grüner, F. Bell, W. Assmann, and M. Schubert, "Integrated approach to the electronic interaction of swift heavy ions with solids and gases," *Phys. Rev. Lett.*, vol. 93, p. 213201, Nov 2004. Available from: http://link.aps.org/doi/10.1103/PhysRevLett.93.213201.

[145] C. Poivey, T. Carriere, J. Beaucour, and T. Oldham, "Characterization of single hard errors (SHE) in 1 M-bit SRAMs from single ion," *IEEE Trans. Nucl. Sci*, vol. 41, pp. 2235 –2239, Dec. 1994. Available from: http://dx.doi.org/10.1109/23.340568.

[146] C. Dufour, P. Garnier, T. Carriere, J. Beaucour, R. Ecoffet, and M. Labrunee, "Heavy ion induced single hard errors on submicronic memories [for space application]," *IEEE Trans. Nucl. Sci*, vol. 39, pp. 1693 –1697, Dec. 1992. Available from: http://dx.doi.org/10.1109/23.211355.

[147] J. Felix, M. Shaneyfelt, J. Schwank, S. Dalton, P. Dodd, and J. Witcher, "Enhanced Degradation in Power MOSFET Devices Due to Heavy Ion Irradiation,"

IEEE Trans. Nucl. Sci, vol. 54, pp. 2181 –2189, Dec. 2007. Available from: http://dx.doi.org/10.1109/TNS.2007.910873.

[148] L. Scheick, "Microdose analysis of ion strikes on SRAM cells," *IEEE Trans. Nucl. Sci*, vol. 50, pp. 2399 – 2406, Dec. 2003. Available from: http://dx.doi.org/10.1109/TNS.2003.822130.

[149] T. Oldham, K. Bennett, J. Beaucour, T. Carriere, C. Polvey, and P. Garnier, "Total dose failures in advanced electronics from single ions," *IEEE Trans. Nucl. Sci*, vol. 40, pp. 1820 –1830, Dec 1993. Available from: http://dx.doi.org/10.1109/23.273474.

[150] A. Virtanen, A. Javanainen, H. Kettunen, A. Pirojenko, I. Riihimäki, and K. Ranttila, "RADiation Effects Facility at JYFL.". Available from: http://www.jyu.fi/accelerator/radef.

[151] P. J. McWhorter and P. S. Winokur, "Simple technique for separating the effects of interface traps and trapped-oxide charge in metal-oxide-semiconductor transistors," *Appl. Phys. Lett.*, vol. 48, no. 2, pp. 133–135, 1986. Available from: http://link.aip.org/link/?APL/48/133/1.

[152] S. M. Sze, *Physics of Semiconductor Physics*. John Wiley & Sons Inc., 1969.

[153] M. Shaneyfelt, J. Schwank, D. Fleetwood, P. Winokur, K. Hughes, and F. Sexton, "Field dependence of interface-trap buildup in polysilicon and metal gate MOS devices," *IEEE Trans. Nucl. Sci*, vol. 37, pp. 1632 –1640, Dec. 1990. Available from: http://dx.doi.org/10.1109/23.101171.

[154] T. R. Oldham, "Recombination along the tracks of heavy charged particles in SiO_2 films," *J. Appl. Phys.*, vol. 57, no. 8, pp. 2695–2702, 1985. Available from: http://link.aip.org/link/?JAP/57/2695/1.

[155] M. Murat, A. Akkerman, and J. Barak, "Charge Yield and Related Phenomena Induced by Ionizing Radiation in SiO Layers," *IEEE Trans. Nucl. Sci*, vol. 53, pp. 1973 –1980, Aug. 2006. Available from: http://dx.doi.org/10.1109/TNS.2006.875050.

[156] T. R. Oldham, "Charge generation and recombination in silicon dioxide from heavy charged particles," Technical Report HDL-TR-1985, Harry Diamond Laboratory, 1982.

[157] F. Sexton, D. Fleetwood, M. Shaneyfelt, P. Dodd, G. Hash, L. Schanwald, R. Loemker, K. Krisch, M. Green, B. Weir, and P. Silverman, "Precursor ion damage and angular dependence of single event gate rupture in thin oxides," *IEEE Trans. Nucl. Sci*, vol. 45, pp. 2509 –2518, Dec. 1998. Available from: http://dx.doi.org/10.1109/23.736492.

[158] S. Suyama, A. Okamoto, T. Serikawa, and H. Tanigawa, "Electrical conduction and dielectric breakdown in sputter-deposited silicon dioxide films on silicon," *Journal of Applied Physics*, vol. 62, no. 6, pp. 2360–2363, 1987. Available from: http://link.aip.org/link/?JAP/62/2360/1.

[159] M. Shaneyfelt, D. Fleetwood, J. Schwank, and K. Hughes, "Charge yield for cobalt-60 and 10-keV X-ray irradiations of MOS devices," *IEEE Trans. Nucl. Sci*, vol. 38, pp. 1187 –1194, Dec. 1991. Available from: http://dx.doi.org/10.1109/23.124092.

[160] G. Vizkelethy, D. K. Brice, and B. L. Doyle, "Heavy ion beam induced current/charge (IBIC) through insulating oxides," *Nucl. Instrum. Methods Phys. Res., Sect. B*, vol. 249, no. 1-2, pp. 204–208, 2006. Ion Beam Analysis - Proceedings of the Seventeenth International Conference on Ion Beam Analysis. Available from: http://www.sciencedirect.com/science/article/pii/S0168583X0600406X.

[161] G. Cellere, A. Paccagnella, A. Visconti, and M. Bonanomi, "Subpicosecond conduction through thin SiO_2 layers triggered by heavy ions," *J. Appl. Phys.*, vol. 99, no. 7, p. 074101, 2006. Available from: http://link.aip.org/link/?JAP/99/074101/1.